Grazing incidence small angle neutron scattering as a tool to study curved biomembranes on nanostructured surfaces

Mothander, Karolina

2021

Document Version:
Publisher's PDF, also known as Version of record

Grazing incidence small angle neutron scattering as a tool to study curved biomembranes on nanostructured surfaces

Grazing incidence small angle neutron scattering as a tool to study curved biomembranes on nanostructured surfaces

by
Karolina Mothander

LUND
UNIVERSITY

Thesis for the degree of Doctor of Philosophy

To be presented, with the permission of the Faculty of Science, Lund University, Sweden, on the 15th of October 2021 at 09:00 in Lecture hall A at the Department of Chemistry, Lund University.

Thesis advisors: **Tommy Nylander**, Peter Jönsson, Christelle Prinz and Adrian Rennie

Faculty opponent: Prof. Dr. Eva M. Herzig, Universität Bayreuth

Organization	Document name
LUND UNIVERSITY Department of Chemistry Box 124 SE–221 00 LUND Sweden	**DOCTORAL DISSERTATION** Date of disputation 2021-10-15 Sponsoring organization
Author(s) Karolina Mothander	

Title and subtitle

Grazing incidence small angle neutron scattering as a tool to study curved biomembranes on nanostructured surfaces

Abstract

Curvature in lipid-based biomembranes provides compartmentalization in cells and can act as regulator of biological activity in living systems. The study of these biomembranes require novel model systems and new methods. In this work I have used a supported phospholipid bilayer on a hexagonal array of silicon nanowires. The nanowires impose curvature on the supported lipid bilayer and the resulting structure has been investigated with a range of methods. Two main techniques have been used grazing incidence small angle neutron scattering (GISANS) and reflectometry. GISANS revealed the structure and coverage of the lipid bilayer on the nanowires, whereas reflectometry has been used to investigate the lipid bilayer on the flat areas between the nanowires. This makes the two techniques complementary, and the same bilayer has been studied on two different surfaces. In addition, confocal microscopy on fluorescently labeled lipids verified the formation of a lipid bilayer on the nanowire surface. Using fluorescence recovery after photobleaching (FRAP), I was able to verify that the formed lipid bilayer was continuous and mobile. To analyze the GISANS data a new method has been developed, which is based on the ratios of integrated peak intensities. These ratios were then compared with ratios of model-calculated form factors. This approach simplifies the analysis of the data, and allows for information on the lipid layer to be obtained directly.

Key words

GISANS, reflectometry, neutron scattering, phospholipids, supported lipid bilayers, nanowires, confocal microscopy, QCM-D

Classification system and/or index terms (if any)

Supplementary bibliographical information	Language
	English
ISSN and key title	ISBN
	978-91-7422-830-4 (print) 978-91-7422-831-1 (pdf)
Recipient's notes	Number of pages: 107 / Price
	Security classification

Grazing incidence small angle neutron scattering as a tool to study curved biomembranes on nanostructured surfaces

by
Karolina Mothander

LUND
UNIVERSITY

A doctoral thesis at a university in Sweden takes either the form of a single, cohesive research study (monograph) or a summary of research papers (compilation thesis), which the doctoral student has written alone or together with one or several other author(s).

In the latter case the thesis consists of two parts. An introductory text puts the research work into context and summarizes the main points of the papers. Then, the research publications themselves are reproduced, together with a description of the individual contributions of the authors. The research papers may either have been already published or are manuscripts at various stages (in press, submitted, or in draft).

Cover illustration front: Oil painting by Dr. Michael Persson

Cover illustration back: Photos by Karolina Mothander

Faculty of Science, Department of Chemistry

ISBN: 978-91-7422-830-4 (print)
ISBN: 978-91-7422-831-1 (pdf)

Printed in Sweden by Media-Tryck, Lund University, Lund 2021

There's plenty of room at the bottom
- Richard Feynman

Contents

List of publications

This thesis is in the form of a monograph an is based on the following publications, referred to by their Roman numerals:

I **New method for analysing grazing incidence small angle neutron scattering patterns arising from regular nanostructured arrays**

Karolina Mothander, Christelle N. Prinz, Tommy Nylander and Adrian R. Rennie
Journal of Applied Crystallography, 2021, under revision

II **Poly(styrene)-block-Maltoheptaose Films for Sub-10 nm Pattern Transfer: Implications for Transistor Fabrication**

Anette Löfstrand, Reza Jafari Jam, Karolina Mothander, Tommy Nylander, Muhammad Mumtaz, Alexei Vorobiev, Wen-Chang Chene, Redouane Borsali, Ivan Maximov
ACS Applied Nano Materials, 2021, vol 4, 5141–5151

Acknowledgements

First, I would like to give a big thanks to my main supervisor Tommy Nylander. Without Tommy believing in me some four years ago and giving me the opportunity to do a PhD I would not be here writing these words right now! I thank you for all the nice discussion, both regarding science and my PhD work, but also (and maybe more important) discussion about food, wine, gin and horses!

Secondly, I'm thanking my co-supervisor Adrian Rennie. Adrian has helped out so much with beam times, and has taught me a lot when it comes to all things neutron scattering. I'm very happy to have had Adrian as a co-supervisor!

I would also like to thank my other two co-supervisors, Christelle Prinz and Peter Jönsson, for always being there to help and discuss my work!

I have many great colleagues at Physical Chemistry. First I want to thank Maria, Johan, Polina, Jen and Ben for all the fun times and help in the lab, both in Lund and at various beam times. Secondly, I would like to thank Tommy D, and Arif for always being there to help, especially with imaging.

During my time as a PhD student I have been a part of the national PhD research school SwedNess. Thanks SwedNess for giving me the opportunity to travel and to meet a lot of really nice people. A special thanks goes to Elin and Filippa! I really hope we can meet and drink cocktails soon, maybe even at Willy & Rudy!

A big part of my PhD work has been spent on beam times at different places in the world, and these beam times would not be possible without the beam line scientists. Thanks to Paul Butler at NCNR, USA, Sarah Rogers at ISIS, UK, Henrich Frielinghaus, FRM II, Germany, and Alexei Vorobiev at ILL, France. A special thank you to Najet Mahmoudi, who was my supervisor during my three month stay at ISIS.

I came to Lund 12 years ago, and during that time I have gotten to know really amazing people. A really big thanks goes out to Bagge, Emil, Erik, Farah, Josefin, Micke, Pontus, Saair, and Stina. We see each other almost every week, often on Wednesdays, to barbecue and drink beer. I hope for many more x-bergs in the future!

Ett stort tack går till mina kära föräldrar! Mamma och pappa har alltid stöttat och trott på mig genom livet och har alltid försökt förstå vad jag håller på med. Stort tack till er!!

Till sist vill jag tacka Jacob. Tack för all hjälp och för att du alltid läser alla mina texter! Stort tack för att du alltid finns där och stöttar mig.

Populärvetenskaplig sammanfattning

Neutroner är, tillsammans med protoner, en del av atomkärnan. En neutron är en neutral partikel som kan användas för att undersöka egenskaper hos olika material. De interagerar med atomkärnan hos materialet och kan känna av olika typer av atomer, och även olika isotoper av samma grundämne. Neutroner interagerar till exempel mycket mer med väteatomer, och dess isotoper, än vad röntgenstrålning gör. Detta gör att neutroner är väldigt bra att använda för att studera biologiska prover som innehåller mycket väte.

För att undersöka material skjuts en stråle av neutroner på ett prov. När neutronerna träffar provet kommer neutronstrålen att spridas, och de spridda neutronerna fångas upp av en detektor. På detektorn kan olika mönster bildas beroende på strukturen och typen av material som finns i det undersökta provet. Det finns väldigt många olika neutronspridningstekniker, som används för att undersöka olika typer av prover. Under det här arbetet har jag använt mig av två olika tekniker, *reflectometry* och *grazing incidence small angle neutron scattering (GISANS)*. Dessa tekniker används för att studera ytor, och tunna lager på ytor. *Reflectometry* kan ge information om lagers struktur vinkelrätt mot ytan, till exempel tjocklek och vilken typ av material som finns i lagerna. *GISANS* ger istället information om material och struktur över ytan. Detta gör att de två teknikerna kan ge kompletterande information om prover.

I det här arbetet har jag använt *reflectometry* och *GISANS* för att undersöka ett fosfolipidbilager på kiselnanotrådar. En fosfolipid är en typ av fettmolekyl som bygger upp cellers membran. En cell har väldigt många olika membran som delar upp cellen i olika delar, och dessa membran kan ha olika hög kurvatur, ett mått på hur välvda membranen är. Hög kurvatur kan också uppkomma när en cell delar på sig eller när den skapar olika typer av vesikler. Kurvaturen hos ett cellmembran kan påverkas av vilka typer av fosfolipider som membranet innehåller men även av olika typer av membranproteiner. För att undersöka hur kurvatur påverkar cellmembran så har jag använt mig av ett modellcellmembran, ett så kallet *supported lipid bilayer*. För att skapa kurvatur på modellmembranet så har kiselnanotrådar använts. Nanotrådar har en diameter mellan $1 - 100$ nanometer, vilket är ungefär 1000 gånger mindre än diametern på ett hårstrå, och en längd upp till flera mikrometer. Nanotrådar används mer och mer inom forskning på celler, och när celler odlas på nanotrådar kommer cellmembranet vara den första kontaktpunkten mot nanotråden. Det är därför intressant att ta reda på hur cellmembran påverkas av nanotrådar, vilket är varför nanotrådar har används i det här arbetet.

Med hjälp av *reflectometry* och *GISANS* har jag tagit reda på strukturen och tjockleken av modellcellmembranet på nanotrådarna, men även på ytorna mellan nanotrådarna. Jag har även utvecklat en ny metod för att kunna analysera *GISANS*data.

Abstract

Curvature in lipid-based biomembranes provides compartmentalization in cells and can act as regulator of biological activity in living systems. The study of these biomembranes require novel model systems and new methods. In this work I have used a supported phospholipid bilayer on a hexagonal array of silicon nanowires. The nanowires impose curvature on the supported lipid bilayer and the resulting structure has been investigated with a range of methods. Two main techniques have been used grazing incidence small angle neutron scattering (GISANS) and reflectometry. GISANS revealed the structure and coverage of the lipid bilayer on the nanowires, whereas reflectometry has been used to investigate the lipid bilayer on the flat areas between the nanowires. This makes the two techniques complementary, and the same bilayer has been studied on two different surfaces. In addition, confocal microscopy on fluorescently labeled lipids verified the formation of a lipid bilayer on the nanowire surface. Using fluorescence recovery after photobleaching (FRAP), I was able to verify that the formed lipid bilayer was continuous and mobile. To analyze the GISANS data a new method has been developed, which is based on the ratios of integrated peak intensities. These ratios were then compared with ratios of model-calculated form factors. This approach simplifies the analysis of the data, and allows for information on the lipid layer to be obtained directly.

Introduction

My PhD work has mainly focused on using various neutron scattering techniques, mostly surface related methods such as grazing incidence small angle neutron scattering and reflectometry. I have been part of the SwedNess PhD research school, which is a national research school for PhD students with an emphasis on neutron scattering. Included in this school was courses on neutron scattering and we got to spend a lot of time at different neutron facilities around Europe and the world.

My PhD project involved revealing the structure of a nanowire supported lipid bilayer. The nanowires were used in order to induce curvature on the lipid bilayer. I investigated how the lipid bilayer was affected by the nanowires and also how adsorption of different proteins is impacted by the curvature of the bilayer. Exploring curved lipid bilayers is of interest since they are of importance for the cell, e.g. for compartmentalization within the cell and during cellular mitosis. Different lipids and membrane proteins have been shown to affect the curvature of the bilayer.

Nanowires are becoming increasingly employed in life science, where they are used as nanometer probes, cell guiding, measuring cellular forces, and to steer cell proliferations. During the culturing of cells on nanowires the first point of contact on the nanowires is the cell membrane. The interaction between the cell membrane and the nanowires has yet to be fully understood. Using a supported lipid bilayer makes it possible to mimic the cell membrane and the structure of the lipid bilayer can thus be investigated.

The first part of my PhD work was spent developing and producing my nanowire substrates. Since I have been using GISANS to investigate the nanowire supported lipid bilayer I needed a large surface area with nanowires. I started working with nanoimprint lithography (NIL), which is a technique that can be used to produce patterns on large surface areas. The idea was to use NIL to produce an etch mask and then employ reactive ion etching to fabricate the nanowires.

Unfortunately, this proved to be too difficult and the nanowires thus had to be produced elsewhere. I describe this further in chapter 2.

This thesis is written as a monograph and contains eight chapters. The first chapter gives a background to the work and introduces the various concepts used throughout the thesis. Chapters two through seven present the different projects and work done during my PhD. The last chapter contains the conclusion with an outlook.

Aims

The main scientific goals and the scientific work have been directed towards the following major goals.

- **Reveal the structure of a nanowire supported lipid bilayer using GISANS**
  The nanowires were used to induce curvature on the lipid bilayer and GISANS was employed to reveal the structure and coverage of the lipid bilayer.

- **Modeling and simulations to interpret GISANS data**
  In order to analyze and interpret the GISANS data a new method based on form factor ratios was developed.

- **Reveal how the adsorption of proteins to the nanowire supported lipid bilayer is affected by the curvature**
  As a continuation of the first objective, the nanowire supported lipid bilayer was used to study the effect on anchoring proteins.

- **Complementary reflectometry studies on nanostructured surfaces**
  As a complement to the GISANS experiments, reflectometry was used to reveal the structure of the lipid bilayer on the areas between the nanowires. I also took part in the exploration of self-assembled block co-polymers used in semiconductor processing.

Chapter 1

Background

1.1 Neutron scattering

A neutron is a neutral subatomic particle that has a weak interaction with matter, and hence has a large penetration depth into materials. Using neutrons for the investigation of different materials has many advantages over using x-rays. Neutrons are much less destructive to materials than x-rays. The neutron interacts with the nuclei of atoms in matter, which makes neutron techniques sensitive to various elements and isotopes. Compared with x-rays, neutrons are also scattered by light elements. X-ray scattering, where the x-rays interact with the electrons in the sample, are less sensitive to light elements and are not sensitive to different isotopes of the same element. The sensitivity to light elements and isotopes of the same element make neutron techniques very powerful, especially when investigating materials containing large amounts of hydrogen, such as biological samples[1].

The scattering cross section, σ, is a measure of the amount that a certain element or isotope of that element will scatter. The scattering cross section is measured in barn, which is $10^{-28}\,\mathrm{m}^2$. The strength of the interaction between the neutrons and the nucleus is referred to as the scattering length, b, of the sample, and is on the order of $10^{-15}\,\mathrm{m}$. It is related to the scattering cross section through the following relationship,

$$\sigma = 4\pi b^2. \tag{1.1}$$

Another important parameter in neutron experiments is the scattering length density (SLD). SLD is a measure of scattering power of a particular component in the sample, and is related to the density of the scattered material. The value of SLD, denoted ρ, can be calculated from the scattering length, b, and the molecular volume, V_M of a particular component in the sample according to,

$$\rho = \frac{\sum_{i=1}^{N} b_i}{V_M}. \tag{1.2}$$

In turn, the molecular volume, V_M, of a component in the sample can be calculated from the density of the material, ϱ, and the molecular mass, M,

$$V_m = \frac{M}{\varrho N_A}, \tag{1.3}$$

where N_A is the Avogadro constant [1].

Figure 1.1 shows the scattering triangle with the incoming and outgoing wave vectors, $\mathbf{k_i}$ and $\mathbf{k_f}$, respectively. The difference between the two wave vectors is the scattering vector $\mathbf{Q}$.

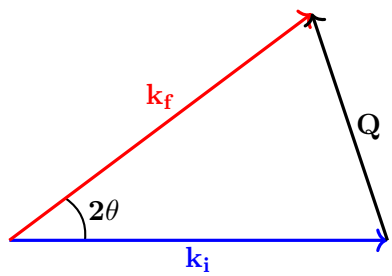

FIGURE 1.1: A schematic illustration of the scattering triangle with the incoming, $\mathbf{k_i}$, and outgoing, $\mathbf{k_f}$, wave vectors, and the resulting scattering vector $\mathbf{Q}$. For elastic scattering, the amplitude of the wave vectors are equal, $k_f = k_i$.

In elastic scattering the amplitudes of the wave vectors are equal, i.e. $k_i = k_f$, since there is no exchange of energy between the neutron and the sample, and Q is expressed as,

$$Q = 2k \sin\theta. \tag{1.4}$$

Since $k = 2\pi/\lambda$, it is possible to write,

$$Q = \frac{4\pi \sin\theta}{\lambda}, \tag{1.5}$$

where λ is the wavelength of the incoming neutron beam. The unit of Q is reciprocal length, meaning that smaller structures and objects will scatter at larger Q and larger objects at smaller Q.

1.1.1 Small angle neutron scattering

Small angle neutron scattering (SANS) is a technique for investigating large-scale structures, with a length scale of about 1 to 100 nm. Such structures include different kinds of surfactants, lipids and proteins, as well as assemblies thereof. In SANS a collimated neutron beam is transmitted through a sample that can either be an aqueous solution, a solid, a powder or a crystal. The neutron beam is elastically scattered at a small angle, typically 0.1 to 10°, from its initial trajectory, and the resulting scattering is detected on a 2D detector.

Figure 1.2 shows a schematic diagram of how a SANS experiment works. The incoming neutron beam, k_i, is transmitted through, and scattered off the sample. The scattered beam, k_f, then hits a 2D detector, at a certain distance from the initial beam trajectory. The beam will scatter at different angles depending on the shape, size and SLD of the sample which will give rise to a 2D scattering pattern, as seen in the middle of fig. 1.2. The 2D scattering pattern can then be azimuthally averaged if there is no preferential orientation, which will reduce the data to a 1D plot with scattered intensity versus Q.

There are a number of model free approximations that can be used to quickly gain information about the sample without extensive modeling. The gradient of a linear fit at small Q when plotting $\ln(I)$ against Q^2, a so-called Guiner plot, will equal $-R_G^2/3$, where R_G is the radius of gyration of the particles in the sample. This relationship is valid for $R_G Q < 1$. The radius of gyration is the root mean square of the distance from the center of mass to the different parts of the particle, and can be seen as an average radius of the particle. In polymer science the radius of gyration is used to describe the dimensions of the polymer chain. Another model free approximation is the so called Porod plot, which is a log-log plot of $Q^4 I$ against Q. At large Q, in the so called Porod regime, $Q^4 I$ tends towards a limiting value. At that point $Q \approx 2\pi/D$, where D is the diameter of the particles in the system.

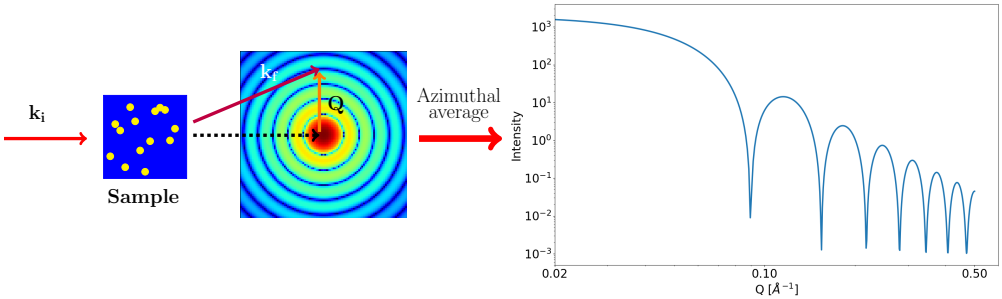

FIGURE 1.2: Schematic illustration of a SANS experiment. The scattered beam, k_f, hits a 2D detector at a certain distance from the initial beam trajectory. The detected scattering pattern is then averaged azimuthally to reduce the data to a 1D plot, with the scattered intensity versus scattering vector Q. The 2D and 1D plots shown in the image have been modeled with *SASview* [2], using the *sphere* function [3,4]. The data was modeled for an Si sphere with a radius of 50 Å surrounded with D_2O.

A widely used modeling software for SANS data is called *SASview* [2]. In *SASview* one can model and fit data with built-in functions to extract form, size and organisation of the particles. In the software it is possible to fit data from multiple contrasts simultaneously to gain more information about the system.

1.1.2 Reflectometry

Reflectometry is a technique for investigating interfaces and thin films on surfaces. In neutron reflectometry a highly collimated neutron beam is reflected from a flat surface with a grazing incidence angle, θ, and the intensity of the reflected beam at the same angle (specular reflection) is determined.

In reflectometry information about the thickness of thin films, as well as the solvent content, composition, and any roughness between the layers, can be obtained. Figure 1.3 shows modeled reflectivity data of lipid bilayers on a Si/SiO_2 substrate in D_2O. The data is modeled with the lipid DOPC, which is used later in this thesis, and for one, two and three bilayers. For the Si/SiO_2 substrate there are no fringes, whereas with one bilayer, corresponding to the red line in the figure, there are two fringes. When the number of bilayers increases, so does the number of fringes. The thickness, d, of a film can be calculated according to,

$$d = \frac{2\pi}{\Delta Q}, \tag{1.6}$$

where ΔQ is the difference in Q between two adjacent fringes [1].

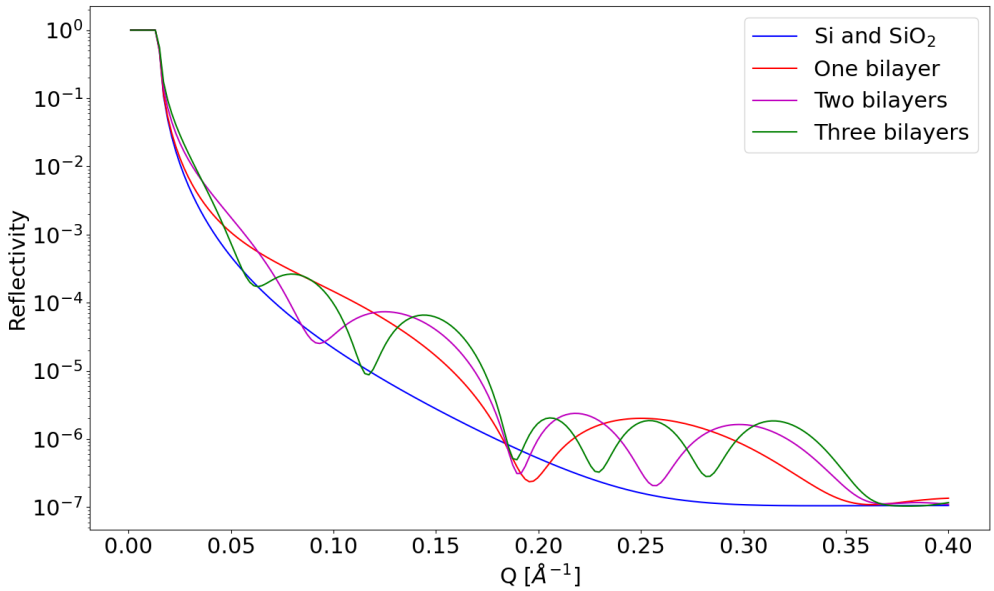

Figure 1.3: Modeled data of DOPC lipid bilayers on a Si substrate surrounded by D_2O with an increasing number of bilayers. The data was modeled using *refnx* [5], where one lipid bilayer was simulated as two individual lipid leaflets using the default parameters for a DOPC lipid leaflet in *refnx*.

To analyze reflectivity data there exist various software packages that one can use. For example, with the software *refnx* [5] (used in chapter 7) a model is created based on what is known about the sample and the software then calculates the reflectivity using the Abelès method. The calculated reflectivity is subsequently compared and refined against the data. From the model fit, information about the thickness and SLD of the layers is obtained.

1.1.3 Grazing incidence small angle neutron scattering

Grazing incidence SANS is a surface technique, but instead of only considering the reflected specular beam direction, the off specular reflection (or scattering) is considered. In reflectometry, information is obtained about structures perpendicular to the surface of the sample, whereas in GISANS, information is also obtained on the lateral structure over the sample. This means that surface structures which would be impossible to see with reflectometry are revealed. SANS is, instead, a bulk technique, so one can say that GISANS lies somewhere in-between SANS and reflectometry.

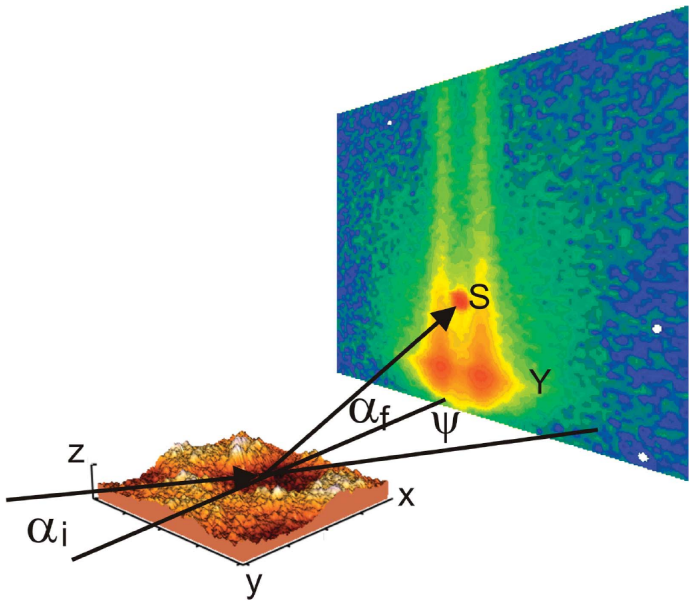

Figure 1.4: Schematic illustration of a GISANS experiment. The incident beam, α_i, hits the sample surface at a small angle, typically below 1°. The specular peak (S) is where the angle of the exiting beam, α_f, is the same as the angle of the incoming beam. The Yoneda peak (Y) is where the exiting beam angle is the same as the critical angle of the sample. Image from Müller-Buschbaum[6].

In GISANS, a collimated neutron beam is impinged on a sample surface at a very small angle. The incident angle in GISANS is often below 1° and is on the order of the critical angle of reflection from the sample. The neutron beam is then scattered and the scattered neutrons are recorded with a 2D detector. Figure 1.4 shows a schematic diagram of a GISANS experiment, where the incident and exit angles are α_i and α_f, respectively. On a GISANS scattering pattern one often find a specular peak (denoted S in fig. 1.4), which is where the incident and exit angles are the same. The other peak often seen is the Yoneda peak (denoted Y in the figure), which is where the incident angle and the critical angle of the sample are identical. Besides the specular and Yoneda peaks, there often also exist a number of Bragg peaks corresponding to the repeat distance of the structures in the sample[6].

In order to probe structures at different depths in the sample, one can change the incoming beam angle. Figure 1.5 shows the change in penetration depth at an Si and D_2O interface at a wavelength of 5 Å and varying incident angles. The x-axis displays the ratio of the incident beam angle to the critical angle. At the critical angle the penetration depth changes dramatically and the beam

can probe deep into the sample. Tuning the incident beam angle will enable the probing of different depths in the sample. Changing the wavelength of the beam will alter the critical angle and it is therefore possible to investigate various average depths with a change in wavelength.

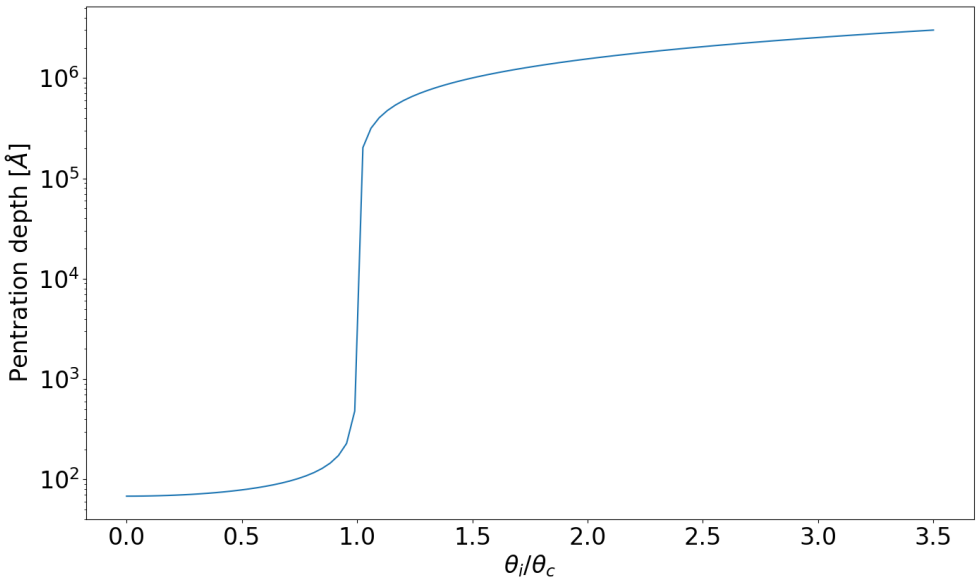

Figure 1.5: Penetration depth of an Si and D_2O interface at 5 Å. The x-axis is the incoming beam angle over the critical angle of the sample. When the incident angle is equal to the critical angle there is a dramatic change in penetration depth.

GISANS experiments are often conducted on either SANS or reflectometry instruments. A SANS instrument is often preferable since it is possible to collimate the beam in a point shape to obtain enough resolution in the q_y, lateral, direction.

1.1.4 Time of flight scattering

Time of flight (ToF) refers to the time it takes a neutron to travel a specific distance. ToF is often used at pulsed neutron sources, where all the neutrons come to the instruments in discrete pulses. However, it is possible to use a continuous source and a chopper to create the same effect as that of a pulsed neutron source. If the exact times that the neutrons left the source and arrived at the sample are known, then one can calculate the wavelengths of the neutrons using the de Broglie equation,

$$\lambda = \frac{h}{mv}, \tag{1.7}$$

where h is the Planck constant, m is the mass, and v is the velocity of the neutron, calculated from the travel time and distance from the source to the sample.

Compared with a monochromatic instrument, a ToF instrument will allow making use of a larger flux of neutrons and multiple wavelength at the same time. All the wavelengths can then be used and the data reduced to a single Q-scale, or just one wavelength can be chosen. The downside of choosing just one wavelength is that the flux will decrease, however, there might be some features in the sample that are only visible at certain wavelengths.

One way to probe different depths in GISANS, as mentioned previously, is to change the wavelength of the incoming beam. Using ToF GISANS means that several wavelengths will be accessed simultaneously and therefore multiple different depths will be probed with one measurement. Figure 1.6 shows twelve 2D ToF GISANS images, separated by different wavelengths, with wavelengths ranging from 5 Å to 14.8 Å. The sample in the figure was polystyrene nano-dots. The images clearly shows the development of different structures and peaks, arising from the varying depths probed in the experiment [7].

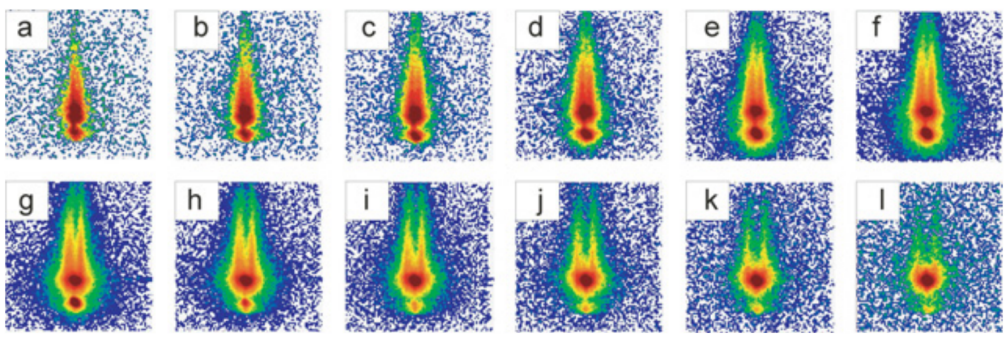

Figure 1.6: Twelve 2D ToF-GISANS images of polystyrene nano-dots on a solid support measured simultaneously, separated by different wavelengths a) 5 Å, b) 5.5 Å, c) 6.1 Å, d) 6.8 Å, e) 7.5 Å, f) 8.2 Å, g) 9.1 Å, h) 10 Å, i) 11 Å, j) 12.2 Å, k) 13.5 Å, and l) 14.8 Å. Data and image from Müller-Buschbaum et al. [7].

1.2 Nanowires

Nanowires are large aspect ratio structures with a diameter in the nm-range and a length of one or several µm. Due to their large aspect ratio, nanowires are often called 1D materials[8]. Nanowires can be made of several different materials, however, here the focus will be on semiconductor nanowires. Nanowires can be made from either one single material, so called homostructures, or from two or more different materials, so called heterostructures. The latter can be either radial, where additional material is added to an already existing nanowire, or axial, where the material changes along its length. The materials used for heterostructures do not have to be lattice matched, where the two materials have similar lattice constants, since the small diameter of the nanowire reduces the strain effect[9,10].

In semiconductor processing, like in the fabrications of nanowires, there are two main ways of producing structures, bottom-up and top-down. Generally, in a bottom-up process material is added and in a top-down process material is removed. Bottom-up nanowire fabrication uses epitaxial growth through a process called vapor-liquid-solid growth. The technique employs a metal seed particle which is brought into contact with precursor gases. The gases interact with the deposited metal nanoparticle thereby giving rise to axial growth[11]. The top-down method utilizes etching to produce the nanowires. Here a predefined etch mask ensures the size and placement of the nanowires. Etching is often employed to produce silicon nanowires, through a technique called the black silicon method[12,13]. More on these methods is given in Chapter 2.

Nanowires have many potential applications, for instance in electronic devices[14], lasers[15], and solar cells[16,17]. The use of nanowires in life sciences[18] are of particular interest for this thesis. Nanowires have been utilized for cell guiding[19–21], measuring signals from cells[22–24] and cell forces[25,26]. When growing, or culturing cells, on nanowires various cell types react differently to the presence of the nanowires. Fibroblasts, which is the most common cell type in connective tissue, cultured on nanowires exhibit a decrease in motility, cell division, as well as DNA damage[27]. In a mixed cell culture of neurons and glial cells, which are helper cells for neurons within the central nervous system, the glial cells often take over. However, when the same cells are cultured on nanowires, the growth on the glial cells is inhibited, while the neuron growth remains unaffected[28].

A cell cultured on nanowires will first come into contact with the nanowire through the cell membrane, however it is not fully understood how the cell membrane interacts with the high-aspect ratio nanowires. Thanks to techniques

such as scanning electron microscopy (SEM), transmission electron microscopy (TEM), or focused ion beam milling combined with SEM (FIB-SEM) it is possible to image the cell-nanowire interaction, but common for all these methods is that the cells first need to be fixed, stained and dehydrated, and sometimes also covered with metals and resins[27,29,30]. Such treatment can alter the shape of the cell and membrane making it difficult to determine the actual shape of the living cell. Thus, in order to study the membrane of living cells, other techniques are required.

1.3 Phospholipids

Phospholipids are the main building block of biological membranes and consist of a hydrophobic tail region with two acyl chains and a hydrophilic head group, see fig. 1.7. The tail consists of two fatty acids connected to a glycerol molecule, and the head is made up of a phosphate group. Figure 1.7 shows a simplified schematic diagram of a phospholipid bilayer constituting the matrix of a simple cell membrane. Here two monolayers of lipids with the hydrophobic tails pointing towards each other. The structure of the phospholipid membrane creates a water impermeable barrier around cells and organelles[31].

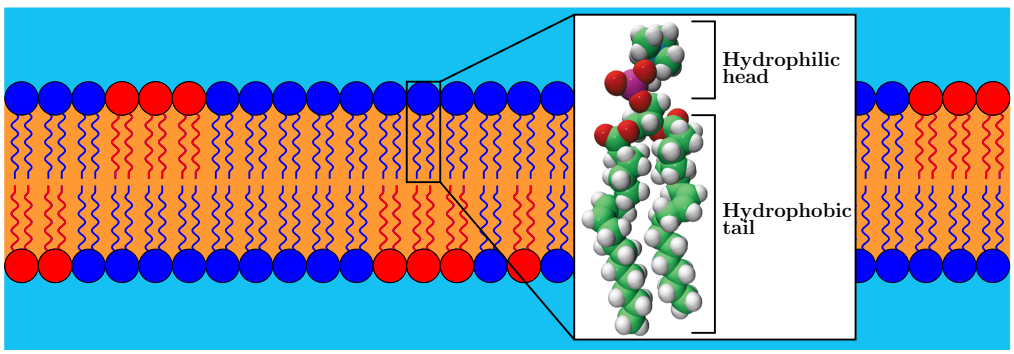

Figure 1.7: Simplified schematic diagram of a phospholipid membrane, consisting of two rows of phospholipids with the hydrophobic tail groups pointing towards each other. The blue and red lipids in this bilayer are DOPC and DOPE phospholipids, respectively (more on these in chapter 3). The insert is a 3D model of a DOPC lipid, showing the hydrophilic head and hydrophobic tail. The 3D image is from Avanti Polar Lipids[32].

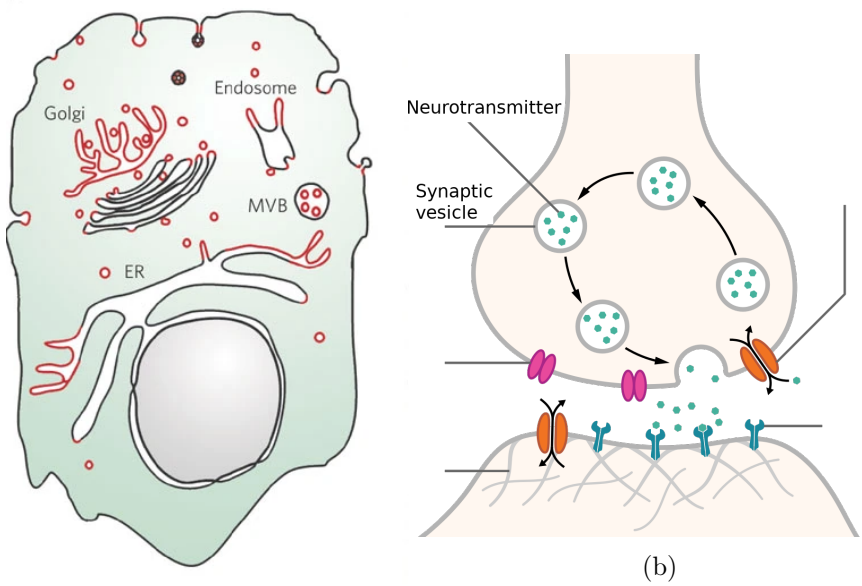

(a) (b)

Figure 1.8: (a) Areas of locally high curvature, shown in red, of the membranes with in a cell. ER stands for the endoplasmic reticulum which is the site of the ribosomes which are responsible for protein synthesis in the cell. MVB stands for multivesicular bodies and are a so-called late endosome. Endosomes are part of the sorting and cleaning system of the cell. Endosomes are connected with Golgi body which packs proteins into vesicles before the proteins are transported to their final location. Diagram from McMahon and Gallop[33]. (b) A schematic view of a synapse showing the synaptic vesicles containing neurotransmitters. Diagram from Splettstoesser[34].

1.3.1 Curved lipid bilayers

Cell membranes function as a divider of the cell from its surrounding and of the organelles from the cytosol. The membrane is an important part of the cell and organelles, and many processes take place on and around it. The membrane that surrounds the cell and organelles have varying degrees of curvature, and fig. 1.8a displays a schematic view of a cell, accentuating areas of high curvature. The figure highlights the intricate form of the Golgi apparatus and vesicles budding from the cell membrane. Vesicles are often used for communication in and between cells, for example the transport of neurotransmitters in synaptic vesicles, as displayed in fig. 1.8b[33].

There are several ways a membrane can curve. Changing the lipid composition in a bilayer can cause the membrane to change curvature depending on the shape

of the lipid molecules. The cytoskeleton within the cell and microtubule motors outside of the cell can cause the membrane to deform. Different types of protein scaffolding and insertion of amphipathic helices can also give rise to curvature of the cell membrane. The shape of the membrane proteins can influence where on the membrane they are located. The focus in this section is on the role of different lipids have on the curvature of the membrane. If a membrane protein has a more conical shape it will concentrate to areas that match the shape of the protein[35,36].

Lipids can self-assemble into many different structures, the shapes of which can be explained by the lipid molecular packing parameter[37]. This packing parameter is defined as $P = V/(a\,l)$, where V is the molecular volume, a is the cross-sectional area of the head group and l is the length of the molecule. Figure 1.9 shows the effect of the packing parameter on the lipid structures. For $P = 1$ the lipids form a lamellar bilayer, whereas for $P < 1$ the lipids create hexagonal structures and micelles. On the other hand, reverse curvature is favored for $P > 1$ where the lipids create cubic phases, inverted hexagons and inverted micelles. In this case inverted means that the lipid aqueous interface is curved towards the solvent[38]. Another way to express the packing parameter is with the lipid intrinsic radius of curvature, R_0, which is defined as the curvature that minimizes the elastic free energy of a lipid monolayer. The intrinsic radius of curvature is a property innate to lipids and decreases for lipids with a larger spread between the tails, e.g. unsaturated lipids. In contrast, it increases for lipids with a larger headgroup area[39]. The intrinsic radius of curvature can be simplified into the intrinsic curvature of the lipid, $C_0 = 1/R_0$, to avoid the singularity for lamellar phases, where $R_0 = \infty$. Lipids that form a lamellar bilayer would have an intrinsic curvature close to 0.

1.3.2 Supported lipid bilayers

Cell membranes are a complex mixture of lipids and proteins. Phospholipid bilayers have the fluidity and barrier function of a cell membrane and are a good environment for membrane proteins, making them a decent model for real cell membranes. Supporting the bilayer on top of a solid support creates a stable and robust bilayer. There are three common types of supported lipid bilayers (SLB), bilayers with the inner monolayer fixed to the supported substrate, freely supported bilayers, and bilayers supported by a soft hydrated polymer film[40]. The first and latter of the three are commonly used to study transmembrane proteins[41]. To obtain a good quality freely supported lipid bilayer the support needs to be hydrophilic, smooth and clean. Materials such as silica, glass or

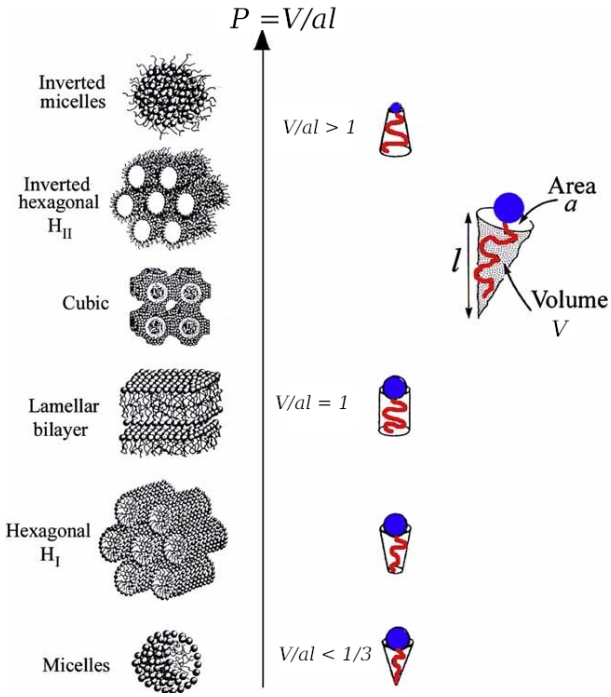

Figure 1.9: Schematic illustration showing the effect of the packing parameter, P. Lipids that have a packing parameter close to 1 have an intrinsic curvature close to 0 and form a lamellar bilayer. Lipids with a packing parameter larger than 1 have a negative intrinsic curvature. Drawing from Mouritsen[38].

silicon oxide are good candidates for supports[42]. Supported lipid bilayers enable the use of surface techniques, such as ellipsometry, Fourier transform infrared spectroscopy, and neutron and x-ray reflectometry, and they can for instance be used as model cells to study the interactions between ligands and receptors[40].

There are three main ways to creating supported lipid bilayers. The first employs the Langmuir-Blodgett technique to create a monolayer, after which a second monolayer is pushed down on the first monolayer using the Langmuir-Schaefer procedure[43,44]. The second technique involves attachment, ruptured vesicles, followed by spreading to form a lipid bilayer (more on that technique in chapter 3)[45]. The last method can be seen as a combination of the first two, where the first monolayer is formed with the Langmuir-Blodgett technique and the second one is created via vesicle fusion[44].

To study the effect of curvature on a lipid bilayer, a curved supported lipid bilayer can be used. A common method for creating a curved SLB is to coat silica nanoparticles with a lipid bilayer. Lipid coated nanoparticles have been

used to study the packing of lipids as a function of the curvature of the lipid layer[46,47]. Curved structures in an SLB can be induced by the asymmetric ionic strength of the surrounding solvent[48]. Another way to introduce curvature to a supported lipid bilayer is by means of nanowires. Dabkowska et al.[49] described the formation of a lipid bilayer on an array of GaP nanowires and a similar nanowire supported lipid bilayer was used in this thesis, but with nanowires made of Si.

Chapter 2

Nanowire substrate

Nanowires are finding increasing usage in life science for both sensing and promotion of cell growth. In this study, nanowires were employed to impose curvature on a lipid bilayer, which is an important feature for both types of applications. The main method for studying the lipid bilayer on the nanowires was with GISANS (see chapters 4 and 5). In a GISANS experiment a neutron beam hits a surface at a very shallow angle. This means that the neutron beam will cover a large surface area, meaning that a large and homogeneous sample is needed.

The nanowires used in this work were produced through etching with an etch mask that was obtained either by nanoimprint lithography (NIL), at the Lund NanoLab, or by electron beam lithography (EBL), at the Danchip Nanolab. I carried out the initial processing of the substrate at the Lund Nanolab. Unfortunately, the processing proved to be too challenging and time-consuming to produce sufficiently large substrates with the available equipment, so it was decided to have the substrate processed at the Danchip Nanolab at the Danish Technical University in Copenhagen.

2.1 Method

2.1.1 Nanoimprint lithography

Nanoimprint lithography uses a stamp to transfer a pattern on to a polymer resist. The pattern in the polymer resist can then be used to transfer a metal

pattern onto the substrate. There are a few different versions of NIL, thermal press, room temperature, and UV nanoimprint. They all share the basic principle, i.e. a stamp is pressed into a polymer for pattern transfer, but they differ with regard to the temperature and pressure used and whether or not UV-light is required[50,51]. The remainder of this section focuses on UV nanoimprint since that was the method used for this project.

The stamp in the NIL processes can be manufactured from several different materials. In UV-NIL the stamp needs to be made from a UV transparent material in order to let the UV light through the stamp. Stamps can be made from quartz or polydimethylsiloxane (PDMS). A method to increase the lifetime of the stamp is to transfer a master stamp to a polymer material, a so-called intermediate polymer stamp (IPS)[52,53], and then use the polymer stamp for the imprint.

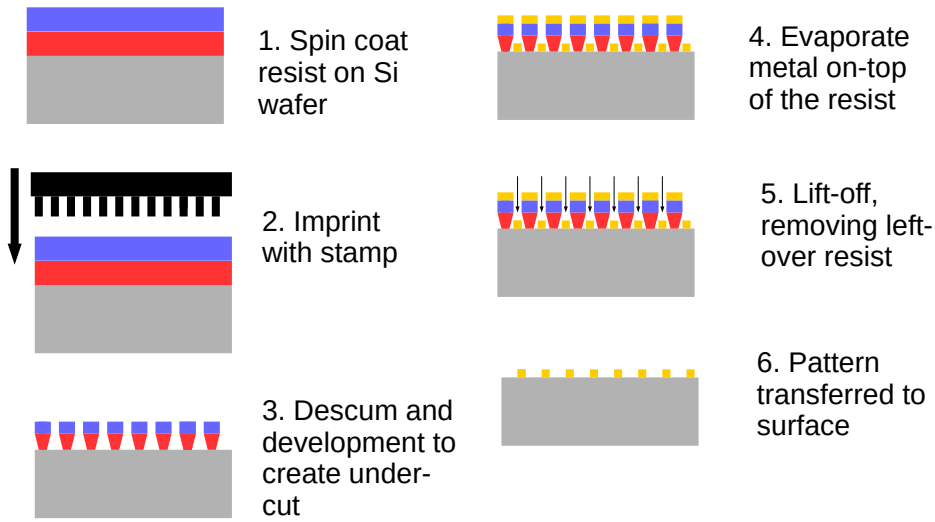

Figure 2.1: A schematic diagram of the NIL process. First, two resists are spin-coated to the wafer, the resist closest to the surface acts as a lift off-resist and creates the under-cut shown in step 3. The second step is the imprint, followed by the descum and development stage to create the under-cut which helps with the lift-off in step 5. The fourth step is thermal evaporation of the metal, in this case 30 nm of Cr. Lastly, the left-over resist is lifted-off and the pattern is transferred to the surface.

Figure 2.1 shows a simplified view of the NIL process. The first step consists of spin-coating two resists. The first, LOR0.7A (red in the figure), was spin-coated at 6000 rpm for 63 s, after which the spin-coated wafer was baked on a hotplate at

200 °C for 10 min. The second resist, TU7-90 (blue in the figure), was spin-coated at 2000 rpm for 63 s and then baked on a hotplate at 95 °C with vacuum contact for 1 min. The two resists were utilized to ensure an under-cut in the walls of the resist. Such an under-cut is necessary for the lift-off process, described below. Before the imprint, the master nickel stamp was copied to an IPS. The spin-coated Si wafer was placed in the NIL machine (Obducat, Lund, Sweden) and heated. The IPS was then positioned on top of the Si wafer and pressed onto it. When the stamp was pressed into the resist, the UV light was turned on to harden the resist. This was followed by what is called the descum process, which involves etching with O_2 plasma. This step is needed to remove the excess resist at the bottom of the imprinted holes. The sample was etched using Sirius T2 plus (Trion Technology, Tempe, AZ, USA), O_2 flow set at 40 sccm (standard cubic centimeter per minute) with a pressure of 150 mTorr and at 50 W power for approximately 30 s. After the descum process, the sample was developed using 3 : 1 MF319 for 60 s followed by DI water for 3 min and nitrogen drying. The development produced an under-cut in the resist layer closest to the silicon wafer. A 30 nm thick layer of chromium was subsequently thermally evaporated onto the wafer and this Cr only came into contact with the Si wafer where the NIL process left holes in the resist. The removal of the resist, which is a process called lift-off, was carried out by placing the sample in Remover 1165 for 5 min at 90 °C, followed by 5 min in an ultrasonic bath and lastly heating for 5 min at 90 °C. The process was repeated until the excess Cr covering the resist had been visually lifted-off.

2.1.2 Electron beam lithography

Electron beam lithography (EBL) works in a very similar way to a scanning electron microscope (SEM). To create a pattern, a substrate is covered with an electron beam sensitive resist and a focused electron beam scans over the surface according to a predefined pattern [51]. The resolution of patterns using EBL have steadily improved since the first experiments in the 1960s and patterns down to 5 nm can now be realized [54].

Figure 2.2 gives an overview of the EBL process. The first step, similar to the NIL technique, was to spin-coat a layer of resist on the Si substrate. In the case with EBL only one resist was used. A pattern was then written in the resist, the resist was developed and a 13 nm thick layer of Cr was evaporated onto the surface. The leftover resist and Cr on-top of the resist were removed through lift-off, using the Remover 1165, leaving Cr dots on the surface as an etch mask.

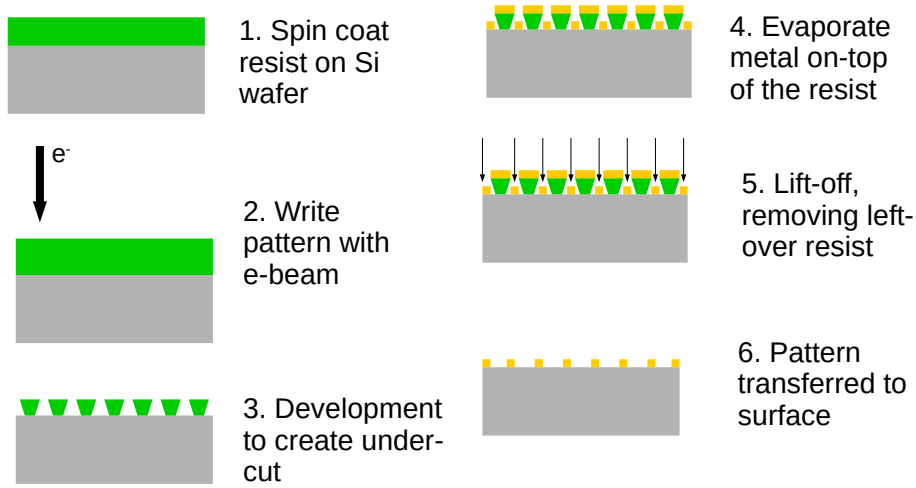

Figure 2.2: A schematic diagram of the EBL process. The first step involves to spin-coating the resist on the Si surface. The second step is to write the pattern in the resist by means of the electron beam. Subsequently, the pattern is developed to create the under-cut, and metal is evaporated on-top of the resist. Finally, the left-over resist is lifted-off and the pattern has now been transferred to the surface.

2.1.3 Reactive ion etching

Reactive ion etching (RIE) is a very common technique used in nano-fabrication. RIE is a type of dry etching and all the etching takes place in plasma. The plasma is generated by an RF field between a cathode and an anode. The sample is placed on the cathode and the negative ions in the plasma are accelerated towards the sample. The method uses both physical and chemical processes, where the former involves ionization of reactive gas molecules and physical sputtering of the substrate. However, the most dominant process in RIE is the chemical one. RIE processes often make use of halogen-containing gases, such as fluorine, or chlorine, since they are the most reactive and erosive. Both are employed for etching Si, with the difference between them being the way they etch Si. Fluorine has a faster etch rate, however, it etches more isotropically, whereas chlorine, on the other hand, etches slower but more anisotropically [51].

The etch rate in an RIE process is directly dependent on the plasma density in the chamber, and the plasma density increases with an increase in RF power. However, with an increase in RF power, there is also a rise in ion bombardment energy, which leads to reduced etch selectivity. To get around this problem, it

is possible to use inductively coupled plasma (ICP) RIE, in which the plasma is produced independently of the RF power at the sample. This gives a much higher plasma density, but at the ion bombardment energy of a normal RIE process. ICP-RIE processes hence give higher etch rates while maintaining the high selectivity of a standard RIE technique [13,51,55]. To produce the Si nanowires used in this thesis an ICP-RIE process has been used. This approach used a mix of different fluorocarbon gases in a procedure commonly called the black silicon method, and can produce very anisotropic, straight walled, Si structures [12,56,57].

2.2 Results

2.2.1 Nanoimprint test

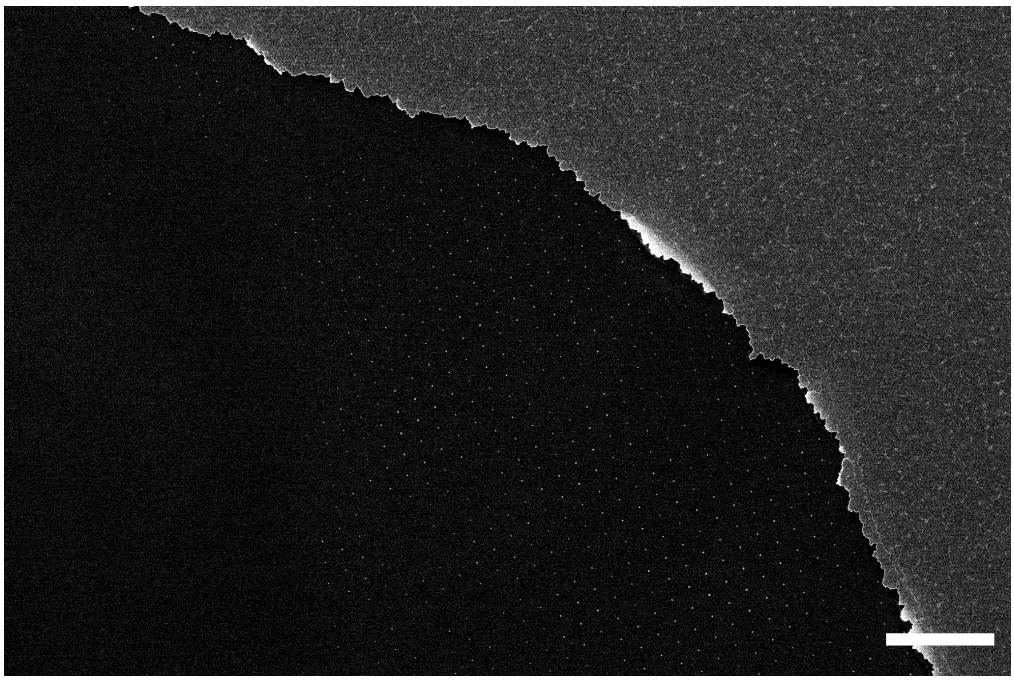

Figure 2.3: An example of a sample after NIL and thermal evaporation of Cr. The large piece in the top right corner is leftover Cr. Scale bar is 5 µm.

NIL is a fast processing technique to produce a pattern over a large area. However, there are several different parameters that need to be optimized in order to get an even and reproducible result. Here, NIL was performed on a *2 inch* Si wafer and was imaged by SEM after each process step. The purpose of NIL was

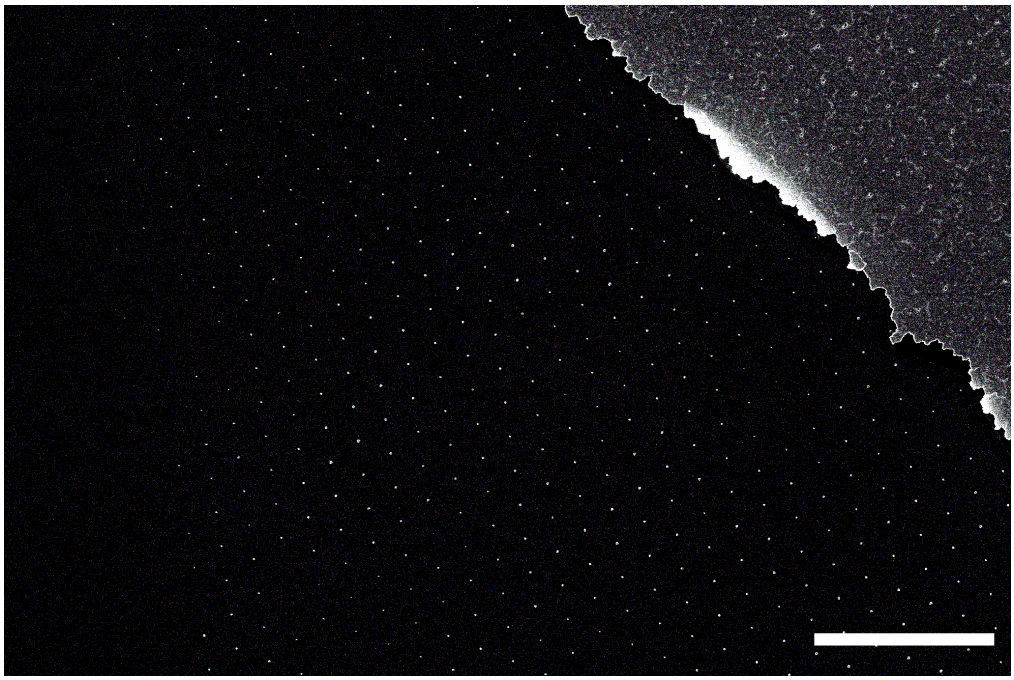

Figure 2.4: A magnified version of the image in fig. 2.3. Here, the Cr dots in the hexagonal pattern are clearly visible. Scale bar is 5 µm.

to produce a hexagonal pattern of dots which would be used as an etch mask for nanowire fabrication.

Figure 2.3 shows an example of how the wafer looked after metal evaporation and lift-off, and fig. 2.4 displays a magnified image of the same area. As can be seen in the images there were small dots in a hexagonal pattern, however, there were also large areas without dots and a large piece of Cr still left on the surface.

The missing pattern and the large piece of Cr left on the surface, shown in figs. 2.3 and 2.4, were most likely due to the same issue, an incomplete pattern transfer from the stamp to the resist. Where the dots are missing, the stamp most likely did not penetrate through the resist layer and did not leave holes all the way down to the Si wafer. Holes through the resist layer are needed so that the Cr evaporated on top of the resist can come into contact with the wafer. If there is not contact between Cr and Si, then all the Cr will be removed along with the resist in the lift-off process, leaving a surface without dots.

On the area with the large piece of Cr it was likely the there was too little undercut in the resist layers around the holes. The undercut in the resist layer

is needed so that the lift-off chemicals can come into contact with the resist and hence remove the resist and the Cr on top of it.

The incomplete pattern transfer of the stamp to the resist layer could be due to small particles on the surface or the way the stamp was removed from the resist. Small particles on the surface can result in an uneven contact between the stamp and the resist layer, causing the pattern to be imprinted unevenly. If the stamp is not removed very carefully then some of the resist will follow the stamp and not stay on the surface.

2.2.2 Etch test

To produce the nanowires, reactive ion etching was performed. With RIE there are several different parameters that need to be optimized, and due to time constraints I could unfortunately only carry out two tests. Figure 2.5 shows the obtained results. There was quite a clear difference between the two samples. Their processing involved the same gases, O_2, CHF_3, and SF_6, with the only difference being that fig. 2.5a used 4 sccm[1] CHF_3 and fig. 2.5b used 8 sccm[1] CHF_3. Many more tests would have been needed in order to fine tune the recipe to make perfectly straight nanowires.

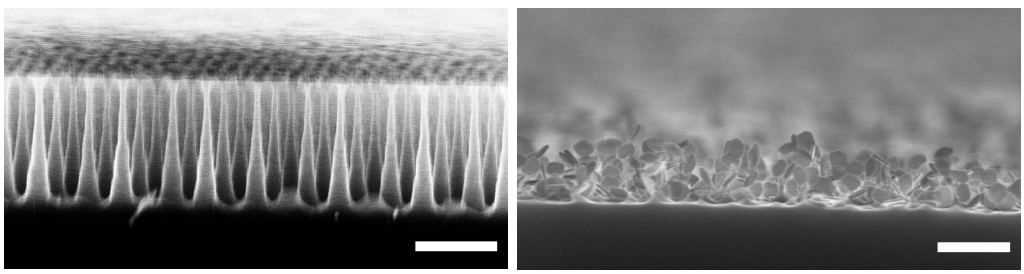

(a) (b)

Figure 2.5: Test to produce Si nanowires with reactive ion etching. The wafer is imaged by breaking the wafer in half and then imaging the broken edge. Both etch tests used the same recipe, the only difference being that (a) has 4 sccm of CHF_3 and (b) has 8 sccm CHF_3. Scale bars are 1 µm.

[1]The unit sccm stands for *standard cubic centimeters per minute.* and is used to measure flow rate during etching

2.2.3 Final sample used in this thesis

The samples that have been used throughout this thesis were produced at the Danchip Nanolab in Copenhagen. They were made with etching and the etch mask was produced with EBL. Two differently sized samples were produced, one 0.6 mm thick, *2 inch* (50.8 mm) in diameter wafer and one Si block with dimensions 65 mm × 65 mm × 6.25 mm. Initially, it was unclear if it would be possible to create a sample larger than a *2 inch* wafer, hence the two sample sizes. Both samples were covered with nanowires, which were around 85 nm in diameter, approximately 750 nm in length and spaced 500 nm apart in a hexagonal pattern.

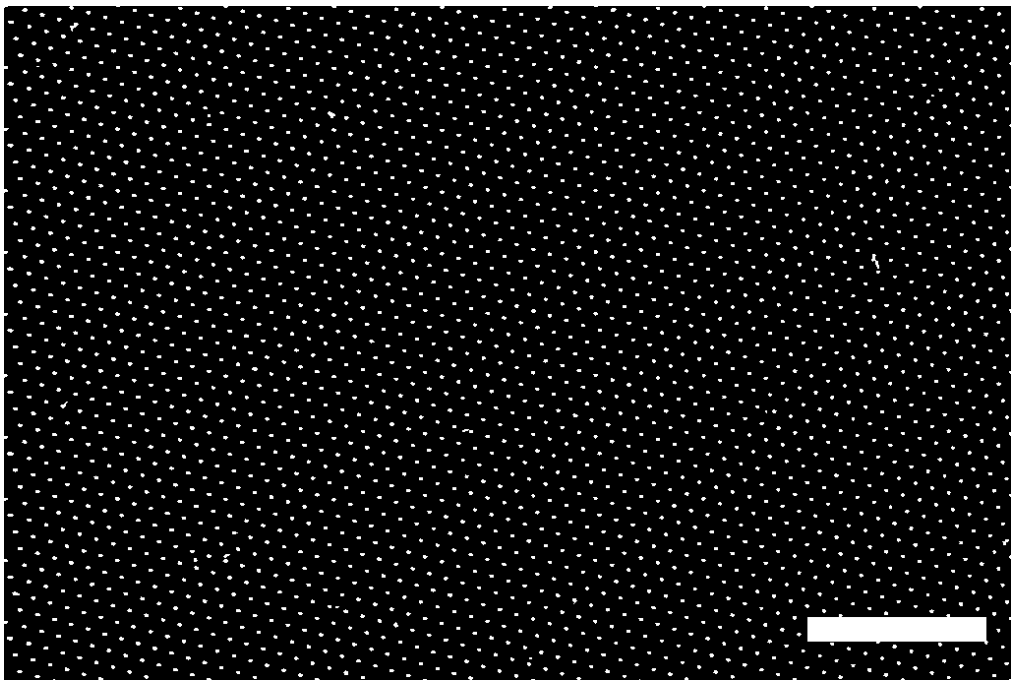

Figure 2.6: An overview of the etched nanowires. Scale bar is 5 µm.

Figure 2.6 shows an overview of the resulting nanowire sample. The image displays the top of the nanowires and reveals that the nanowires were uniformly positioned over a large area. Figure 2.7 shows the nanowires imaged with a 30° stage tilt. Tilting the SEM stage 30° allows for easy length measurements of the nanowires, i.e. by taking the length in the image and multiplying by 2.

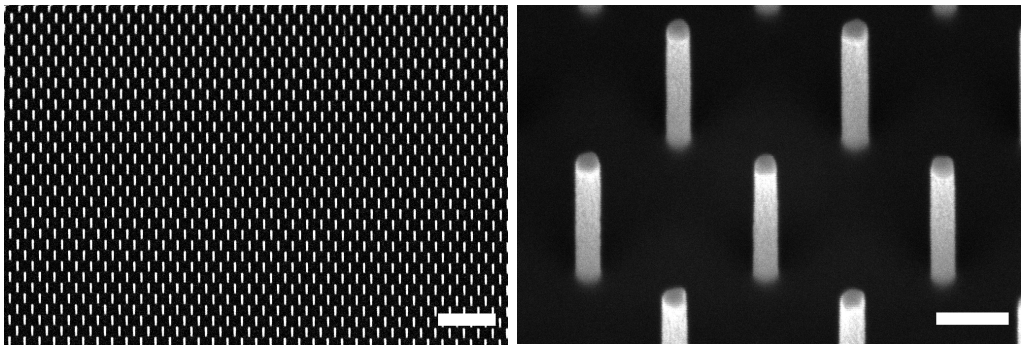

(a) (b)

Figure 2.7: The nanowires imaged at a 30° tilt of the SEM stage. The scale bar in (a) is 2 µm and in (b) it is 200 nm.

2.3 Summary

There are many different methods to produce nanowire arrays. Here, the top-down approach using etching was used. In order to etch nanowires at predetermined positions an etch mask first needs to be defined, which in this case was done with NIL or with EBL. Both techniques have their advantages and disadvantages. EBL is very flexible and can write almost any type of pattern, but it takes a long time, and the larger the patterned area, the longer the writing time will be. With NIL, the whole pattern can be defined simultaneously, however, different defects can easily appear. In this case, the development of an even pattern over a large surface and perfectly straight nanowires proved to be difficult and time consuming, and the decision was made to outsource the sample processing.

Chapter 3

Formation of the supported lipid bilayer

Nanowires are finding increased use in life science. Different types of cells have been cultured on nanowires to control cell proliferation[28], to measure signals from cells[22], and to measure cell forces[26], among other things. When cells are cultured on nanowires the first point of contact is the lipid bilayer which can form a locally, highly curved membrane around the nanowires. This highly curved membrane has been studied with scanning electron microscopy (SEM), transmission electron microscopy (TEM) and focused ion beam milling (FIB) – SEM, however, these techniques require the cells to be fixed and dehydrated, which can lead to deformation of the cell membrane. By using a supported lipid bilayer on nanowires as a model for the highly curved cell membrane, it is possible to explore the curvature effects introduced by the nanowires. More information on supported lipid bilayers is given in the background chapter.

The present chapter is focused on the formation of the supported lipid bilayer, which was done by means of vesicle fusion. To be able to follow the formation of the lipid bilayer on a planar surface, QCM-D was used. The formed bilayer on nanowires was imaged using confocal microscopy.

3.1 Method

3.1.1 Supported lipid bilayer

Throughout this thesis work I used a model biomembrane, consisting of two phospholipids, DOPE (1,2-dioleoyl-sn-glycero-3-phosphoethanolamine, fig. 3.1b) and DOPC (1,2-dioleoyl-sn-glycero-3-phosphocholine, fig. 3.1a), in a supported lipid bilayer. Both lipids were purchased from Avanti Polar Lipids (Alabaster, AL, USA), with a purity of over 99%. These two lipids are found in biological membranes, where about 9% and 45% of the phospholipids in the human brain consists of DOPE and DOPC, respectively[58]. The intrinsic curvature of DOPC and DOPE is $-0.11\,\mathrm{nm}^{-1}$ and $-0.48\,\mathrm{nm}^{-1}$, respectively[59]. A negative intrinsic curvature means that the volume of the tail group is slightly larger than the area of the head group times the length of the tails. The shape of DOPC is cylindrical whereas the shape of DOPE is that of an inverted cone, where DOPE on its own forms a non-lamellar reverse hexagonal phase[60].

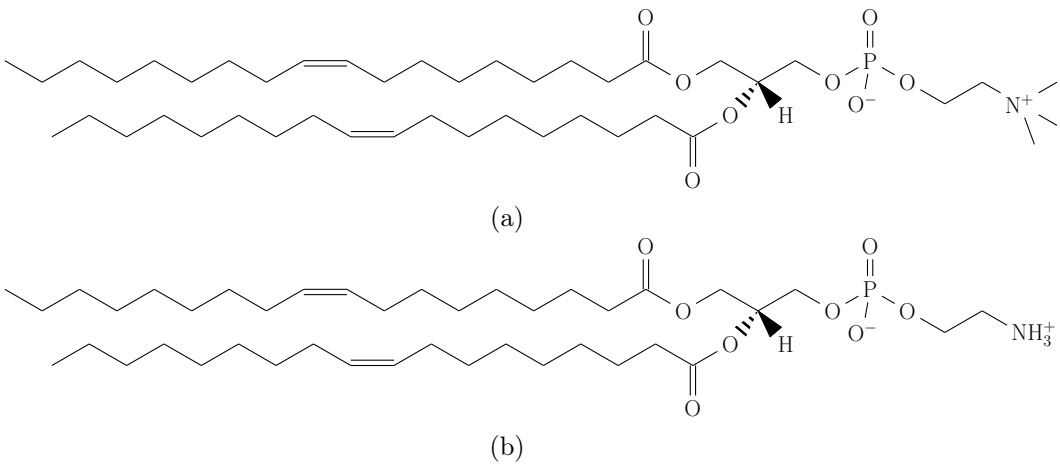

Figure 3.1: Chemical structure of the phospholipids (a) DOPC and (b) DOPE.

The supported lipid bilayer was formed via vesicle fusion of small unilamellar vesicles, about 100 nm in diameter. To form the vesicles the lipids were first individually dissolved in chloroform and then mixed in a glass vial to obtain a lipid solution where 20 wt% of the lipids consisted of DOPE and 80 wt% of DOPC. This composition was used since it has been shown to create lipid bilayers with high coverage on the nanowires[49]. The chloroform was slowly evaporated under nitrogen flow and the resulting lipid film was subsequently dried in vacuum over night, after which it was hydrated in phosphate buffered saline (PBS). The

vial was vortexed to form a lipid dispersion and left at 25 °C for about 1 h. The PBS was purchased in tablet form from Sigma-Aldrich (Darmstadt, Germany) and when mixed with MilliQ water a 137 mM NaCl, 2.7 mM KCl, and 10 mM phosphate buffer solution was obtained. The lipid dispersion was then sonicated using a tip sonicator to form the small unilamellar vesicles. The vesicle dispersion was put in contact with the substrate with nanowires, either in the GISANS measurement cell (described in chapter 4), in a flow cell for fluorescent imaging (described in section 3.1.3), or a flat SiO_2 substrate in a QCM-D cell.

3.1.2 Protein interactions

The effect of curvature of the lipid aqueous interface on the protein interaction with the membranes was investigated using two proteins, namely streptavidin and α-synuclein. Streptavidin is a specific binding protein while α-synuclein binding is non-specific. Streptavidin is a tetrameric 58.2 kDa protein which binds specifically to biotin with high affinity. One streptavidin molecule can bind up to four biotin molecules[61]. A lipid with a biotinylated head group, biotinyl cap PE (1,2-dioleoyl-sn-glycero-3-phosphoethanolamine-N-(cap biotinyl)), was added to the lipid mixture, described in section 3.1.1. The formed lipid bilayer was exposed to the streptavidin solution and the protein was allowed to attach to the biotinylated bilayer. The biotinyl cap PE lipid with purity of over 99% was purchased from Avanti Polar Lipids (Alabaster, AL, USA).

α-synuclein is one of three synuclein proteins that are abundant in the brain. It is concentrated in the nerve endings and is responsible for the release of neurotransmitters. α-synuclein has been found to be present in Lewy bodies and has been associated with Parkinson's disease[62,63]. It has also been shown that α-synuclein molecules have a higher binding affinity to curved bilayers compared with flat ones[64]. The protein was added to the sample cell after forming and characterizing the bilayer, as described in section 3.1.1.

3.1.3 Fluorescent imaging

The supported lipid bilayer was imaged using confocal microscopy[65,66]. This technique focuses on a particular focal plane while excluding the signal arising from other focal planes, thus allowing for sharper images and 3D reconstructions. The fluorescent used with confocal imaging also makes it possible to measure fluorescence recovery after photobleaching (FRAP)[67–69].

Fluorescence recovery after photobleaching

In FRAP, a small spot, about 3 µm, on the bilayer is bleached by means of a focused laser beam. The bleached spot is allowed to recover and the recovery time, τ_D, is used to calculate the diffusivity of fluorescent labeled lipids in the bilayer according to,

$$D = \frac{w^2}{4\tau_D}, \tag{3.1}$$

where w is the radius of the bleached spot. The above expression for the diffusion coefficient is that of a flat bilayer. A bilayer on a substrate with nanowires will have a larger surface area than on a flat substrate. This is due to the bilayer covering the full length of the nanowire. Since the diffusion time is dependent on the distance traveled by the lipids, the increased surface area of the nanowires needs to be taken into account to obtain the diffusivity on the nanowires[49,70],

$$D_{NW} = D(1 + \pi\, d\, l\, \rho_{NW}) \tag{3.2}$$

where d and l are the diameter and length of the nanowires respectively, and ρ_{NW} is the density of nanowires on the surface, i.e. the number of nanowires per unit area.

The intensity in the bleached spot, I_b, was divided by the intensity in a region in the same field of view but far from the bleached spot, I_{ref}, to account for loss in fluorescence in the whole field of view.

$$I_f = \frac{I_b}{I_{ref}} \tag{3.3}$$

The intensity, I_f, was then normalized to the intensity before bleaching. The normalized fluorescent intensity was plotted against time and fitted using the least-squares method, with SciPy `optimize.curve.fit`[71] in Python, to the function[49,72],

$$f(t) = (1-\gamma)\left(\mathrm{I}_0\frac{2\tau_D}{t} + \mathrm{I}_1\frac{2\tau_D}{t}\right)\exp\left(-\frac{2\tau_D}{t}\right) \tag{3.4}$$

to determine τ_D and γ, which is the immobile fraction in the bilayer. In the function, I_0 and I_1 are modified Bessel functions.

Fluorescent imaging set-up

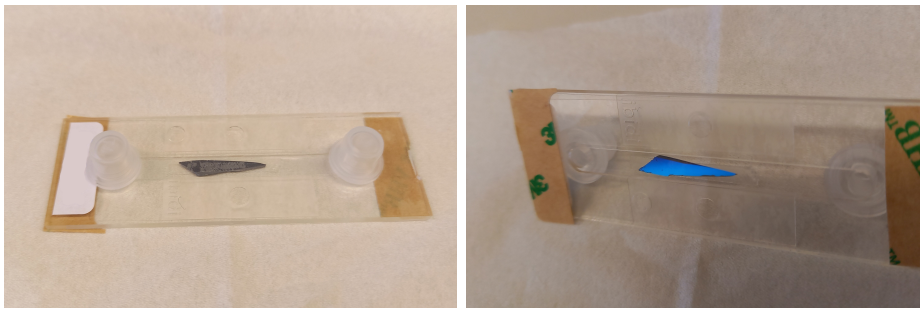

(a) (b)

Figure 3.2: Flow cell used for confocal microscopy measurements. a) shows the flow cell from the top with the nanowire sample in the middle, b) shows the flow cell from the bottom. The shiny blue color comes from the interference pattern from the nanowires.

The confocal imaging was performed on a small piece of the nanowire substrate with the nanowires facing down in the flow channel, see fig. 3.2. Prior to placing the nanowire substrate in the flow channel, it was carefully rinsed with 99.5% ethanol and dried with N_2. The flow channel was then sealed with a glass cover slide. A fluorescent dye was added to the lipid mixture before sonication as described in section 3.1.1, and the lipid vesicle dispersion was then passed through the flow channel. For static images 0.1 wt% Atto fluorescence dye (Attotec GmbH, Siegen, Germany) was used and for FRAP 0.1 wt% Cy5 fluorescence dye (ThermoFisher Scientific, Waltham, MA, USA) was used.

3.1.4 Quartz crystal microbalance with dissipation

Quartz crystal microbalance with dissipation (QCM-D) is a very sensitive technique for measuring adsorbed material on a quartz crystal. The measurement is carried out by monitoring the change in resonance frequency of the quartz crystal when material is added to the surface. The resonance frequency of the crystal decreases with the adsorption of material on the surface. Monitoring the dissipation gives a measurement of the viscoelastic properties of the adsorption film, where the dissipation increases with softer films[73]. To calculate the mass adsorbed to the surface of the crystal, Δm, the Sauerbrey equation[74] was used,

$$\Delta m = \frac{C}{n}\Delta F \tag{3.5}$$

where ΔF is the change in frequency, n is the overtone and

$$C = -\frac{t_q \rho_q}{f_0} \tag{3.6}$$

where t_q, ρ_q, and f_0 are the thickness, density and resonance frequency of the quartz, respectively. C is often called the crystal constant and has a value of $-17.7\,\mathrm{ng\,s\,cm^{-2}}$ for a 5 MHz crystal[75].

With QCM-D it is possible to monitor the kinetics during the formation of a supported lipid bilayer. It also allows the monitoring of interactions of proteins and other biomolecules with the supported lipid bilayer[76]. QCM-D was used to monitor the formation of the lipid bilayer on a flat silica surface, as described in section 3.1.1, and to monitor the long-term stability of the formed lipid bilayer.

QCM-D measurement set-up

The quartz crystals were first rinsed with MilliQ water, dried with nitrogen and washed with 99.5 % ethanol and again dried with nitrogen. The washed quartz crystals were then further cleaned in an air plasma for 5 min at 0.02 mbar using a plasma cleaner (Harrick Scientific Corp, model PDC-3XG, New York, USA). The cleaned crystals were placed in the Q Sense E4 QCM-D (Biolin Scientific, Gothenburg, Sweden), and MilliQ water was pumped through the cell at a rate of about $0.5\,\mathrm{ml\,min^{-1}}$ until a stable base line was found. Subsequently, phosphate buffered saline (PBS) was pumped through the cell at the same rate, again until a base line was found. When the base line was deemed stable, the change in frequency and dissipation was zeroed and the lipid vesicle dispersion, at a concentration of $0.1\,\mathrm{mg\,ml^{-1}}$, was pumped through the cell. A few ml of the vesicle dispersion was pumped through and was then left to incubate for 30 min to form a supported lipid bilayer. After the incubation the cell was rinsed with PBS and data was collected for a period of 8 h.

3.2 Results

3.2.1 Formation of the lipid bilayer

By using QCM-D it is possible to follow the formation of the lipid bilayer on the quartz crystal. Figure 3.3 presents QCM-D data, with both the change in

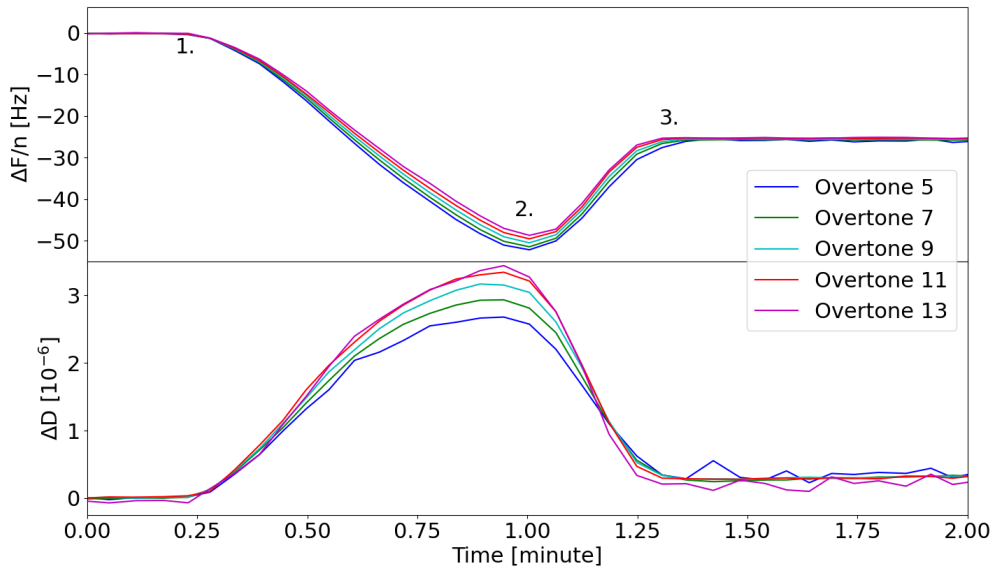

Figure 3.3: QCM-D measurement showing both the change in frequency (top) and in dissipation (bottom) during the formation of the lipid bilayer. The lipid vesicle dispersion was added to the QCM-D cell at 1. The initial decrease in frequency, at 2, and the increase in dissipation was an indication that vesicles have been bound to the surface. When the vesicles rupture, water was released and a bilayer was formed leading to an increase in the frequency, at 3, to a final value of around $-25\,\mathrm{Hz}$, and the decrease in dissipation to just above 0.

frequency (top) and change in dissipation (bottom) of the crystal, where the different lines are the overtones. The plateau represents the base line measured in PBS and is set to zero. The change in frequency and dissipation upon vesicle addition is measured relative to this baseline. When the lipids were added, at 1 in the figure, the frequency decreased and the dissipation increased. The initial change in frequency and dissipation is due to vesicles attaching to the surface, indicated with 2. The subsequent increase in frequency and decrease in dissipation were due to the rupture of the vesicles and release of water. The lipid bilayer was then spread on the surface and the change in frequency stabilized at around $-27\,\mathrm{Hz}$, seen at 3. This behaviour corresponds well with fig. 2*b*. in Keller and Kasemo[77], which shows the formation of a similar lipid bilayer on a quartz crystal.

The adsorbed mass, $\Delta m = 509 \pm 11\,\mathrm{ng\,cm^{-2}}$, on the crystal was calculated using eq. (3.5) and the frequency change after the bilayer formation. Using the adsorbed mass and the known molecular weight of the lipid, $M_W = 778\,\mathrm{g\,mol^{-1}}$,

it was possible to make a first rough estimate of the area per molecule. For this bilayer and lipid composition, the area per molecule then becomes 50 $Å^2$. In a review Nagle and Tristram-Nagle[78] reported on several different methods for measuring the area per molecule for a lipid bilayer consisting of only DOPC. The area per molecule was found to be between 60 and 80 $Å^2$, compared with the 50 $Å^2$ determined by QCM-D. It is however worth noting, that the adsorbed mass in QCM-D is obtained for all the material adsorbed to the surface, which includes water bound to the lipids.

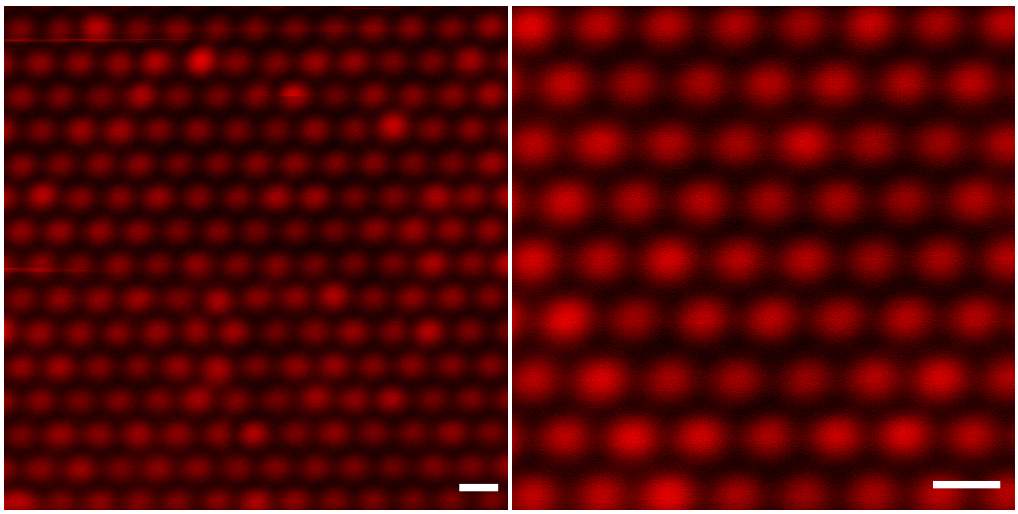

(a) (b)

Figure 3.4: Confocal microscopy images showing the lipid bilayer on the nanowires. Scale bars are 500 nm.

Confocal microscopy was used to image the formed lipid bilayer on the nanowires. Figure 3.4 shows static confocal images of the lipid bilayer on the nanowires. Both images clearly show the hexagonal pattern of the nanowires. The size of the bright spots do not reflect the actual size of the nanowires, since the fluorescent signal is spread out. The confocal images were taken in several different planes along the length of the nanowire. Since a fluorescent signal was measured from the full length of the nanowires it was possible to conclude that the lipid bilayer was formed along the whole length. In fig. 3.4a, some brighter spots are apparent, which were most likely due to vesicles trapped on the nanowire.

Figure 3.5 presents three images from the FRAP measurement. The first image, fig. 3.5a, was taken right after the bleaching of the bilayer. The bleached spot is visible in the top right-hand corner of the image. The second and third images, figs. 3.5b and 3.5c, were captured 10 s and 30 s after the bleaching, respectively.

In the image captured 10 s after the bleaching it is still possible to see a small bleached spot, which had completely disappeared after 30 s.

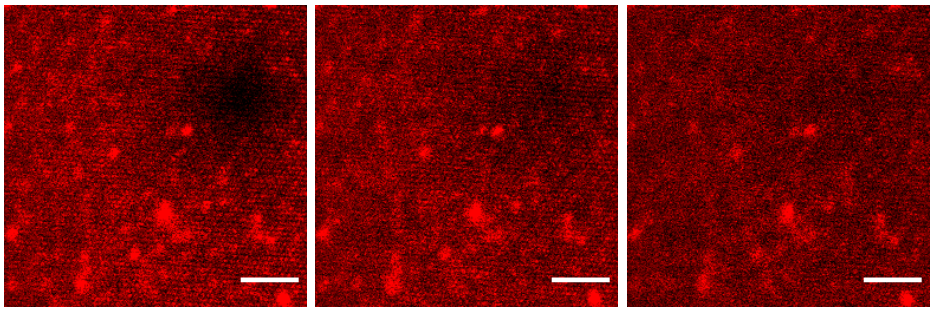

(a) (b) (c)

Figure 3.5: FRAP series. (a) time zero, the bleached spot is seen in the top right corner. (b) The same spot after 10 s and (c) after 30 s.

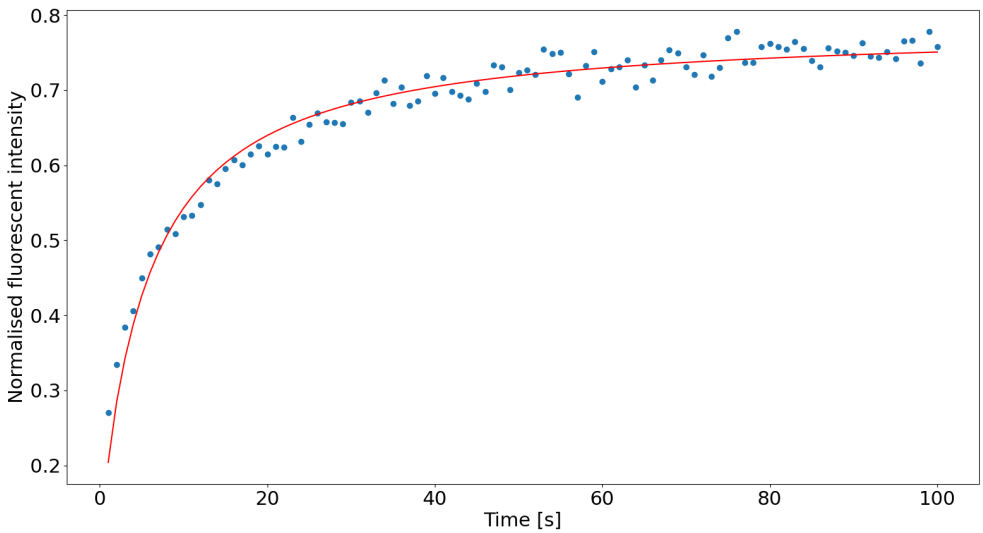

Figure 3.6: FRAP recovery curve, where the blue dots are the normalized fluorescent signal in the bleached spot. The red line is a fit to the function in eq. (3.4).

Figure 3.6 shows the fluorescence recovery plot from the same FRAP measurement as in fig. 3.5. The presented data were first divided by the intensity in a reference area of the same size not affected by the bleaching to account for the loss of fluorescence in the whole image. The red line was a fit to the data using the function in eq. (3.4). The recovery time, τ_D, and the immobile fraction, γ, were calculated from the fit. For this data the recovery time was $\tau_D = 4.6$ s and the immobile fraction was $\gamma = 0.2$. The diffusion coefficient, D, was calculated

using eq. (3.1) and the recovery time. However, since the diffusion took place on the nanowires, the diffusion coefficient was normalized to the surface area using eq. (3.2). The normalized diffusion coefficient was $D_{NW} = 0.500 \pm 0.003\,\mu m^2\,s^{-1}$, which corresponds well with previous studies [49].

3.2.2 Longevity of the bilayer on the nanowires

Chapters 4, 5 and 7 present how the lipid bilayer described herein was measured by means of GISANS and reflectometry. During those measurements the lipid bilayer was deposited on the surface and then left on the nanowires for up to several days. In order to verify the long-term stability of the bilayer an 8 h long, QCM-D measurement was performed.

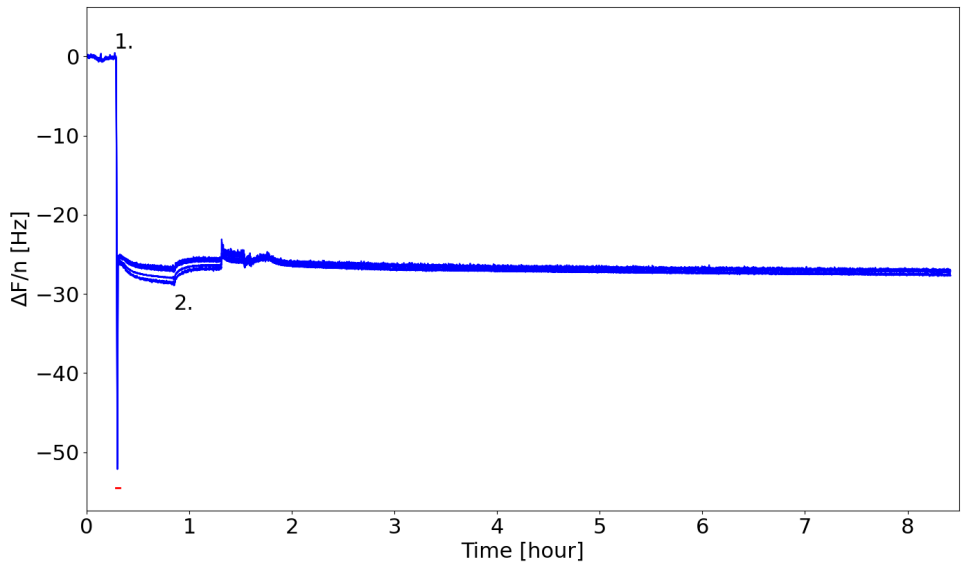

Figure 3.7: QCM-D curve of the full duration of the 8 h measurement. The small red line, in the bottom left corner, indicates where the formation of the bilayer took place which is seen in fig. 3.3.

Figure 3.7 shows the continuation of the measurement presented in fig. 3.3, which only covered the initial formation of the bilayer, represented by a small red line in the figure. The lipids were added at 1, and left to incubate until 2, when the remaining vesicles were rinsed from the cell with PBS. Before starting the rinse a slight decrease in frequency change could be observed, indicating that more material, vesicles, were attaching to the surface. After the rinse, all the vesicles

in the solution and those that had attached were rinsed off, leaving a bilayer on the surface. The PBS was left pumping at a slow rate, and after the 3 h mark the pump was stopped and the bilayer was left in the QCM-D cell immersed in PBS. As no change in the frequency for the full measurement was observed for at least 8 h it was concluded that the bilayer very likely remained intact on the surface for a long time.

3.3 Summary

This chapter describes how a lipid bilayer from a mixture of 80% DOPC and 20% DOPE can be formed on a flat surface, as observed with QCM-D, and on the nanowire surface, as observed with confocal microscopy. The bilayer was shown to be fluid and continuous over the full length of the nanowire. It has also been shown to be stable over at least a 8 h. The lipid bilayer formed with the vesicle fusion method, was investigated using GISANS and reflectometry, and the results are presented in the upcoming chapters.

Chapter 4

Grazing incidence small angle neutron scattering on nanowire arrays

The supported lipid bilayer discussed in the previous chapter was studied with grazing incidence small angle neutron scattering (GISANS). In a GISANS experiment a highly collimated neutron beam impinges on an interface at a shallow angle and is then scattered off the surface. Using GISANS, information is obtained on lateral structures at the interface. The supported lipid bilayer was also studied with confocal microscopy, as described in the previous chapter. However, the coverage and thickness of the bilayer could not be revealed with fluorescent imaging, and GISANS was therefore used to determine the structure and coverage of the lipid bilayer. This chapter is focused on the set-up of the different instruments, with discussions of both time of flight and monochromatic instruments. The collimation of the incident beam and illumination of the sample are described, as well as geometry, orientation and alignment of the sample at the different instruments. Furthermore, the overall patterns seen in the scattering are compared. The next chapter will describe a new method for analysing GISANS data.

4.1 Method

4.1.1 Grazing incidence small angle neutron scattering

In a grazing incidence small angle neutron scattering (GISANS) experiment a collimated neutron beam impinges on a surface with a very small angle, usually less than 1°, close to the critical angle of total reflection. The neutrons are then scattered at the interface and recorded by a 2D detector[6,79,80]. Figure 4.1 shows a schematic image of the geometry of the GISANS experiment at the VSANS instrument. The incoming neutron beam (red) comes in through the side of the silicon crystal and scatters at the interface between the Si crystal and D_2O. The orange line in the image shows the specular peak, which is where the angle of the incoming beam and the scattered beam are identical. The green lines in the image points to peaks, giving information about the structure of the sample.

The scattering pattern seen in fig. 4.1 can be described as a product of the structure, S, and form factor, F. The differential scattering cross-section is approximated by,

$$\frac{d\Sigma}{d\Omega} = S(Q) \cdot F^2(Q) + \text{background} \tag{4.1}$$

The structure factor describes how the different constituents in the sample are organized in relation to one another, in this case the nanowire array. The form factor describes the size and shape of the constituents of the samples, here the individual nanowires.

4.1.2 Experimental set-up

GISANS experiments were performed on three different beam lines, with KWS-1[81] at MLZ (Garching, Germany), with VSANS[82] at NIST (Gaithersburg, USA) and with SANS2D[83] at ISIS (Didcot, UK). Two different nanowire samples were used, a 600 µm thick, *2 inch*, 50.8 mm in diameter Si wafer and a large square Si crystal, both described in chapter 2. The Si wafer was used at the KWS-1 beam line and was placed in a custom built aluminum sample holder, seen in fig. 4.2a. The sample was positioned with the back of the wafer facing down, see figs. 4.2b and 4.2c. In fig. 4.2c, the red line shows the direction of the neutron beam and indicates how the beam hits the back of the Si wafer.

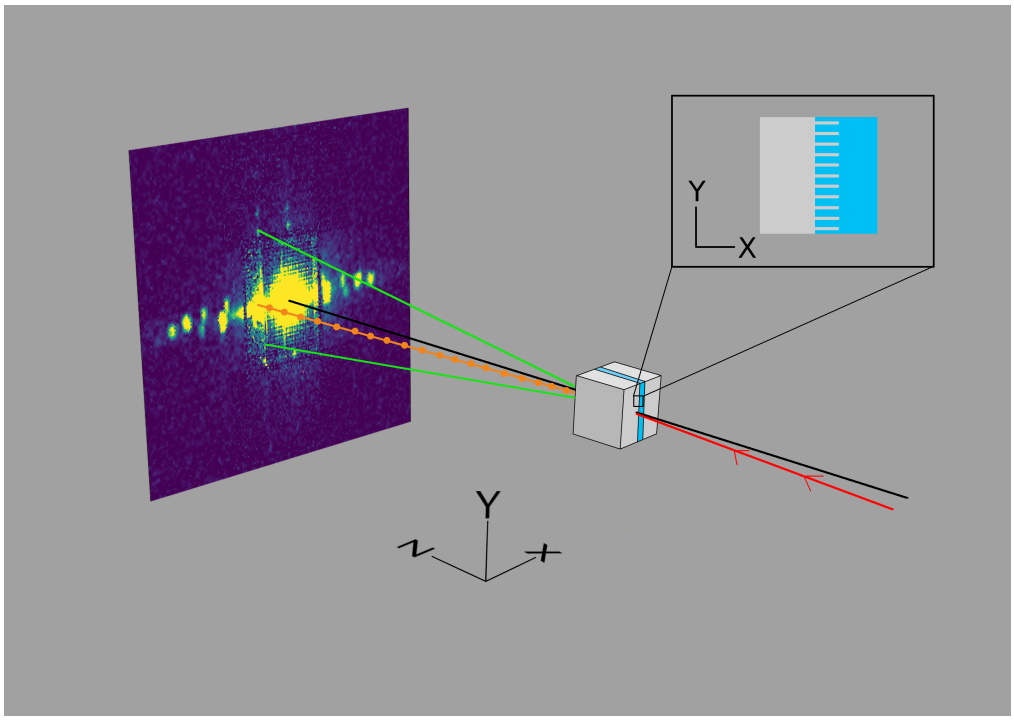

Figure 4.1: Schematic overview of a GISANS geometry, specifically for the VSANS instrument. The black line shows the center which is parallel to the surface of the Si crystal, with the incoming beam, red with arrows, at a small angle to the center line. The orange line with dots marks the specular, or reflected, peak, where the incoming angle and exit angle are the same. The green lines point to two peaks. The insert shows the Si crystal with the nanowires which are perpendicular to the surface of the crystal. For all detector plots shown in this chapter, the nanowires will be oriented parallel to the x-axis, as illustrated in the insert.

The large square substrate described in chapter 2 was used at VSANS and SANS2D. The sample was placed in a similar but slightly larger sample holder as that described by Rennie et al.[84] and seen in fig. 4.3. With this sample holder and the larger thickness of the substrate, i.e. 6.25 mm, it is possible for the neutron beam to enter through the side of the Si crystal, approximately where the red laser dot can be seen in fig. 4.3. When the neutron beam comes in through the back of the Si wafer, part of the beam will be reflected and scattered at that interface. The incident beam angle would also need to be lower than the critical angle for the air-Si interface, in order to have significant intensity at the next interface, i.e. the D_2O-Si interface. With the beam coming in through the side of the crystal, the second scattering interface will be avoided and the incident beam angle can be closer to the critical angle of the D_2O-Si interface.

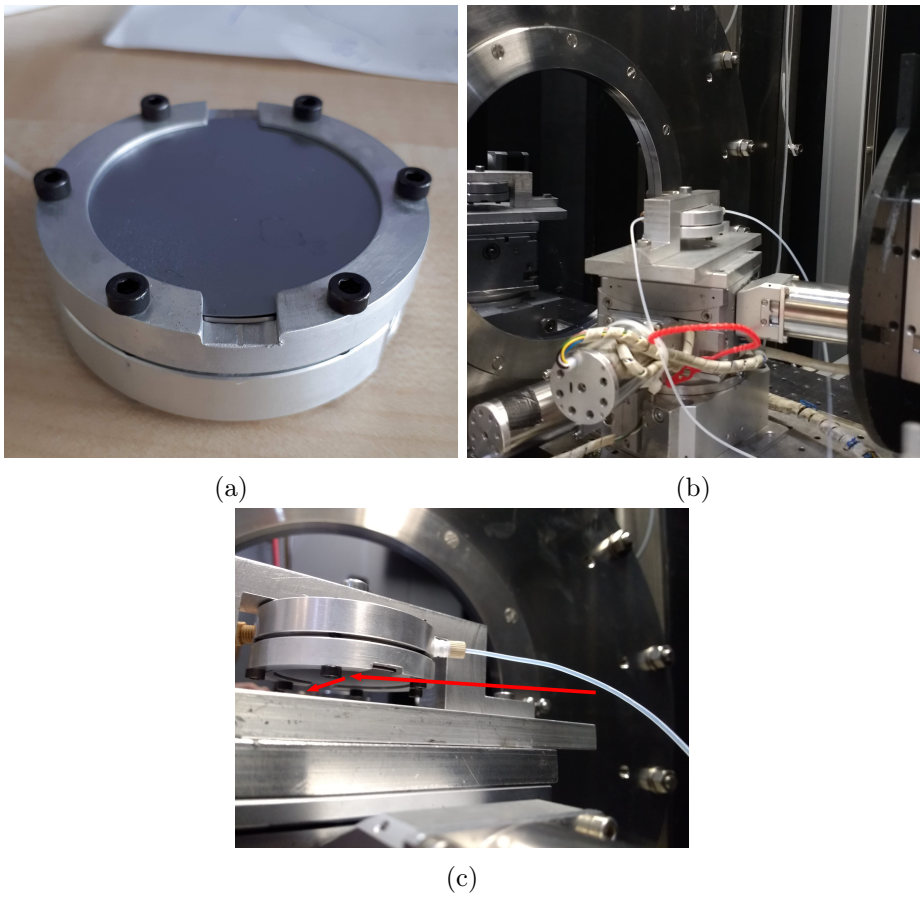

Figure 4.2: Sample and sample holder used at KWS-1. (a) Shows the sample holder and the back of the Si wafer. (b) The sample at the KWS-1 beam line. (c) The neutron beam comes to the interface from the back of the Si wafer, shown with red arrows. Seen behind the sample in (b) and (c) is the neutron beam guide window.

Prior to the sample being placed in either the small round holder or the large square holder, it was cleaned by immersing the sample in 1 % solution of Neutracon (Decon Laboratories Ltd. Hove, East Sussex, UK) for about 20 min. The sample was then carefully rinsed with MilliQ water, submerged in MilliQ and then rinsed once more. The last steps involved rinsing the sample with 99.5 % ethanol and then carefully drying it with nitrogen. SEM imaging revealed that the lipids were successfully cleaned from the surface, and that the nanowires were undamaged by the cleaning procedure.

The supported lipid bilayer was prepared using vesicle fusion as described in chapter 3. The prepared vesicle dispersion was pumped into the cell using a

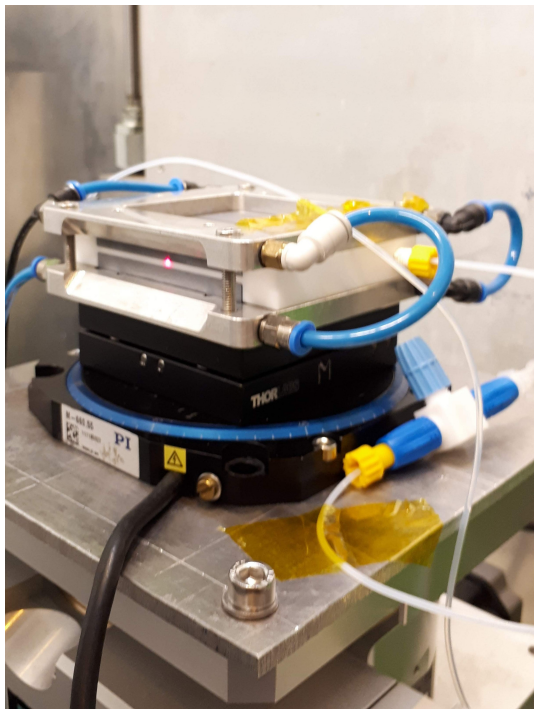

Figure 4.3: Sample holder for the larger Si crystal, here seen at the SANS2D instrument. The neutron beam enters from the side of the Si crystal, approximately at the red laser dot.

syringe pump at a speed of $0.5\,\mathrm{ml\,min^{-1}}$. The bare nanowires and the supported lipid bilayer on the nanowires were measured in D_2O, and in water matched to Si (cmSi), which corresponds to a mix of 62% D_2O and 38% H_2O.

KWS-1

Figure 4.4 shows a schematic diagram of the KWS-1 instrument. The first part of the instrument, indicated by 1, is the neutron beam guide which transports neutrons from the source to the velocity selector, placed at 2. The velocity selector creates a monochromatic neutron beam, and can select wavelengths between 4.5 and 12 Å, as well as 20 Å, with a resolution of $\Delta\lambda/\lambda = 10\%$. After the velocity selector comes the collimation line, at 3, consisting of a number of moveable, 1 m long neutron guides, which are used to change the source to sample distance. The sample position is at 4, followed by the 20 m long evacuated detector tube. The detector is placed at 5 and can be moved between a distance of 1.5 and 20 m from the sample position. The detector is a position sensitive

2D scintillator detector, with a spatial resolution of $5.3 \times 5.3\,\mathrm{mm}^2$. The available Q-range at KWS-1 is 0.0007 to $0.5\,\mathrm{Å}^{-1}$ depending on the chosen wavelength and the position of the detector[81].

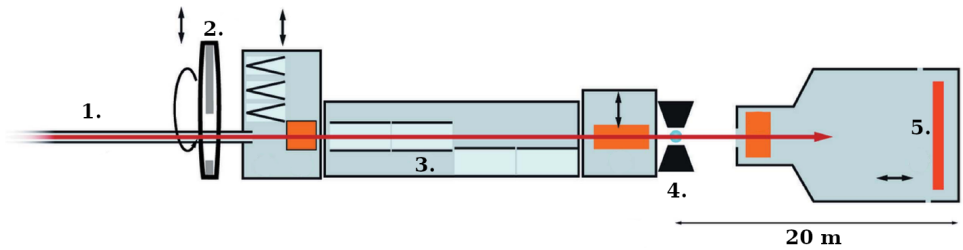

Figure 4.4: Schematic diagram of the KWS-1 beam line. The instrument starts with (1) a neutron beam guide, and (2) the velocity selector. After the velocity selector is (3) the collimation line, followed by (4) the sample position, and lastly (5) the 2D detector. Schematic diagram from Feoktystov et al.[81].

At KWS-1 the *2 inch* wafer substrate (600 µm thick, one side unpolished) was used and placed with the back of the wafer facing down, as can be seen in fig. 4.2. The neutron beam came in from the back of the Si wafer and was scattered at the interface between the Si and the water. Three sample to detector distances were used, 1.5 m, 8 m and 20 m. For these detector settings, a wavelength of 5 Å was used with incident beam angles of 0.5°, 0.65° and 0.8°. For the 20 m detector distance an additional wavelength of 12 Å was also used with incident beam angles of 0.65°, 0.8° and 1.1°. The sample was measured in D_2O for 2 h at the 20 m detector distance, and for 1 h for the 8 and 1.5 m detector distances. Slightly longer measurements times were used for the cmSi measurements.

VSANS

VSANS stands for very small angle neutron scattering and is the name of a beam line located at the Center for Neutron Scattering at NIST in the USA. Figure 4.5a shows a schematic diagram of the VSANS beam line. The beam line has a velocity selector (1) that creates a monochromatic beam with wavelengths between 4.5 and 12 Å with $\Delta\lambda/\lambda = 12\%$. The beam line is 45 m long and has three moveable detector arrays in an evacuated detector tube. The front and middle detectors are ^{3}He tube detectors with a resolution of 8 mm, and the rear detector is a scintillator detector with a 0.2 mm resolution. The front and middle carriages have four detector panels each, and the rear carriage has one detector panel. The three detector carriages can be placed at varying distances from the

sample in order to measure different Q ranges with appropriate resolution with the various detectors, and a single wavelength and collimation set-up [82].

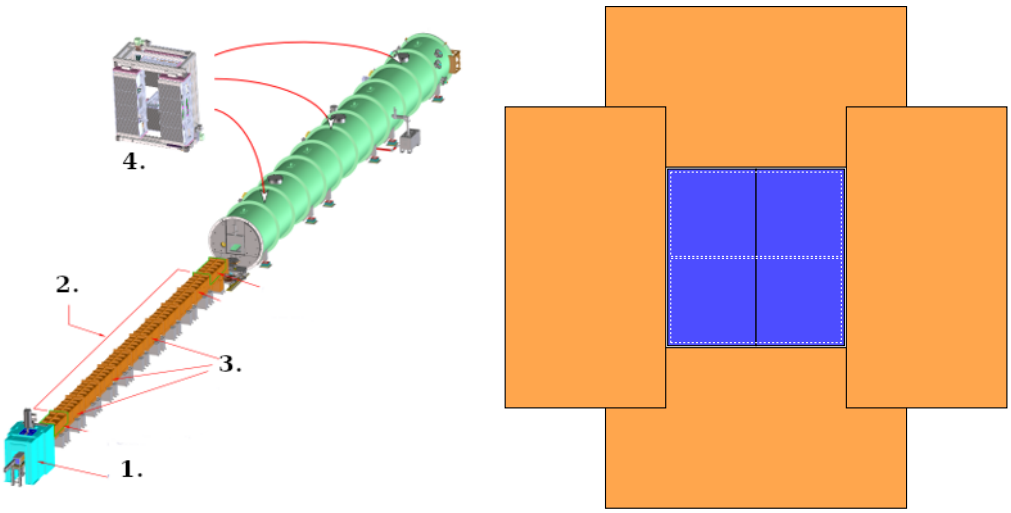

(a) (b)

Figure 4.5: (a) Schematic diagram of the VSANS beam line, provided by NCNR [82]. The instrument has a (1) velocity selector for wavelengths between 4.5 to 12 Å, (2) moveable neutron guide with (3) multiple converging apertures and slits. In the detector tube, there are (4) three moveable detector carriages. (b) Schematic illustration of the detector set-up used at the VSANS instrument. The orange panels are the four front detectors, overlapping slightly, placed at 8 m from the sample, and with an opening in the middle. The blue panels are the middle detectors, placed at 20 m from the sample, with the left and right panels touching, and with the top and bottom panels behind.

During the experiment the front and middle detector carriages were used and placed at 8 m and 20 m, respectively. Figure 4.5b shows the positioning of the detector panels of the front and middle carriages. The front detectors (orange in the image) were positioned to create an opening in the center to let neutrons through to hit the middle detectors (blue in the image). The middle detectors were placed with two of them touching, with the other two behind, the dashed lines in fig. 4.5b. A wavelength of 6 Å was used, with an incident beam angle of 0.55°. The nanowire sample, without and with a lipid layer, was measured in D_2O and in cmSi. The lipid layer contained biotinylated lipids, and measurements with the streptavidin protein, described in section 3.1.2, were also performed. Each measurement was 2 h long.

SANS2D

SANS2D is situated at the second target station at ISIS Neutron and Muon source in the UK. The ISIS source is a pulsed spallation source and SANS2D works as a time of flight (ToF) instrument. In contrast to KWS-1 and VSANS, it is with a ToF instrument possible to carry out measurements with multiple wavelengths at the same time. The wavelength band that can be used at SANS2D is from 1.75 to 14 Å. Figure 4.6 shows a schematic diagram of the SANS2D instrument, which has five removable, 2 m long, neutron guides providing incident collimation from 2 to 12 m. The detectors are positioned in a vacuum tank and consist of two 0.96 m^2 ^{3}He multiwire proportional counters. They can be placed at distances between 2 and 12 m from the sample position. Depending on the collimation and detector set-up a Q-range of 0.002 to 3 $Å^{-1}$ can be obtained[83].

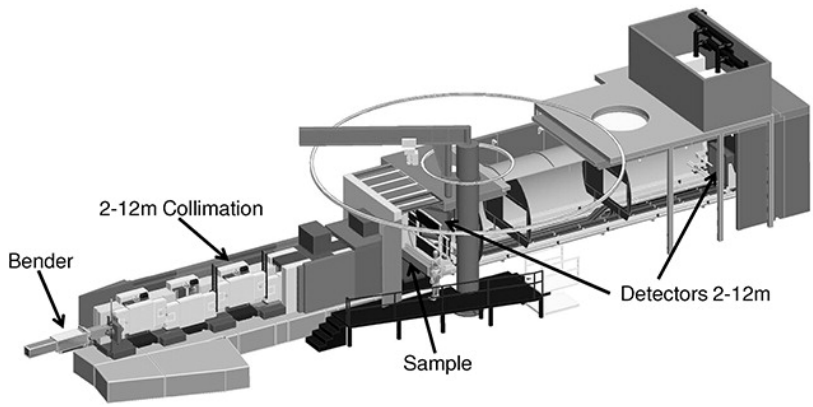

Figure 4.6: A schematic diagram of the SANS2D instrument. The instrument employs the ToF capabilities of ISIS and can use wavelength from 1.75 to 14 Å. The two detectors are positioned in a vacuum tank and can be placed at a distance between 2 and 12 m from the sample. Schematic diagram from Heenan et al.[83]

The large square sample was used and placed horizontally with the nanowires facing down, see fig. 4.3. A wavelength range of $1.75 - 12.5$ Å was used, with an incident beam angle of 0.28°. To increase the flux, a short collimation length was used. The collimation was set to be 6 m and the distance to the detector was set at 12 m. The sample was measured for about 8 h[1] for each sample configuration.

[1] At ISIS measurements are not usually defined simply in time but as accumulated proton current on the target, measured in µA h. The samples were measured for a total of 320 µA h, which, if the beam stays on, corresponds to about 8 h.

4.1.3 Scattering length density

The scattering length densities (SLD), ρ, of the different compounds are shown in table 4.1. The SLD of a compound is calculated from the values of scattering lengths, b_i, tabulated by Sears[85], of the different atoms in the material, and the known molecular volume, V_M, or compound density, ϱ_M, according to,

$$\rho = \frac{\sum_{i=1}^{N} b_i}{V_M} \tag{4.2}$$

where V_M can be calculated through,

$$V_M = \frac{M}{\varrho_M N_a} \tag{4.3}$$

where M is the molecular weight and N_a is the Avogadro constant.

Table 4.1: SLD for the different materials used throughout this work. *representing two acyl chains, †20 wt% DOPE and 80 wt% DOPC

Material	**SLD** $[10^{-6}\text{Å}^{-2}]$	ϱ_M $[\text{g cm}^{-3}]$
H_2O	−0.56	0.997[86]
D_2O	6.35	1.10[86]
Silicon	2.07	2.33[86]
Amorphous silica	3.48	2.20[86]

Material	**SLD** $[10^{-6}\text{Å}^{-2}]$	$\mathbf{V}_\text{M}$ $[\text{Å}^3]$
DOPC[87–89]	0.30	1294
-head	1.88	319
-tail*	−0.214	975
DOPE[78]	0.34	1227
-head	2.48	252
-tail*	−0.21	975
Lipid mixture†	0.315	1280
-head	2.006	305
-tail*	−0.214	975

4.2 Results

4.2.1 Monochromatic measurement

Figure 4.7 shows 2D plots of the scattering from bare nanowires (left) and lipid covered nanowires (right) measured with the VSANS instrument in D_2O. What can be seen in the image are a number of peaks concentrated along vertical and horizontal lines. Given the distance between the nanowires the peaks are all expected to be of high order. The orientation of the sample, shown in fig. 4.1, puts the long axis of the nanowires parallel to the x-axis of the detector. This means that the variation of intensity in the peaks seen on the horizontal line of the detector is mainly due to the length of the nanowires. The intensity in the peaks along the vertical lines, perpendicular to the long axis of the nanowires, is mainly due to the radius of the nanowires. The addition of the lipid to the nanowires makes it possible to see a clear difference between the two scattering patterns in fig. 4.7. The peaks in the horizontal direction become more intense and the peaks in the vertical direction lose some of their intensity. Also noticeable in fig. 4.7 is that the peaks in the vertical direction have a slight tilt. This tilt away from the xy axes is due to a minor misalignment of the nanowire array with respect to the detector.

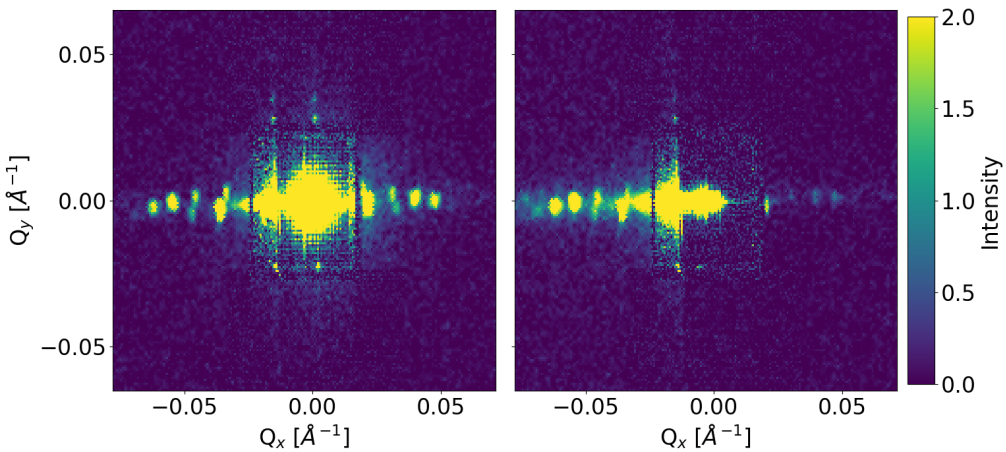

Figure 4.7: The scattering from nanowires without (left) and with (right) a lipid layer measured in D_2O at the VSANS instrument.

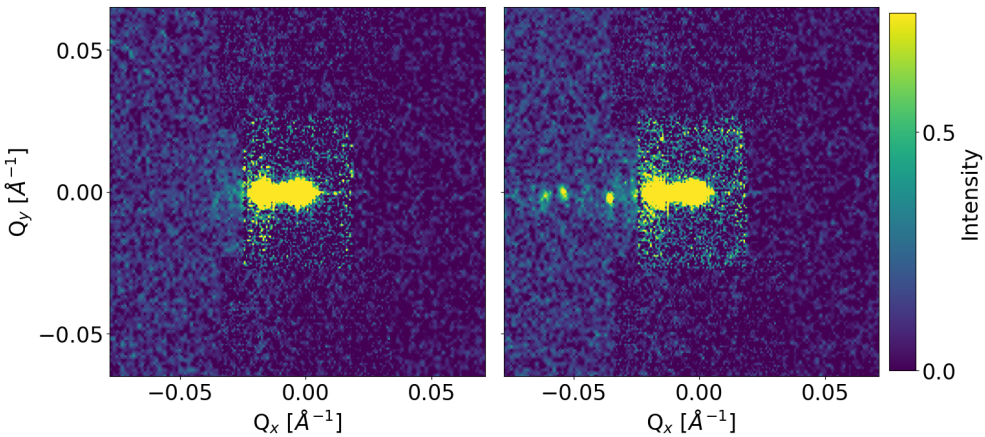

Figure 4.8: Scattering from nanowires measured in cmSi at the VSANS instrument. The figure on the left is for the bare nanowires and the figure on the right is for the nanowires covered with a lipid layer.

Figure 4.8 shows 2D plots of scattering from bare nanowires (left) and lipid covered nanowires (right) measured in water contrast matched to Si (cmSi) at the VSANS instrument. When comparing the bare nanowires measured in cmSi with the bare nanowires measured in D_2O the large difference in scattering pattern is obvious. Since the nanowires are made of Si they are almost completely masked when measured in cmSi, and the only visible peaks are the direct beam and the reflected beam. In the right figure, some peaks, due to the lipid bilayer, are visible. These are very weak compared with those measured in D_2O. This is, in part, because the lipid layer is quite thin, but also because the contrast between the lipid and the surrounding solvent is smaller in cmSi than in D_2O. The difference in SLD between the lipid and D_2O is about three times larger than the difference in SLD between the lipid and cmSi.

Figure 4.9 shows data from the KWS-1 instrument. The scattering patterns are for the nanowires in D_2O, with the bare sample to the left and with lipid to the right, using the *2 inch* wafer. The measurements were performed with a wavelength of 5 Å and the detector at 8 m. Comparing the two images there is a very clear difference after the addition of the lipid with many more peaks visible in the right figure. During this experiment the sample was placed horizontally with the beam coming in through the back of the Si wafer. The placement of the sample can be seen in fig. 4.2, where the red line depicts the beam direction.

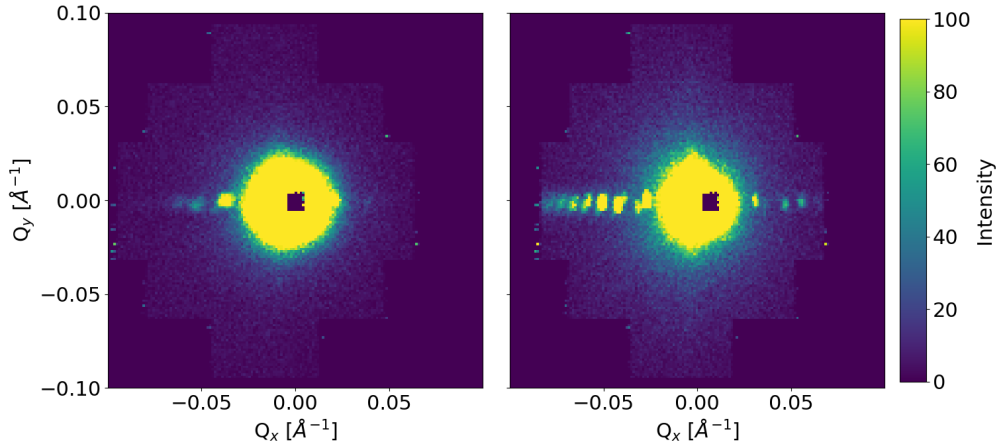

Figure 4.9: Scattering data from the KWS-1 instrument measured in D_2O. The image to the left corresponds to bare nanowires and the image to the right to nanowires with lipid. The square in the middle of both images is the beam stop.

A very noticeable feature seen in both images in fig. 4.9 is the high intensity around the square beam stop at $Q_x = Q_y = 0$. This intensity is due to small angle scattering from over-illumination of the sample. The incident angle in this measurement was 0.5° and the slit at the sample was 50 mm × 4 mm. This gave rise to a beam footprint of 500 mm along the beam direction, which meant that the sample was over-illuminated by a factor of 10, given that the diameter of the sample, or length of the sample in the beam, was 51 mm. Since the footprint of the beam was so much larger than the actual sample, a large portion of the beam hit the sample holder and gasket surrounding the sample cell, thus causing the small angle scattering seen around the beam stop. Due to this scattering, peaks at low Q were not visible.

A direct comparison between the data measured at VSANS and at KWS-1 is challenging. First, two different samples were measured at the instruments. The largest difference between them were the size, where the sample at KWS-1 consisted of a thin, about 0.6 mm thick, 50.8 mm in diameter wafer, whereas the sample at VSANS was a 65 mm × 65 mm × 6.25 mm Si block. Since the wafer used at KWS-1 was so thin, it was not possible for the neutron beam to come in through the side of the sample, which was the case at VSANS. At VSANS, a much narrower slit, i.e. 0.5 mm, was used at the sample giving a beam footprint of about 52 mm. This smaller footprint, and larger sample, meant that no over-illumination occurred. Compared with the KWS-1 measurement, almost no small angle scattering from the sample holder was seen in VSANS data. This means that peaks at low Q are clearly visible at VSANS, whereas

they were hidden due to strong small angle scattering at KWS-1. However, what is comparable between the measurements at VSANS, shown in fig. 4.7, and at KWS-1, shown in fig. 4.9, is the clear difference seen when the lipids are added.

4.2.2 Time of flight measurement

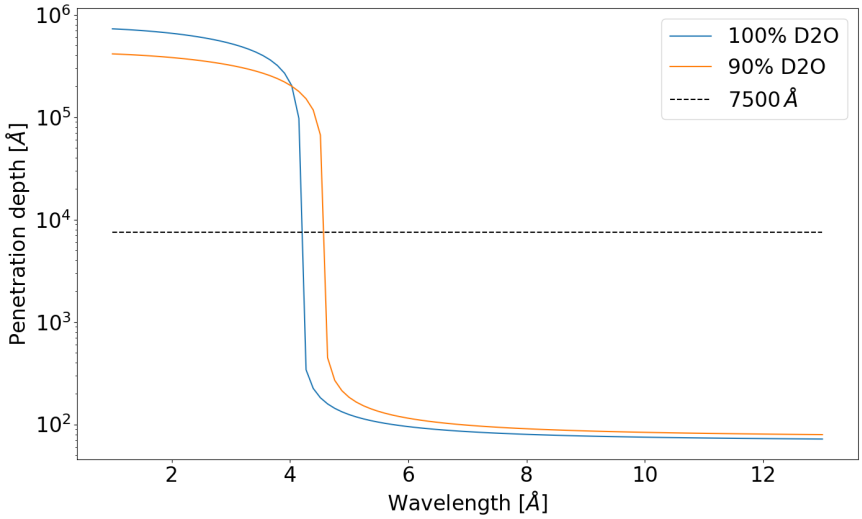

Figure 4.10: The penetration depth in D_2O, and in D_2O with 10 % H_2O from a Si interface at an incident beam angle of 0.28°. The dashed line indicates the length of the nanowires. The penetration depth was calculated using equations from Nouhi et al. [80].

Scattering for multiple wavelengths can be recorded simultaneously when using time of flight (ToF) measurements, thus making it possible to probe different depths in a single sample at the same time. Figure 4.10 shows the penetration depth at Si/D_2O and Si/90 vol%D_2O interfaces with an incident beam angle of 0.28°, which is what was used at SANS2D. At a wavelength of about 4 Å there is a sharp decrease in penetration depth. This is the critical wavelength of the interface. After a ToF measurement, the data for the various wavelengths can be divided up and different structures visualized.

ToF GISANS was used at the SANS2D beam line with wavelengths ranging from 1.75 to 12.5 Å. Figure 4.11 shows measurement data from the nanowires in D_2O. The left image shows the full wavelength band, and the right one displays the data in the wavelength band from 4.0 to 6.0 Å. The scattering from the 7500 Å long nanowires will be largest when the penetration depth of the neutrons

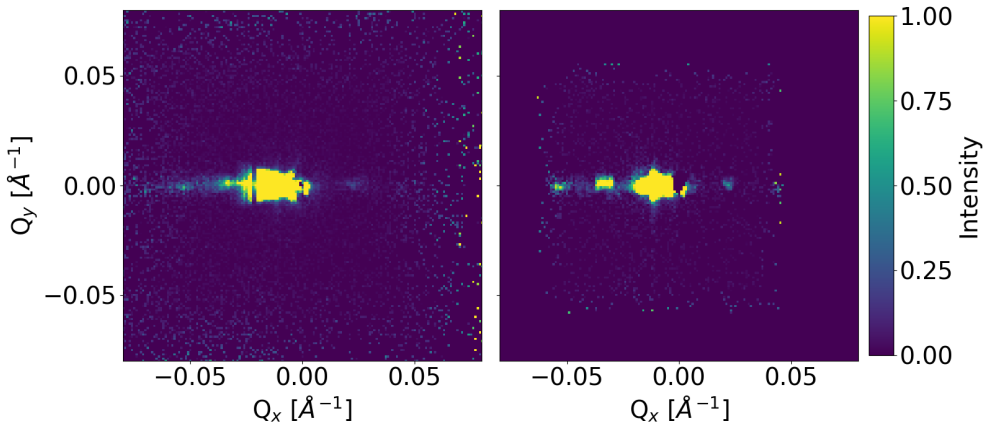

Figure 4.11: Time of flight measurement at SANS2D. The left image is for the full wavelength band, from 1.75 to 12.5 Å. The right image is for the wavelength band 4.0 to 6.0 Å. Both images are for the nanowires in D_2O.

slightly exceeds the full length of the nanowires. As seen in fig. 4.10, a wavelength around, or below, the critical wavelength is needed to penetrate the length of the nanowires. The right image in fig. 4.11 shows the scattering from just above the critical wavelength, and it is possible to see some clear peaks arising from the nanowires. At SANS2D the maximum in flux is between $4 - 5$ Å [90]. This is likely why the peaks are visible in the wavelength band just above the critical wavelength, and not as visible below the critical wavelength.

The Q-range will decrease when shorter wavelengths are excluded. Figure 4.12 shows a cut along Q_x for four different wavelength bands. The full wavelength band, with wavelengths from 1.75 to 12 Å, has the largest Q-range, with a $Q_{\max}$ of above 0.1 Å^{-1}. The smallest Q-range is seen for the wavelength band 10 to 12 Å, with a $Q_{\max}$ of just above 0.02 Å^{-1}. That Q-range is too small to resolve any peaks from the nanowires. The penetration depth at that wavelength band is also too small to penetrate the length of the nanowires, and scattering will only take place at the surface.

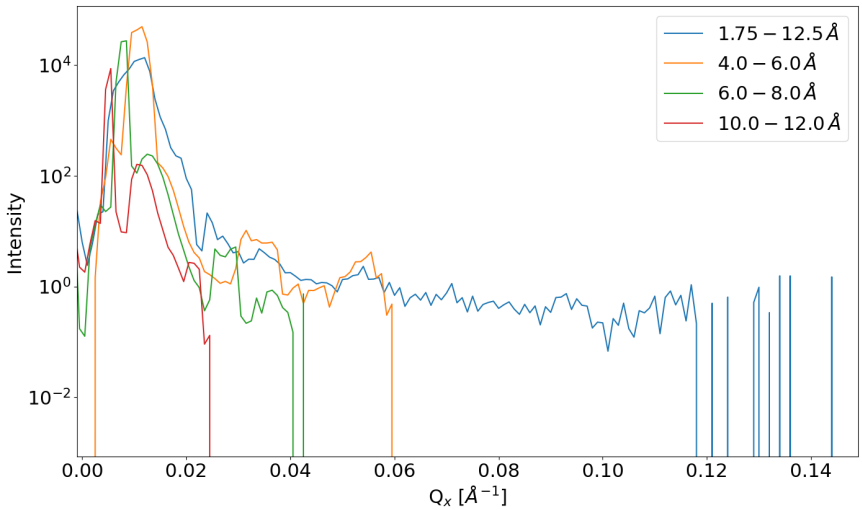

Figure 4.12: Cut along Q_x showing peaks, and the extent of the Q-range for the different wavelength bands for bare nanowires in D_2O.

4.2.3 Rotation of the hexagonal lattice

The hexagonal pattern of the nanowires can be compared with a two-dimensional hexagonal crystal. In the same way as a crystal can be rotated to probe different crystal planes, so can the nanowire array. When the hexagonal pattern is rotated the neutron beam will see different patterns. Figure 4.13 shows eight measurements from KWS-1 where the nanowire array was rotated. The hexagonal pattern was rotated 1° between each of the first five images. Between the fifth and the sixth image the pattern was rotated 2°, and then 5° to the seventh image. Between the seventh and last image the pattern was rotated 30°. The data were recorded using a 5 Å wavelength and with the detector at 20 m. The square at $Q_{xy} = 0$ is the beam stop, and at $Q_x = -0.02$ is the reflected beam. Further to the left in the image it is possible to see a peak. That peak is moving with the rotation of the sample, indicating that different directions of the hexagonal pattern are probed. In the last image it is not possible to distinguish between the small angle scattering around the beam stop and the reflected beam. The sample holder has a cut out, seen in fig. 4.2a, which was mostly aligned with the beam. When the sample was rotated by as much as 30°, more of the beam then hits the aluminum sample holder and the metal screws to the side of the cut out, causing more small angle scattering.

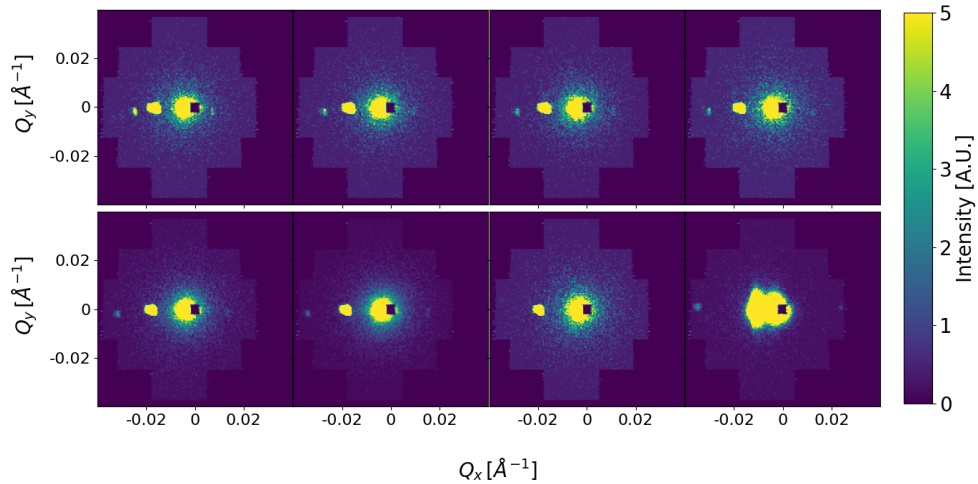

Figure 4.13: Showing rotation of the hexagonal lattice. Between each of the first five images the hexagonal pattern is rotated by 1°. The pattern is then rotated by 2° to image six, and another 5° to image seven. The hexagonal pattern is lastly rotated by an additional 30°, seen in the last image. The data were measured using 5 Å wavelength and a sample to detector distance of 20 m.

At VSANS the hexagonal pattern was also rotated. Figure 4.14 shows a horizontal cut, along Q_x, for three different rotations. These rotations are all relative and, unfortunately, not connected with how the hexagonal pattern is structured on the surface of the Si. The data for +15° in the figure are shown as a 2D plot in fig. 4.7. What can be seen in fig. 4.14 is that the peaks change position depending on the rotation of the sample, which is also seen in the data from KWS-1 shown in fig. 4.13.

One reason to rotate the hexagonal pattern is to have as intense peaks as possible. In the data from the VSANS instruments it was observed that some rotation directions of the hexagonal pattern resulted in more intense peaks, especially for the peaks in the vertical direction. To be able to optimize the best rotation of the pattern each rotation would have to be measured for a long time, since the intensity in the peaks was low, especially for the peaks perpendicular to the long axis of the nanowires. For example, the data shown in fig. 4.14 was measured for 2 h for every rotation, and even after a 2 h measurement, only one of the three data sets had visible peaks in the vertical direction. Peaks in the vertical direction are important for the analysis presented in the next chapter.

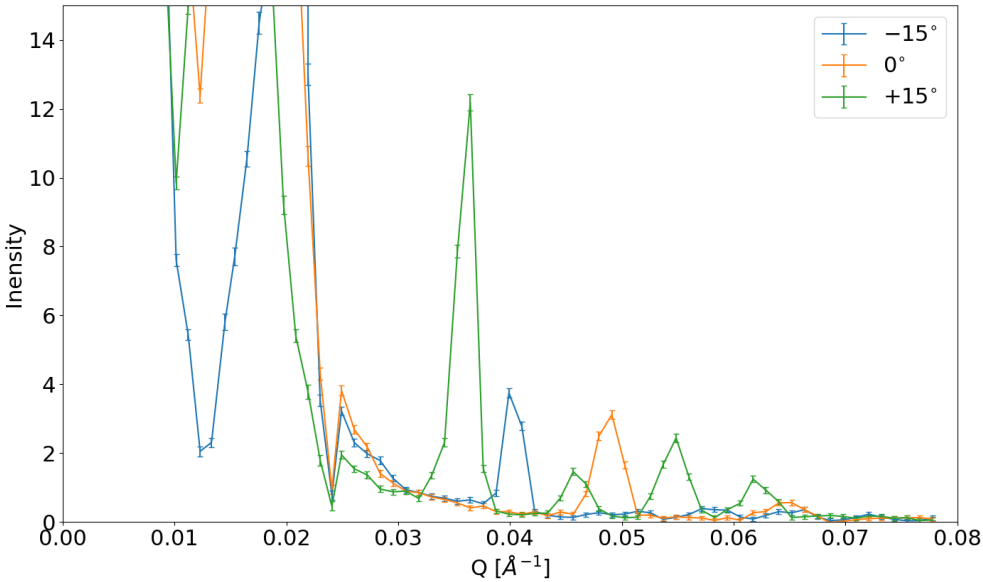

Figure 4.14: Horizontal cuts in data from VSANS at three different rotations angles of the hexagonal pattern for the bare nanowires in D_2O.

4.2.4 Protein interactions

At VSANS a biotinylated lipid was added to the lipid bilayer and the protein streptavidin was allowed to attach to the lipids, as described in section 3.1.2. Streptavidin has a high affinity to biotin and is therefore a good protein to test protein attachment to a lipid bilayer. Figure 4.15 shows horizontal cuts, along Q_x, of the scattering from the bare nanowire, from nanowires with lipid and with lipid and protein. There is no significant difference in the intensity when going from a lipid layer to a lipid layer with protein. This might be due to a too low concentration of protein, which would give a small difference in scattering length density.

At SANS2D α-synuclein was used, where both a hydrogenated and deuterated version of the protein was used. Unfortunately, no noticeable difference was observed when adding the protein. This, again, might be due to too low concentration of protein. The difference observed after addition of the protein at VSANS and at SANS2D was not sufficient to allow for a more detailed analysis. Further analysis of the protein data has therefore not been conducted.

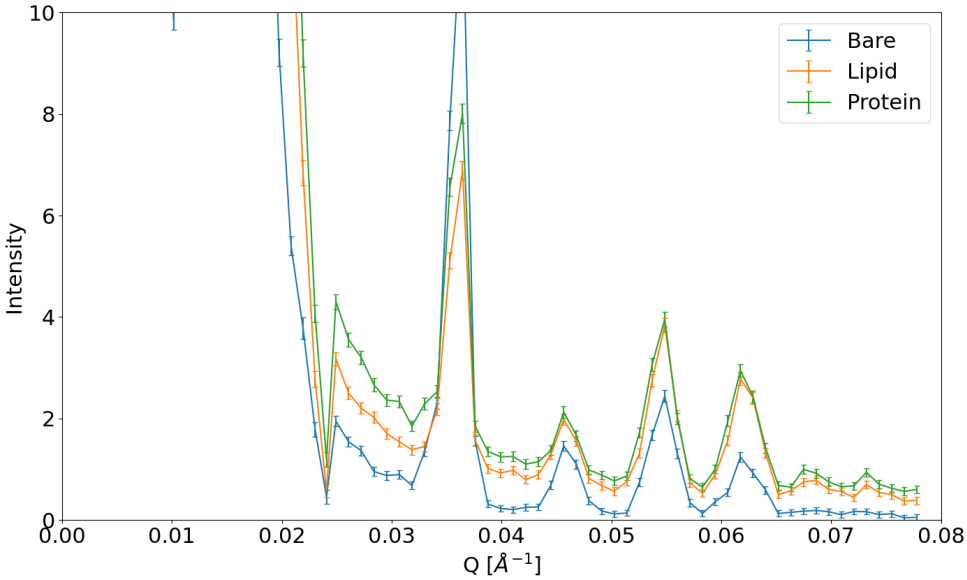

Figure 4.15: Horizontal cuts in data from VSANS showing the scattering from bare nanowires, nanowires with a lipid layer, and with a lipid layer with added protein.

4.3 Summary

This chapter has shown GISANS data from three different instruments, KWS-1, VSANS, and SANS2D. The first two instruments used a monochromatic neutron beam, whereas SANS2D uses time of flight. Two different samples have been used, a thin round *2 inch* Si wafer, and a thick square Si crystal, both with a hexagonal array of Si nanowires. The instruments had varying set-ups with slits and detectors. The slits close to the sample determined the size of the footprint of the beam on the sample. Due to the slit set-up at KWS-1, the footprint was about a factor of 10 larger than the size of the sample. This over-illumination resulted in a large portion of the beam hitting the sample holder, thus causing diffuse small angle scattering. This small angle scattering was seen as a continuously increasing intensity towards the beam stop in fig. 4.9 and obscured peaks at low Q. At VSANS the larger sample was used, and the slit set-up used reduced the diffuse small angle scattering, thereby making it possible to observe peaks even at lower Q.

At SANS2D time of flight was used to carry out measurements at multiple wavelengths at the same time. This technique has the advantage that many different depths in the sample can be probed simultaneously. However, for a

given wavelength the neutron flux is generally lower than at a monochromatic instrument, which means that the measurement times need to be longer to compensate for the lower flux per wavelength. For the present sample most of the interesting structures were seen just above the critical wavelength and a monochromatic instrument using that wavelength might have been a better choice.

The optimal instrument to obtain the best data for the nanowire sample would be a monochromatic instrument with a wavelength of about $4-5\,\text{Å}$ with a small sample slit and high resolution detector. Using a wavelength at the critical wavelength would be useful in order to both have scattering from the full length of the nanowire and also some scattering from the surface of the sample. Having a small slit at the sample would minimize the footprint of the beam and then also minimize diffuse scattering from the sample holder. A high resolution detector would be needed to resolve peaks, specifically at small Q. Using a small slit at the sample and a narrower wavelength spread would lead to a decrease in neutron flux, which would lead to longer measurement times.

Chapter 5

Quantitative analysis of GISANS data arising from a nanowire array

This chapter presents a newly developed method for analyzing GISANS data, which was used to analyze the GISANS data from the VSANS instrument presented in the previous chapter. Current methods for analyzing GISANS data often include taking line cuts and model fitting, frequently using the distorted wave Born approximation[91–93], to the intensity along these lines. Such methods are used to calculate the scattering for individual samples, however, the main interest of this work was to determine the change when adding lipids to the Si nanowires.

As mentioned in the previous chapter, a scattering pattern can be described as the product of the structure factor, S, and the square of the form factor, F, with an addition of a background. The structure factor is determined by the correlation between objects in the sample and the form factor describes the size and shape of those objects. In this case, the structure factor would be determined by hexagonal array nanowires, and the shape of the nanowires would be approximated as the form factor of a cylinder. The addition of the lipid does not alter the structure of the nanowire array, meaning that the structure factor remains unchanged. Based on this, a simplified analysis method using ratios of form factors was developed. The method compares ratios of peak intensities arising from the nanowire array with and without the lipid layer, with ratios of calculated form factors. The advantage of using ratios of peak intensities is that it is not necessary to determine the structure factor of the sample, and, to a first approximation, it is possible to ignore issues such as refraction.

As in the studies described in the previous chapter, the sample consisted of a regular array of hexagonal nanowires. A lipid layer, comprising of 20 wt% DOPE and 80 wt% DOPC, was subsequently added to the nanowires. The formation of the lipid layer was done via vesicle fusion, described in chapter 3.

5.1 Method

5.1.1 Derivation of scattering form factors for multi-shell cylinders

The developed method, which is described in-depth in the next section, is based on the ratios of form factors. The form factor that best describes the nanowires is that of a cylinder. In order to model an oxide and a lipid layer on the nanowires, different shells are added to the cylinder form factor. The derivation of the form factor for multi-shell cylinders is presented here.

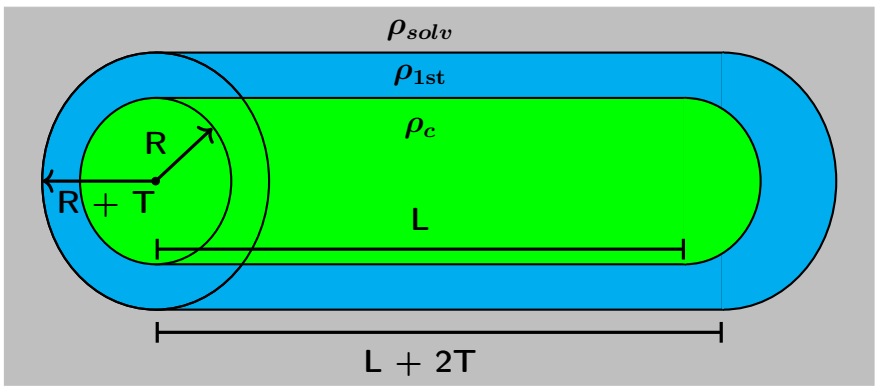

Figure 5.1: Schematic diagram of a core-shell cylinder, showing the length, L, the radius, R, and the thickness, T, of the shell. The core, shown in green, has a scattering length density (SLD) given by ρ_c, the first shell, shown in blue, has an SLD given by ρ_{1st}. The core and the shell is surrounded by a solvent with an SLD given by ρ_{solv}.

The form factor for a solid uniform cylinder[4] is given by

$$F_c(Q) = 2\Delta\rho V \frac{\sin\left(Q\frac{1}{2}L\cos\alpha\right)}{Q\frac{1}{2}L\cos\alpha} \frac{J_1\left(QR\sin\alpha\right)}{QR\sin\alpha}, \tag{5.1}$$

where Q is the scalar amplitude of the scattering vector, $\mathbf{Q}$, $\Delta\rho$ is the difference in scattering length density between the cylinder, ρ_c, and the solvent, ρ_{solv}. L,

and R are the length and radius of the cylinder, respectively, where the volume, V, is calculated from those parameters. The parameters are shown schematically in fig. 5.1. J_1 is the first order Bessel function, and α is the angle between the axis of the cylinder and the scattering wave vector, $\mathbf{Q}$. Figure 5.2 shows the square of the form factor for three different radii. The form factors are calculated using eq. (5.1) for a 7500 Å long cylinder with and $\alpha = 89.5°$. Instrument resolution is included in the plotted form factors.

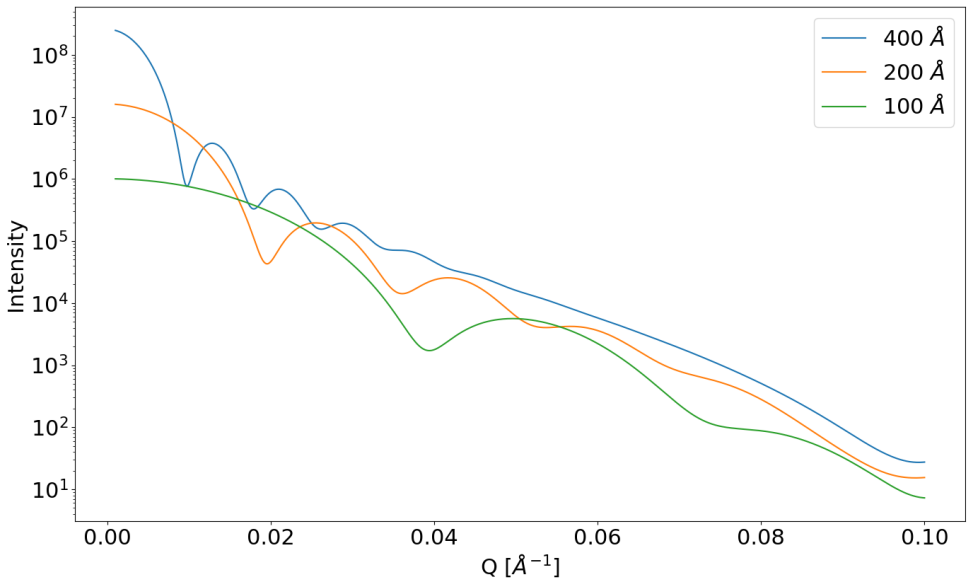

Figure 5.2: Square of cylinder form factors for three different radii. The cylinder was 7500 Å long and with an angle between the cylinder axis and the scattering vector, $\alpha = 89.5°$.

To model the oxide and lipid layers on the nanowires, the scattering form factor needs to be rewritten to include shells. The scattering form factor from *only* a shell is obtained by calculating the form factor for a large cylinder with a total volume of V_1, which includes a core and a shell, and then subtracting the scattering from the core with a volume V_c. The scattering amplitude from *only* the shell thus becomes

$$F_{1\text{st}} = (\rho_{1\text{st}} - \rho_{solv})V_{1\text{st}}P_{1\text{st}} - (\rho_{1\text{st}} - \rho_{solv})V_cP_c \tag{5.2}$$

Here the subscript indicates the shell, where 1st means the first shell. $P_{1\text{st}}$ and P_c are the scattering function of a cylinder with one shell and that of a solid

cylinder, respectively.

$$P_c = \frac{\sin\left(Q\frac{1}{2}L\cos\alpha\right)}{Q\frac{1}{2}L\cos\alpha}\frac{2J_1\left(QR\sin\alpha\right)}{QR\sin\alpha} \tag{5.3a}$$

$$P_{1\text{st}} = \frac{\sin\left(Q\left(\frac{1}{2}L+T_{1\text{st}}\right)\cos\alpha\right)}{Q\left(\frac{1}{2}L+T_{1\text{st}}\right)\cos\alpha}\frac{2J_1\left(Q(R+T_{1\text{st}})\sin\alpha\right)}{Q(R+T_{1\text{st}})\sin\alpha} \tag{5.3b}$$

where $T_{1\text{st}}$ is the thickness of the first shell. $V_{1\text{st}}$ in eq. (5.2) is defined by

$$V_{1\text{st}} = \pi(R+T_{1\text{st}})^2(L+2T_{1\text{st}}) \tag{5.4}$$

The scattering from *only* the shell, eq. (5.2), is then added to the scattering of a solid cylinder, eq. (5.1), to give the form factor of a core-shell cylinder, $F_{\text{core-shell}} = F_c + F_{1\text{st}}$, which gives,

$$\begin{aligned} F_{\text{core-shell}} = (\rho_c-\rho_{solv})V_cP_c + \Big[(\rho_{1\text{st}}-\rho_{solv})V_{1\text{st}}P_{1\text{st}} - (\rho_{1\text{st}}-\rho_{solv})V_cP_c\Big] = \\ \rho_cV_cP_c - \rho_{solv}V_cP_c + \rho_{1\text{st}}V_{1\text{st}}P_{1\text{st}} - \rho_{solv}V_{1\text{st}}P_{1\text{st}} - \rho_{1\text{st}}V_cP_c + \rho_{solv}V_cP_c \end{aligned} \tag{5.5}$$

Canceling out the $\rho_{solv}V_cP_c$ terms and collecting the other terms leads to,

$$\begin{aligned} F_{\text{core-shell}}(Q) &= (\rho_c-\rho_{1\text{st}})V_c\frac{\sin\left(Q\frac{1}{2}L\cos\alpha\right)}{Q\frac{1}{2}L\cos\alpha}\frac{2J_1\left(QR\sin\alpha\right)}{QR\sin\alpha} \\ &+ (\rho_{1\text{st}}-\rho_{\text{solv}})V_s\frac{\sin\left(Q\left(\frac{1}{2}L+T\right)\cos\alpha\right)}{Q\left(\frac{1}{2}L+T\right)\cos\alpha}\frac{2J_1\left(Q(R+T)\sin\alpha\right)}{Q(R+T)\sin\alpha}, \end{aligned} \tag{5.6}$$

where the subscripts c and 1st for ρ and T represent the core and the first shell, respectively [94].

The core-shell equation can be generalized further to include an arbitrary number of shells. This is done in the same way as going from a solid cylinder to a cylinder with one shell. The scattering from only the outermost shell is given by calculating the form factor for a large cylinder with volume V_N, and then subtracting the scattering from the core and inner shells. The scattering from the outermost shell is then added to the scattering from the core and inner shells. Simplified this gives,

$$F_{\text{core-N:shells}} = (\rho_c - \rho_i)V_c P_c + (\rho_i - \rho_{i+1})V_i P_i + \ldots + (\rho_N - \rho_s)V_N P_N, \quad (5.7)$$

where the subscript N is the number of shells and

$$V_k = \pi\left(R + \sum_{i=1}^{k} T_i\right)^2 \left(L + 2\sum_{i=1}^{k} T_i\right), \quad (5.8)$$

for $k = 1, 2, \ldots, N$.

5.1.2 Analysis method

The geometry of the GISANS experiment at VSANS is shown in fig. 4.1. The incoming beam is shown in red, and the specular reflected beam is shown in orange. The green lines points to peaks, which are located along the horizontal line, corresponding to the x-axis of the detector, and vertical lines, along the y-axis of the detector. The insert in the top right corner shows the nanowires on the Si substrate. The x-axis of the detector is defined such that the long axis of the nanowires is parallel to the x-axis.

The scattering pattern shown in fig. 4.1 can be described as a product of the structure factor, S, and the form factor, F, of the sample, with an addition of a background, which gives the differential scattering cross-section,

$$\frac{d\Sigma}{d\Omega} = S(\mathbf{Q}) \cdot F^2(\mathbf{Q}) + background \quad (5.9)$$

where Ω is the solid angle and $\mathbf{Q}$ is the scattering vector. The structure factor, which describes the hexagonal array of the nanowires, will give rise to peaks with a very small separation in Q. Due to the resolution of the instrument, the structure factor would be smeared to be an almost continuously smooth function. The structure factor also remains constant before and after the formation of the lipid layer. The form factor depends on the shape and composition of the nanowires and is likely what is dominating the scattering. The subsequently deposited lipid bilayer will also change the form factor. The background is expected to be slightly higher after the formation of the lipid layer, due to the large amount of hydrogen in the lipids. The background is subtracted from the integrated peak intensities before taking the ratio for the lipid covered nanowires

and the bare nanowires. This leaves the structure factor and the form factor in eq. (5.9),

$$\left.\frac{d\Sigma}{d\Omega}\right|_{NW} = S(\mathbf{Q}) \cdot F^2_{NW}(\mathbf{Q}) \tag{5.10a}$$

$$\left.\frac{d\Sigma}{d\Omega}\right|_{lipid} = S(\mathbf{Q}) \cdot F^2_{lipid}(\mathbf{Q}). \tag{5.10b}$$

Dividing the scattering observed for the nanowires with lipids (eq. (5.10b)) by the scattering from the nanowires, eq. (5.10a), cancels the structure factor and leaves the ratio of the two form factors, F^2_{lipid}/F^2_{NW}.

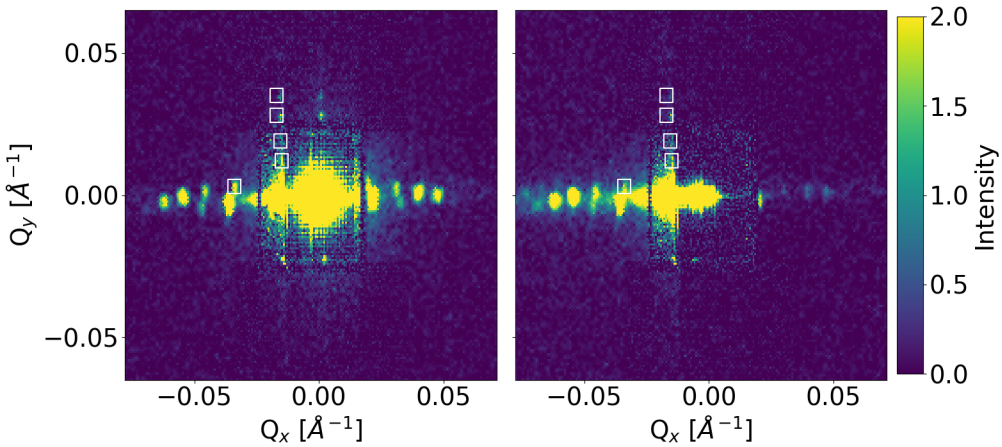

Figure 5.3: 2D scattering image of the data used for the ratio calculations. The white boxes in the figure represent the region of interest for which the integrated intensity was calculated. The peaks are not situated along a straight line, which is due to the sample slit and alignment of the sample. This figure is also shown in fig. 4.7.

For the analysis, peaks in the vertical direction of the detector image were selected, shown as white boxes in fig. 5.3. It is seen in the figure that the peaks are not situated along a straight line. The reason for this is related to the sample slit and the alignment of the sample. The peaks in the vertical direction result from the scattering perpendicular to the nanowires, which means that the intensities in the peaks along Q_y arise mainly from the radial structure of the nanowires. The thickness of the lipid layer is about one order of magnitude smaller than the radius of the nanowires. This may be compared with the difference between the

layer thickness and the nanowire length which is about two orders of magnitude. It is, therefore, convenient to use peaks whose intensity is sensitive to the radial structure of the nanowires, as they are expected to show the largest changes when the lipid is added.

Peaks in the horizontal direction of the detector, see fig. 5.3, are the results of scattering parallel to the long axis of the nanowires. This means that the intensity in those peaks arises mainly from the length of the nanowires, which are approximately 750 nm long. Phase differences, due to a difference in optical path length, may occur when the neutron beam traverses such long structures. These phase differences can then modify the scattering pattern, and even change positions of the minima and maxima of the form factors[95]. When using the ratio calculations, these effects must be taken into consideration, which would complicate the calculations. Since the radius of the nanowires is much smaller, there is no need to consider these phase differences, which is another reason to use the peaks in the vertical detector direction.

The analysis considers the integrated intensity of regions of interest around sharp peaks, seen as white boxes in fig. 5.3. The scattering intensity further from the regions around the peaks comes primarily from either background or diffuse scattering. The background at small Q arises from scattering from the sample holder, and at large Q, largely from incoherent scattering. The background was estimated by taking the total intensity, away from the peaks, in areas of the same size as those used to measure the peak intensity. A total of 10 such areas were chosen and the mean intensity in these areas was used as the background to be subtracted. The 10 background areas were all chosen from the top left corner of fig. 5.3, with a minimum Q of $Q_x = -0.03\,\text{Å}^{-1}$ and $Q_y = 0.03\,\text{Å}^{-1}$. The same regions of the detector were evaluated for the nanowires with and without lipids, both for determining the peak intensities and for the background calculation.

The ratios of the peak intensities obtained on nanowire substrates with and without a lipid layer were compared with the corresponding ratios of form factors calculated from models of the multilayer cylinders, see section 5.1.1. The form factors were calculated for a cylinder with one shell, eq. (5.6), which corresponds to the nanowires with a thin oxide layer, and for a cylinder with two shells, eq. (5.7) with $N = 2$, representing the nanowire with both an oxide layer and a lipid layer. The oxide layer was set to a thickness of 10 Å with an SLD of $3.48 \times 10^{-6}\,\text{Å}^{-2}$. The effects of instrumental resolution were included in the calculated form factors prior to the ratio calculation. The model for the oxide layer was kept the same for both the bare nanowires and those covered with lipids, whereas the thickness and SLD were allowed to change. The best fit was determined by reduced χ^2_ν,

$$\chi^2_\nu = \frac{\chi^2}{\nu}, \tag{5.11}$$

where ν is the number of degrees of freedom, and χ^2 is the uncertainty weighted sum of the squared deviations.

5.2 Results

The method described in the previous section was used to determine the thickness and coverage of the lipid layer on the Si nanowires. The integrated peak intensity ratios were compared with calculated form factor ratios for cylinders with added shells. The shells represented the silicon oxide and a lipid layer. The thickness and SLD were kept the same for the oxide layer throughout the fit, whereas the thickness and SLD for the lipid layer was allowed to vary. Figure 5.4 shows a reduced χ^2 map, and the figure displays a quite clear minimum in reduced χ^2 at around a thickness of 30 Å and an SLD of just over 4×10^{-6} Å^{-2}.

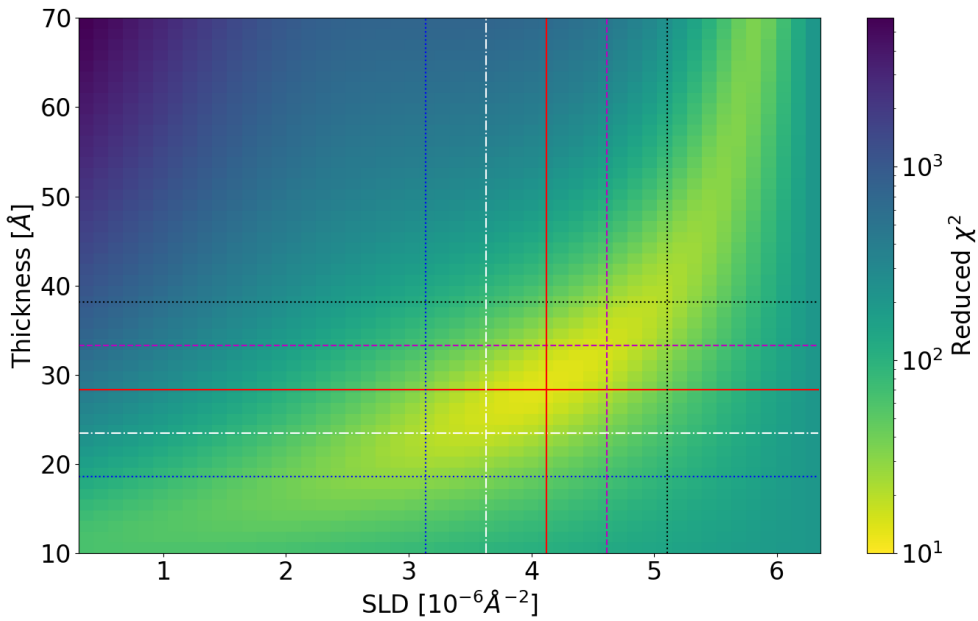

Figure 5.4: The reduced χ^2 for all the combinations of SLDs and layer thicknesses. The lines in the plot correspond to the cuts shown in fig. 5.5.

The minimum in fig. 5.4 can be more clearly seen in fig. 5.5, which shows cuts in the χ^2 map. The line colors in both plots correspond to each other, and the red line shows the position of the minimum, which signified a reduced χ^2 of 13. The clear minimum in figs. 5.4 and 5.5 shows that the developed method was sensitive to the lipid layer thickness.

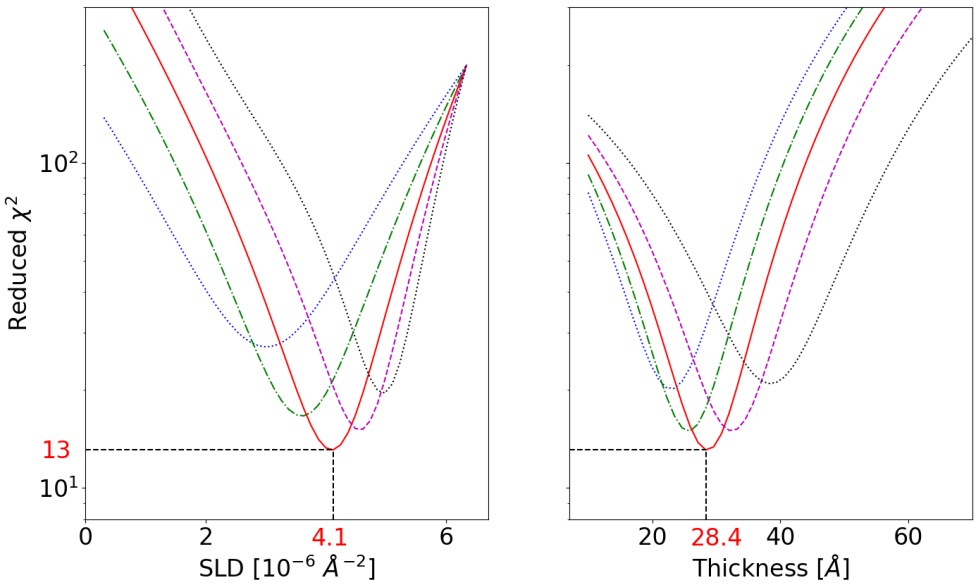

Figure 5.5: Cuts along the lines shown in fig. 5.4. The red line gives the minimum of the reduced χ^2 with the corresponding values of SLD and layer thickness.

Often, GISANS scattering patterns have clearly visible peaks, however, these can be weak and the scattering in the background can sometimes be more intense. Methods for analyzing GISANS data based on model fits to 2D scattering patterns, or line cuts, limited by counting statistics might be dominated by trying to find a fit to the background rather than the actual data. Since the method presented here uses ratios of integrated peak intensities, more information can be directly obtained as compared with methods of analysing GISANS data based on counting statistics.

The fit to the GISANS data can be seen in fig. 5.6. Comparing the obtained SLD of the layer to the SLD of the pure lipid, which is about 0.3×10^{-6} Å^{-2} (see table 4.1 in chapter 4), indicates that some buffer, D_2O, might be included in the layer. The volume fraction of lipid, ϕ_{lipid}, in the mixed layer is calculated as

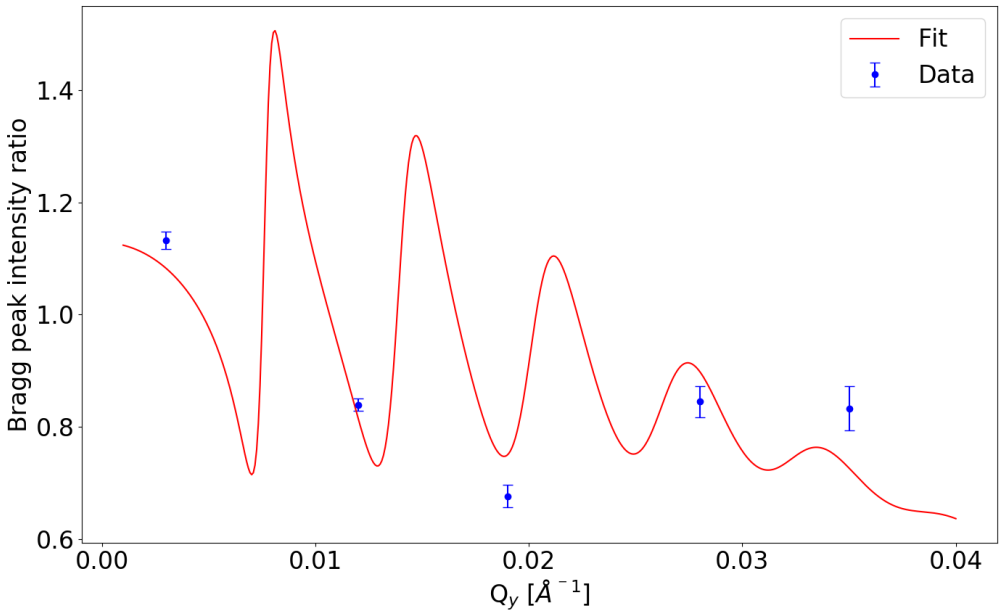

FIGURE 5.6: The blue dots show the ratio of the integrated peak intensity for the nanowires with a lipid layer and bare nanowires in D_2O. The fit gives a thickness of 28.4 ± 4.3 Å and an SLD of $4.1 \pm 0.5 \times 10^{-6}$ Å^{-2} of the layer. The reduced χ^2 of the fit is 13. The SLD of the layer corresponds to a lipid fraction of about 0.37.

$$\phi_{lipid} = \frac{\rho_{mix} - \rho_{D_2O}}{\rho_{lipid} - \rho_{D_2O}} \tag{5.12}$$

where ρ_{mix} is the SLD of the mixed layer, ρ_{lipid}, and ρ_{D_2O} are the SLD for the lipid and D_2O, respectively. Using this equation gives a lipid volume fraction of about 0.37.

The lipid layer will have a curved structure around the nanowires. Curved lipid bilayers have previously been studied using lipid vesicles. Lipid vesicles can be obtained by extruding lipid dispersions through filter membranes. The size of the vesicles and the number of bilayers the vesicles contain can be controlled by the pore size of the filter and the number of times the lipid dispersion is passed through the filter. DOPC vesicles with a radius of about 600 Å measured with SANS were found to have a bilayer thickness of about 38 Å [96–98]. For vesicles with a lipid mixture of 1:1 DOPC and DOPE, and with a radius of 200 Å, the bilayer was approximately 37 Å [99]. These studies did not report on the density of the lipid in the layers. In a vesicle the bilayer would be curved

in two directions, on the other hand, the bilayer on the nanowires would only be curved in one direction, i.e. around the nanowires. These two factors make a direct comparison challenging. Mitchell and Ninham[100] also states that lipid molecules in a spherical shell are expected to be more tightly packed than in a cylinder.

The thickness of the lipid layer obtained from the fit was 28 Å, which is slightly thinner than what is reported for vesicles. A reason for this could be that the lipid tails were tilted or interpenetrating. The layer also contained a large amount of solvent, about 63 %, which is possibly due to the layer being patchy. Figure 5.7 shows a schematic diagram of possible structures that could explain the obtained thickness and SLD of the lipid layer. A combination of a patchy layer and tilted or interpenetrating lipid tails, is a possible structure. Even if the coverage is not complete, the lipid bilayer is still connected as shown, by the FRAP measurements in chapter 3. Unfortunately, the present data could only resolve a uniform single layer model unable to unambiguously distinguish between a patchy layer, interpenetrating or tilted tails.

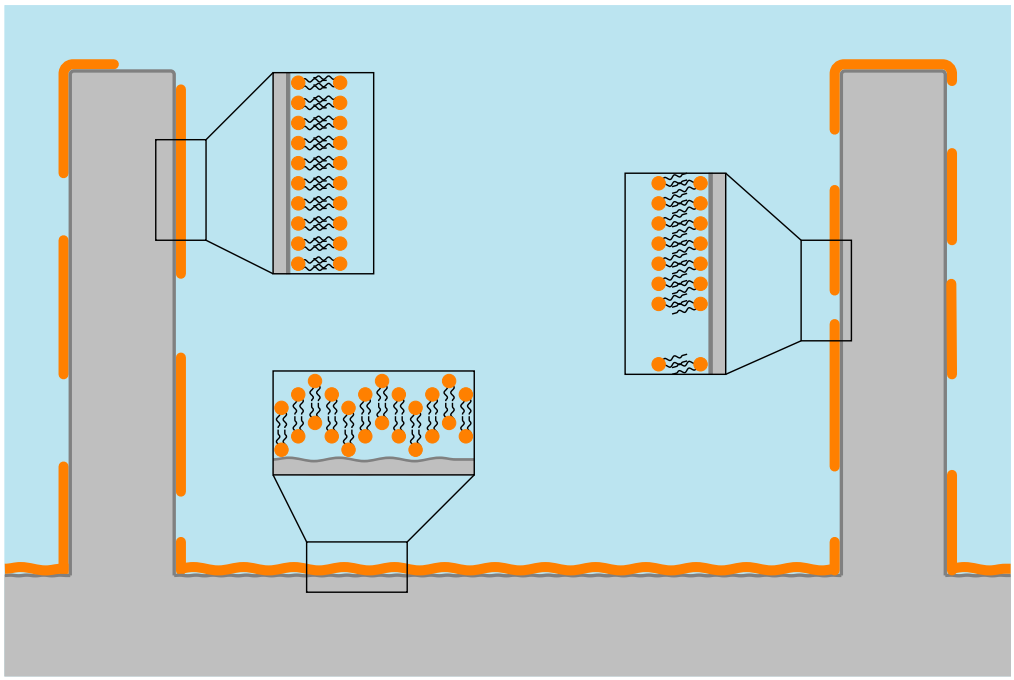

Figure 5.7: Schematic image showing possible structures for the lipid layer on the nanowires. The lipid layer could be divided in patches, which would explain the large solvent content of about 63 %. The lipid tails could be interpenetrating or tilted, which would lead to a thinner lipid layer.

5.3 Summary

This chapter has discussed a newly developed method for analyzing GISANS data from a regular array of hexagonal Si nanowires. The method is based on comparing ratios of scattered intensities for the lipid covered nanowires and bare nanowires with model calculated form factor ratios. This approach cancels effects of the structure factor, and simplifies the analysis to only investigate the change occurring when adding a lipid layer to the nanowires. The method was demonstrated for a sample consisting of a lipid mixture of 20 wt% DOPE in 80 wt% DOPC, on Si nanowires. The fitting of the model to the data gave a lipid layer with a thickness of 28.4 ± 4.2 Å with a large buffer content of about 63 vol%.

A great advantage of the method presented here is that it only considers the intensities in peaks. Other GISANS analysis techniques often use line cuts along rows of peaks and carry out model fits to the lines. These methods are usually focused on obtaining information from measurements on a single sample, whereas the method presented in this chapter directly models changes in the sample, such as the lipid layer on the nanowires. The difference in scattering that arises from changes at a surface can sometimes be rather weak, and it is therefore advantageous to focus the analysis on the relevant part of the data. Using the intensity ratio directly provides information on the lipid layer on the Si nanowires.

Chapter 6

Reflectometry on block copolymers

Block copolymer lithography uses self-assembly of block copolymers to produce high resolution, nanometer sized patterns over large areas. The block copolymers can self-assemble into many different structures, for example cylinders, lamella, or spheres, which are all of interest for the fabrication of semi-conductor devices. In block copolymer lithography one of the block components can be selectively infiltrated with an oxide to produce an etch mask for further processing [101,102]. In this work the polymers maltoheptaose and hydroxyl-terminated polystyrene were studied with neutron reflectometry to investigate the infiltration of AlO_x into the respective polymers. These polymers can be used to form the block copolymer polystyrene-block-maltoheptaose (PS-b-MH), which can form vertically or horizontally oriented cylinders with a distance between cylinders of $10 - 12\,\mathrm{nm}$ [103,104].

Figure 6.1 gives a schematic view of the block copolymer lithography process, where the top row shows the process for vertically aligned cylinders and the bottom row shows the same process for horizontally aligned cylinders. The process starts by letting the block copolymer self-assemble, fig. 6.1 a and d, on a Si substrate. Next, AlO_x is selectively infiltrated into the maltoheptaose block using a sequential infiltration synthesis (SIS, fig. 6.1 b, e), using the precursor gases trimethyl aluminum (TMA) and water. After SIS the PS-block is removed using reactive ion etching (RIE) (fig. 6.1 c, f), which leaves an etch mask on the Si substrate. The alumina etch mask is then used to transfer the pattern into the Si substrate (g) [102]. The amount of infiltrated AlO_x was characterized using neutron reflectometry at the SuperADAM instrument at the Institut Laue-

Langevin (ILL).

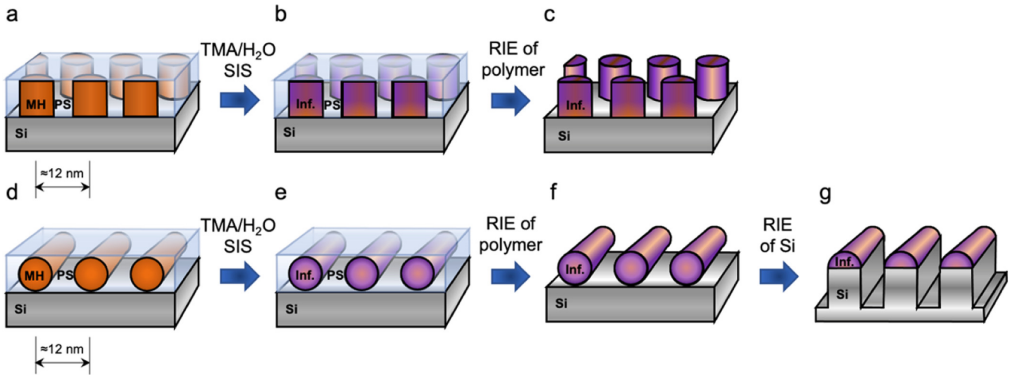

Figure 6.1: Schematic diagram of the block copolymer lithography process. The process starts (a, d) by letting the block copolymer self-assemble on a Si substrate. Next (b, e), the maltoheptaose is selectively infiltrated with AlO_x, in an SIS process using the precursor gases trimethyl aluminum (TMA) and water. The PS-block is removed (c, f) leaving a stable etch mask on the Si substrate. The etch mask (g) is then used to transfer the pattern into the Si substrate. Diagram from Löfstrand et al.[102].

6.1 Method

6.1.1 Homopolymer processing for reflectometry

For the reflectometry experiments, homopolymer samples of maltoheptaose and hydroxyl-terminated polystyrene were used, and the effect of the infiltration process was measured. The homopolymers were used in order to simplify the analysis.

The homopolymers were prepared by spin coating a 35 mm × 35 mm Si substrate of 1 mm thickness. Prior to the spin coating the Si wafers were pretreated on a hotplate at 200 °C for 10 min. The maltoheptaose samples were prepared by dissolving 1 wt% maltoheptaose (MH, 1.2 kg mol^{-1}, Hayashibara Co., Ltd., Japan) in a 3 : 1 volumetric ratio deionized (DI) water and isopropanol. The dissolved maltoheptaose was then spin coated to a thickness of 12 nm. For the other homopolymer samples, 1 wt% hydroxyl-terminated polystyrene (PS-OH, 4.5 kg mol^{-1}, PDI[1] 1.06, anionically polymerized by CERMAV) was dissolved in anisole and spin coated to a thickness of 17 nm. The thickness of all samples was

[1]The polydispersity index (PDI) is a measure of the distribution of the chain lengths of a polymer, i.e. PDI = 1 signifies that all chains are of the same length.

measured with spectroscopic ellipsometry (RC2, J.A. Wollam, Co., Inc., Lincoln, NE, USA). The samples were then baked on a hot plate for 3 min at 80 °C in order to remove residual solvents.

The spin coated homopolymer samples were exposed to the precursor gases using a SIS process. In SIS, the samples were exposed to precursor gases, in this case TMA and water, in a Savannah S100 (Cambridge NanoTech, Waltham, MA, USA) chamber at 80 °C under nitrogen flow at 20 standard cubic centimeters per minute (sccm) for a different number of cycles, where one cycle consisted of four steps. First, the precursor, TMA, was pumped through the chamber for a total of 100 s in 15 ms pulses. Second, the chamber was purged with N_2 for 90 s. Third, the second precursor, water, was pumped through the chamber for a total of 50 s in 10 ms pulses. The cycle ended by purging with N_2 for 600 s to remove byproducts and excess precursor. The maltoheptaose samples were exposed for 1, 2, 4, and 8 cycles, whereas the polystyrene sample was only exposed for 2 and 8 cycles.

6.1.2 Reflectometry at SuperADAM

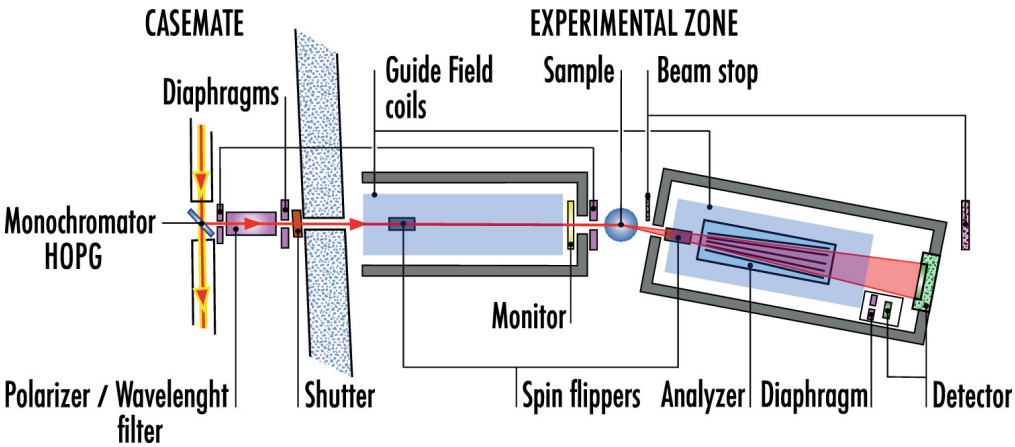

Figure 6.2: A schematic diagram of the SuperADAM instrument showing the different components of the instrument. Illustration from Devishvili et al.[105].

SuperADAM is a monochromatic reflectometry instrument located at the Institut Laue-Langevin (ILL) in Grenoble, France. SuperADAM is financed by the Swedish Research Council and operated by Uppsala University in collaboration with Lund and Linköping Universities. Figure 6.2 shows a schematic drawing of the SuperADAM instrument. The first part of the instrument is the monochromators, operating with a wavelength of 5.2 Å. These are one highly oriented

pyrolytic graphite (HOPG) monochromator and (not shown in the image) one graphite intercalation compound (GIC) monochromator. The HOPG monochromator is used for high resolution, with $\delta\lambda/\lambda = 0.005$, and the GIC, which is under development, is a lower resolution monochromator, with $\delta\lambda/\lambda = 0.035$. The GIC monochromator has an expected flux one order of magnitude higher than the HOPG monochromator[105,106].

The diaphragms, also known as slits, are used to limit the spatial size of the neutron beam and to remove neutrons that would not hit the sample, which would increase the background. There are three diaphragms before the sample position. The instrument also has the possibility to use polarized neutrons, and for that there are polarizers, spin flippers and analyzers. However, polarized neutrons were not used during this experiment and will not be discussed further. The sample is positioned on a high precision rotation stage, on top of which are two translation motors and one tilt motor which allow for alignment of the sample in the beam. The reflected neutron beam is detected by a ^{3}He single detector or by a wide area position sensitive detector, used for off-specular scattering, situated at a rotating detector arm. The incident angle is determined by the rotation stage under the sample and the outgoing angle is determined by the rotation of the detector and is adjusted to match the incident angle. The Q-range that can be obtained at SuperADAM is 0 to 2.5 Å^{-1}[105,106].

The homopolymers described in section 6.1.1 were used at SuperADAM to measure the depth of AlO_x infiltration as a function of the number of infiltration cycles. The measurements were performed on different samples which were infiltrated with a specific number of cycles. Reference measurements on the Si substrate and on pure atomic layer deposition (ALD) AlO_x were also performed. ALD and SIS are closely related processes, the difference being that with ALD material is deposited on a surface, whereas SIS deals with infiltration into materials[102]. Incidence angles from 0.12° to 4.0° were used, and together with a wavelength of 5.2 Å gave a Q-range of 0.005 Å^{-1} to 0.17 Å^{-1}. The raw data was reduced by subtracting the background, normalizing the reflected intensity to the intensity of the direct beam, and correcting for over-illumination of the sample. The reduced data was then fitted using the software *GenX*[107].

6.1.2.1 Scattering length density

The SLD was calculated from the known scattering length[85] and the densities of the materials.

Table 6.1: SLD of the components used in this experiment.
[1]Stated by the supplier.

Material	**SLD** $[10^{-6}\text{Å}^{-2}]$	**Density** $[\text{g cm}^{-3}]$
Si	2.07	2.33 [86]
SiO_2 (α-quartz)	4.18	2.65 [86]
Al_2O_3	5.70	3.97 [86]
MH ($C_{42}H_{72}O_{36}$)	2.12	1.85 [1]
PS $(C_8H_8)_n$	1.41	1.05 [86]
H_2O	-0.56	0.997 [86]

6.2 Results

The data and results presented here have been published by Löfstrand et al. [102] where I am one of the coauthors.

6.2.1 Infiltration into maltoheptaose

Figures 6.3 and 6.4 show the reflectometry and SLD profiles for the different samples of the pristine maltoheptaose and maltoheptaose after 1, 2, 4, and 8 SIS infiltration cycles. It can be seen that the fringes in the reflectometry data, fig. 6.3, move to lower Q, indicating that the layers were getting thicker with more infiltration cycles. The increase in thickness is also apparent in the SLD profiles, fig. 6.4. The results from the fits, which can be found in table 6.2, were compared with measurements with ellipsometry and SEM imaging in order to determine a realistic model. The results from ellipsometry and SEM can be found in Löfstrand et al. [102].

The pristine maltoheptaose, yellow in the figures, was fitted as one layer on top of the Si and SiO_2 substrate. The layer was fitted to 134.0 ± 2.9 Å with an SLD of $1.63 \pm 0.04 \times 10^{-6}$ Å^{-2}. The SLD for the pristine maltoheptaose was slightly lower than the theoretical value shown in table 6.1. The reason for this lower SLD could be inclusion of water, which would correspond to about 18%, or a lower density than tabulated values, at about $1.42\,\text{g cm}^{-3}$. Inclusion of 18% water in maltoheptaose is possible, however, this is at the higher range at normal humidity [108]. Most likely it was a combination of water inclusion and a lower density of the maltoheptaose.

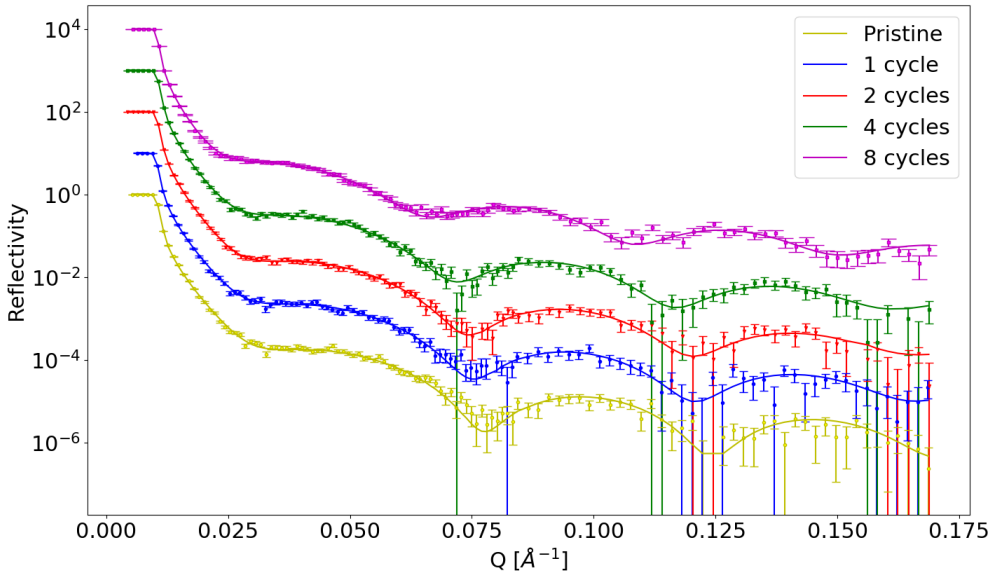

Figure 6.3: Reflectometry curves for pristine maltoheptaose, and for maltoheptaose infiltrated with AlO_x using 1, 2, 4, and 8 infiltration cycles. The data are shifted by factors of 10, 100, 10^3, and 10^4, for each data set.

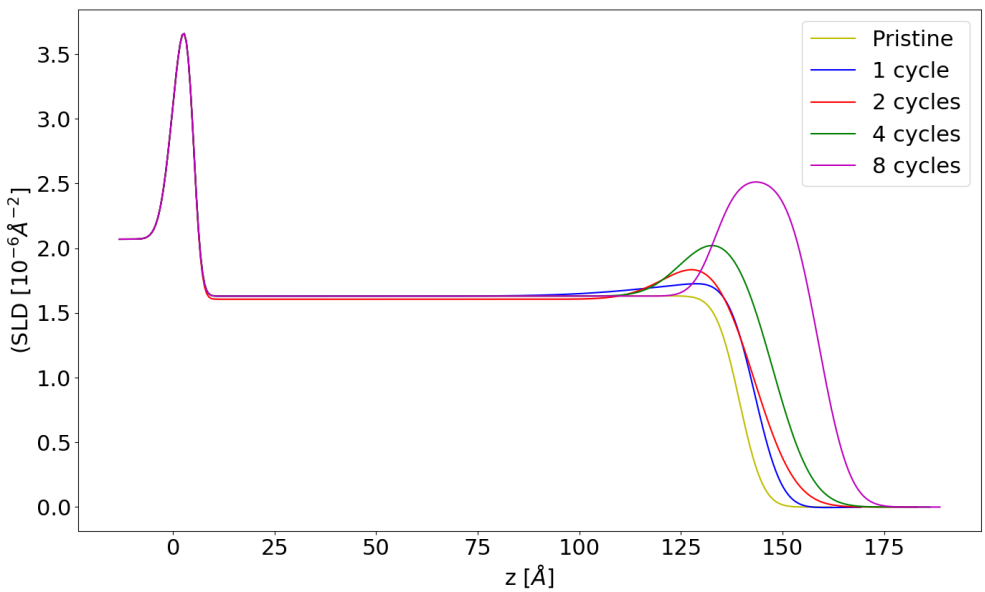

Figure 6.4: SLD profile of maltoheptaose infiltrated with AlO_x for varying number of cycles, where z is the distance from the substrate. The first peak shows the SiO_2 layer. The second peak shows the inclusion of AlO_x in the top layer of maltoheptaose.

Table 6.2: Results of the reflectometry fit to varying numbers of SIS cycles with TMA and water in maltoheptaose.

No. cycles	0	1	2	4	8
Top layer					
Thickness [Å]	—	20 ± 3	19 ± 3	22 ± 3	25 ± 3
SLD [10^{-6}Å^{-2}]	—	1.80 ± 0.12	2.05 ± 0.16	2.16 ± 0.17	2.54 ± 0.17
Roughness [Å]	—	5	8	8	8
vol% of ALD AlO_x	—	6	14	19	32
Bottom layer					
Thickness [Å]	134 ± 3	118	119	120	128
SLD [10^{-6}Å^{-2}]	1.63 ± 0.04	1.63	1.63	1.63	1.63
Roughness [Å]	5	19	9	7	5

Maltoheptaose was infiltrated using a SIS process, described in section 6.1.1, for 1, 2, 4, and 8 cycles. The infiltrated maltoheptaose film was fitted as two layers on top of the substrate, since a one layer model did not result in a good fit. The amount of included AlO_x increased for every infiltration cycle and a maximum of 32 vol% was included in the top layer after 8 infiltration cycles. The volume fraction, ϕ_1, of a component with SLD ρ_1, in this case AlO_x, in a mixture can be calculated through,

$$\phi_1 = \frac{\rho_{mix} - \rho_2}{\rho_1 - \rho_2} \tag{6.1}$$

where ρ_{mix}, and ρ_2 are the SLD of the mixture, and the other component, in this case MH, respectively (essentially the same equation as eq. (5.12)). The volume fraction was determined using the SLD for the pristine MH and the reference measurement on pure ALD AlO_x, which had an SLD of 4.49×10^{-6} Å^{-2}. The SLD of the reference measurement was lower than the theoretical value of 5.67×10^{-16} Å^{-2}, see table 6.1. The lower SLD was likely due to the ALD AlO_x often being very porous, leading to a decrease in density. The reference measurement on AlO_x was used since the deposition was carried out in the same way as for the AlO_x in the maltoheptaose films. The SLD of the pristine maltoheptaose was used since all the maltoheptaose films were deposited in the same way, prior to infiltration. The depth of infiltration increased from 20 Å with 1 SIS cycle to 25 Å for 8 SIS cycles. The increase in thickness and in SLD

can be quite clearly seen in fig. 6.4 which shows the SLD profile of the fitted layers.

6.2.2 Infiltration into polystyrene

It has previously been shown that TMA and water can diffuse through polystyrene, and that polystyrene is not expected to be infiltrated with AlO_x [109]. To investigate the diffusivity through polystyrene, hydroxyl-terminated polystyrene (PS-OH) was infiltrated using 2 and 8 cycles. The hydroxyl-terminated polystyrene includes one reaction site for TMA. Figure 6.5 shows the reflectivity for the pristine PS-OH and for the PS-OH infiltrated with 2 and 8 cycles. There was no apparent difference between the pristine PS-OH and PS-OH after 2 infiltration cycles, and this is even more clear in the SLD profile plot seen in fig. 6.6. After 8 infiltration cycles there was a slight shift in the peaks to lower Q indicating an increased thickness of the layer. The fit indicates an increase in layer thickness from 178 Å to 189 Å, fit parameters can be found in table 6.3. The SLD increased from 1.43×10^{-6} Å^{-2} to 1.46×10^{-6} Å^{-2}, however, the increase is within the measurement error. The slight increase in thickness and SLD could be due to the TMA reacting with the hydroxyl group in the polystyrene, which would lead to an initial AlO_x infiltration. The low infiltration rate in hydroxyl-terminated polystyrene would indicate that there is a high infiltration selectivity between polystyrene and maltoheptaose.

Table 6.3: Results of the reflectometry fits to varying number of SIS cycles with TMA and water in polystyrene.

No. cycles	0	2	8
Thickness [Å]	178 ± 3	178 ± 3	189 ± 3
SLD [10^{-6}Å^{-2}]	1.43 ± 0.03	1.43 ± 0.03	1.46 ± 0.04
Roughness [Å]	8	8	8
vol% of ALD AlO_x	0	0	1.1

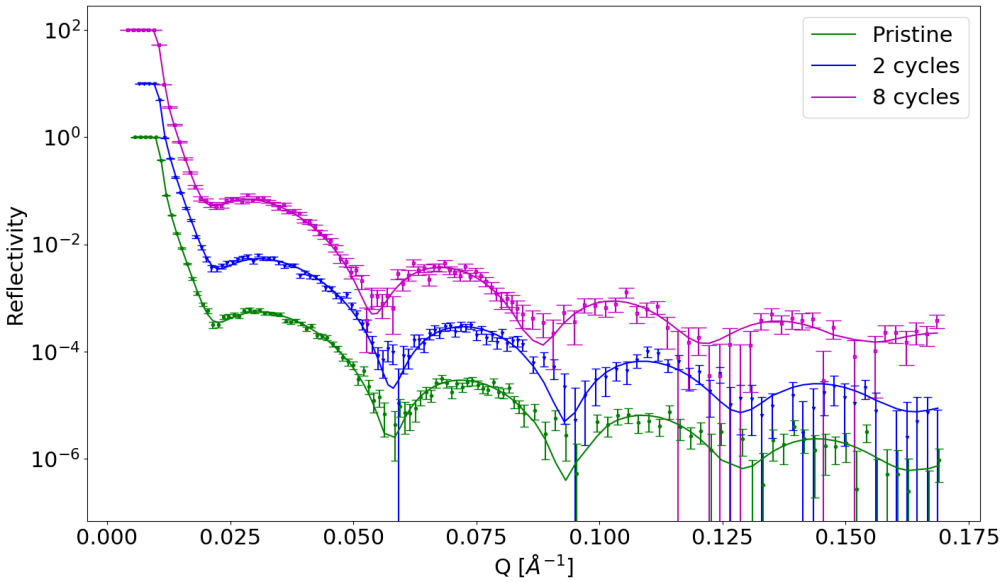

Figure 6.5: Reflectivity curves for pristine and infiltrated hydroxyl-terminated polystyrene. The curves show a small change in peaks to smaller Q for 8 infiltration cycles indicating a slight increase in layer thickness.

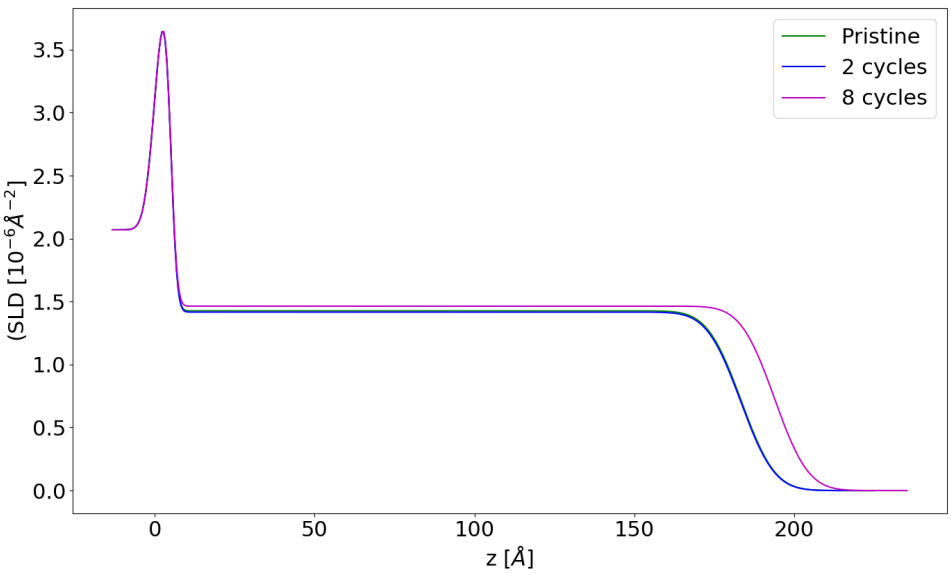

Figure 6.6: SLD profiles for pristine and infiltrated hydroxyl-terminated polystyrene, where z is the distance from the substrate.

6.3 Summary

This chapter has shown reflectometry data and results investigating the rate of infiltration of TMA and water into maltoheptaose and into hydroxyl-terminated polystyrene. The data and fits show that the amount of AlO_x increased with the number of SIS cycles, and that after 8 cycles approximately 32 vol% AlO_x had infiltrated in maltoheptaose. After 8 infiltration cycles in polystyrene only about 1.1 vol% AlO_x had infiltrated. This indicates that the infiltration selectivity between maltoheptaose and polystyrene was high.

Chapter 7

Reflectometry on a substrate with a nanowire array

Chapters 4 and 5, have described how the nanowire array was characterized with GISANS, giving information about lateral structures in thin films or at interfaces. Specular reflectometry, on the other hand, provides information about the average scattering length density profile perpendicular to the surface of the sample. Reflectometry and GISANS are, therefore, complementary to each other. This chapter provides a discussion of the results from neutron reflectometry measurements on the nanowire array substrate, with and without a lipid bilayer. These measurements were conducted as a complement to the GISANS measurements to obtain information on the surface between the nanowires. The reflectometry measurements were performed at the OffSpec beam line at the ISIS Neutron and Muon source. An exploratory study with spin-echo resolved grazing incidence scattering (SERGIS) was also carried out at OffSpec.

7.1 Method

7.1.1 OffSpec

OffSpec is a low background, polarized neutron reflectometer optimized for off-specular reflection located at the ISIS Neutron and Muon source, UK. The low background of the instrument is obtained by a bent neutron guide and shielding. OffSpec has two detectors, one linear, position sensitive scintillator detector placed 3.6 m from the sample position, and one single ^{3}He detector placed 3.2 m

from the sample. An incident wavelength band of 1.5 – 14.5 Å is available at the instrument. OffSpec has the capability of tracking neutrons using spin-echo and can be used to measure spin-echo small angle neutron scattering (SESANS) and spin-echo resolved grazing incidence scattering (SERGIS) [110,111].

7.1.2 Reflectometry

On OffSpec, the large square Si crystal with nanowires, described in chapter 2, was measured as a complement to the GISANS experiments. A wavelength range from 2.2 Å to 12.5 Å with incident beam angles of 0.7° and 2.0° was used, giving a Q-range of 0.01 $Å^{-1}$ to 0.2 $Å^{-1}$. From the reflectometry measurements, information was obtained mainly about the flat areas between the nanowires. The Si crystal was placed in an aluminum sample holder, described in chapter 4. Prior to being placed in the sample holder, the crystal was cleaned by placing the sample in a 1% solution of Neutracon (Decon Laboratories Ltd, Hove, East Sussex, UK) for about 20 min. The crystal was then carefully rinsed with and immersed in MilliQ water. Lastly, the crystal was rinsed once more with MilliQ water, then with 99.5% ethanol after which it was carefully dried with nitrogen.

The supported lipid bilayer was prepared according to chapter 3, however, a short description will follow. A lipid mixture of 20 wt% DOPE and 80 wt% DOPC was used, and the lipid bilayer was formed using vesicle fusion. The vesicle dispersion was prepared by mixing the appropriate amount of lipids, and dissolving them in chloroform. The chloroform was allowed to evaporate, leaving a lipid film, which was then rehydrated in phosphate buffered saline (PBS) and sonicated to form a lipid vesicle dispersion. This dispersion was then put in contact with the nanowires in the sample cell described in chapter 4, by flowing the vesicle dispersion through the cell, at a rate of 0.5 ml min^{-1}. The lipid vesicle dispersion was left to incubate in the cell for about 30 min, after which the cell was rinsed with PBS to remove remaining vesicles.

Measurements were first performed on the bare Si nanowire substrate in D_2O, H_2O, and in water that is contrast matched to Si (cmSi), which is a mixture of 38 vol% H_2O and 62 vol% D_2O. These measurements were performed in order to make a model of the bare substrate before adding the lipids. The lipids were then added to the substrate and the lipid bilayer on the nanowire array was again measured in D_2O, H_2O, and cmSi. The three solvents were used in order to give different contrasts between the lipid bilayer and the surrounding solvent.

7.1.3 Spin-echo resolved grazing incidence scattering

An exploratory study with spin-echo resolved grazing incidence scattering (SERGIS) was performed at OffSpec. SERGIS is a technique that uses the spin of the neutron to encode the angle that the neutron takes through the sample. Magnetic field regions are placed in front of and behind the sample, these have identical magnitudes but are oppositely oriented. A polarized neutron beam comes in through the first magnetic field, and the neutrons start to precess in a plane perpendicular to the magnetic field. The neutrons then go through the sample and, if no interactions with the sample occur, the neutrons leaving the second magnetic field will have the same polarization as they started with. If, however, the neutrons interact with and scattered from the sample, then the initial polarization will not be restored following the second magnetic field, and a change in beam polarization is seen [112].

Ashkar et al. [113] presented a method for investigating spherical colloid particles in a diffraction grating by means of spin-echo SANS (SESANS). The idea was to use the nanowire array in a similar way and potentially resolve lipids and proteins attached to the nanowires, but using SERGIS. Measurements on the Si nanowire array were conducted in D_2O.

7.1.4 Analysis

The reflectometry data from OffSpec were analyzed with the software *refnx* [5]. This software is written in Python and is based on refining a model against a data set. The model reflectivity is calculated using the Abelès method [114]. The model reflectivity is calculated on a so-called `Structure` consisting of different `Component` objects. These objects represent the physical parameters of the sample, for example the thickness or SLD. The simplest of these objects is a so-called `Slab`. A slab has a uniform thickness, SLD, roughness and volume fraction of the solvent. Another type of object is the `LipidLeaflet` object, which is a lipid monolayer, consisting of a head and a tail region, both with their own SLD and thickness. Roughness may exist at the interface between two slabs, or between the head and tail region in a lipid leaflet. Within the `Structure` there is also a substrate and a solvent [97].

With *refnx* it is possible to refine multiple data sets together. This is often done when data sets are measured in different solvent contrasts. When refining data sets together it is possible to obtain a more reliable fit, since the extra contrast can help resolve ambiguity that arises from the loss of phase information when measuring the intensity between different layers.

7.2 Results

7.2.1 SERGIS

An exploratory study with SERGIS was performed on the nanowire array. Unfortunately, problems with the instrument prevented any proper measurement and analysis of the data. Five measurements were performed on the same sample, which was the nanowire array in D_2O. Unfortunately it turned to be challenging to reproduce the data. This prevented further analyzes and further measurements were therefore not continued.

7.2.2 Reflectometry

The reflectometry data were analyzed by co-refining three data sets measured in D_2O, H_2O, and cmSi. First, the data for the bare nanowire substrate were analyzed in order to model fit the substrate before the addition of the lipid bilayer. The data and fits to the bare nanowire substrate can be seen in fig. 7.1. The substrate was modeled as silicon with three layers on top. The first layer consisted of a mixture of Si and SiO_2 and was 60.0 ± 1.4 Å thick with a solvent volume fraction of 0.160 ± 0.004. The next layer was 17.0 ± 0.8 Å thick with 42 % solvent and consisted of SiO_2. The layers closest to the substrate were modeled as two layers since that resulted in a better fit as opposed to a single layer model. These layers also had quite significant roughness, 25 Å and 10 Å, respectively. The structure of the layers, porous, and a mix of Si and SiO_2, are thought to come from the etching that was used to produce the nanowires. The last layer represents the nanowires and was modeled as a thick silicon layer with a large solvent content. The thickness of that layer was the same as the length of the nanowires, determined from electron microscopy. The solvent content was kept at 97.4% since the nanowires only covered 2.6% of the substrate surface, based on the SEM images in fig. 2.7. Table 7.1 lists all the parameters used for the fit to the bare nanowire substrate, and these parameters were also utilized for the rest of the model fits for the lipid layer.

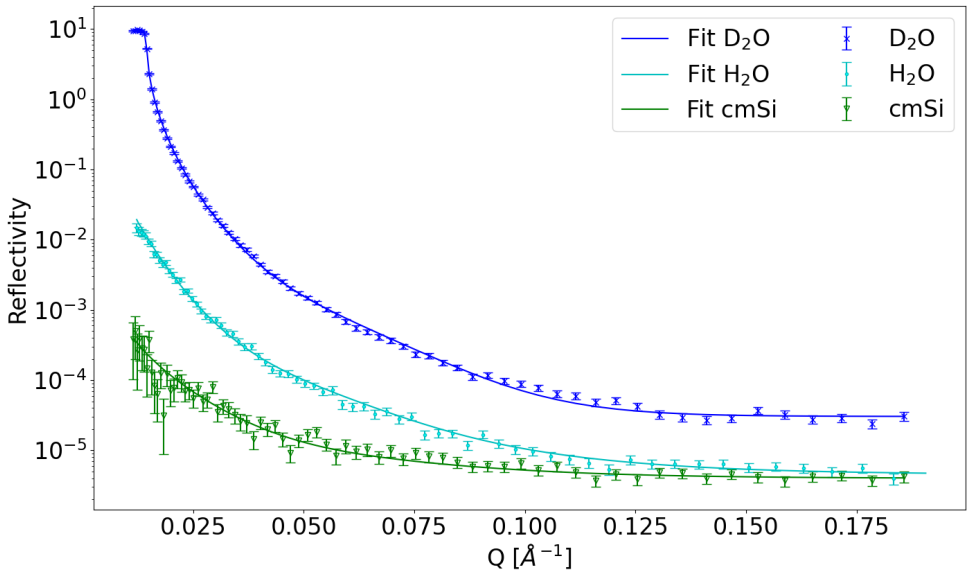

Figure 7.1: Data and model fit for the bare nanowire substrate in D_2O, H_2O, and in cmSi. The data and fit for the D_2O are shifted by a factor of 10, for clarity.

Table 7.1: Fitted parameters for the structural model of the bare nanowire substrate. The roughness parameter is written between the lines in the table indicating the interface for which the roughness is applied. Layer thickness, t_{layer}, Volume fraction solvent, ϕ_{solv}

	$\mathbf{t}_{layer}$ [Å]	ϕ_{solv}	**Rough** [Å]
Substrate	semi inf.	0	25
Si + SiO_2 + Solvent	60 ± 1.4	0.16 ± 0.004	10
SiO_2 + Solvent	17 ± 0.8	0.42 ± 0.03	5
Nanowire	7600	0.974	3
Solvent	semi inf.	1	

After analyzing the data for the bare nanowires substrate, a lipid layer was added to the model. The lipid layer was modeled in two ways, using a single uniform layer or slab, and as a structured bilayer with two lipid leaflets. The lipid layer was first modeled as a slab, since this model is simpler, but also to be able to more easily compare the results from the fit with the GISANS fit in chapter 5. The lipid slab in this model was placed after the first two layers from the bare nanowire substrate model. Figure 7.2 shows the data and model for

the lipid layer fitted as a homogeneous slab. The SLD of the slab was fixed at $0.36 \times 10^{-6}\,\text{Å}^{-2}$, which is the theoretical SLD of the lipid layer (see table 4.1 in chapter 4) with 2.6% Si, representing the nanowires going through the lipid layer. The thickness of the lipid layer was fitted to be $36.9 \pm 0.2\,\text{Å}$ with a volume fraction of solvent of 0.245 ± 0.002. The area per molecule, A_m was calculated using the thickness of the layer, t, the volume of the lipid molecule, V_M (see table 4.1 in chapter 4) and the volume fraction of lipid, ϕ_{lipid},

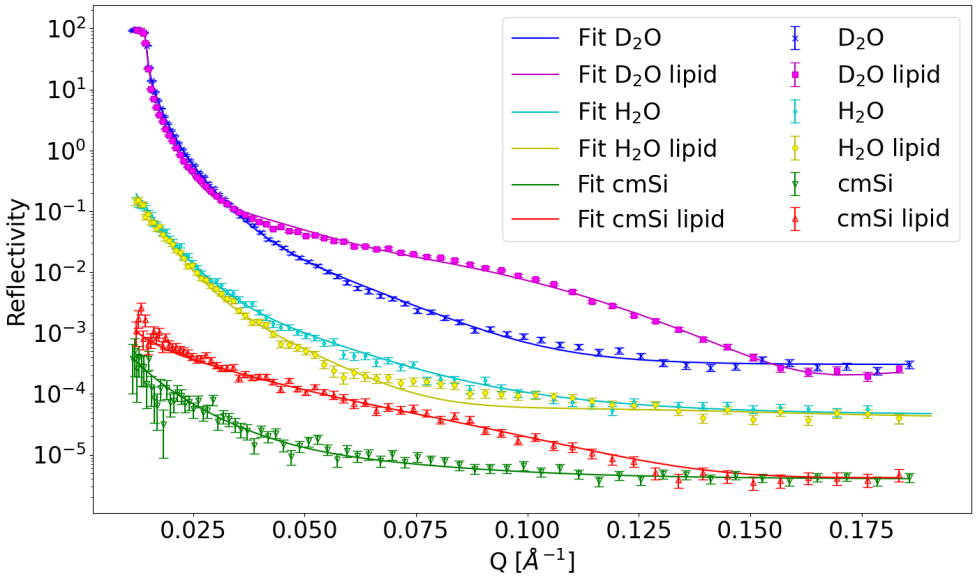

Figure 7.2: Data and model fit for the lipid layer in D_2O, H_2O, and cmSi using the slab model. The H_2O and D_2O data are shifted by factors of 10 and 100, respectively.

$$A_m = \frac{2\,V_M}{\phi_{lipid}\,t} \tag{7.1}$$

where the volume of the lipid molecule was multiplied by 2 since a bilayer was assumed. The area per molecule was calculated to $91.9 \pm 0.3\,\text{Å}^2$.

The lipid layer was then modeled using two lipid leaflets. In this model, the head and tail groups have individual thicknesses, scattering lengths and lipid volumes. The lipid leaflets also have the additional parameter of area per molecule, which models the density of the lipid bilayer. The two lipid leaflets were placed on top the first two layers from the bare nanowire substrate model, in the same way as for the slab model. The scattering length of the head and tails was compensated

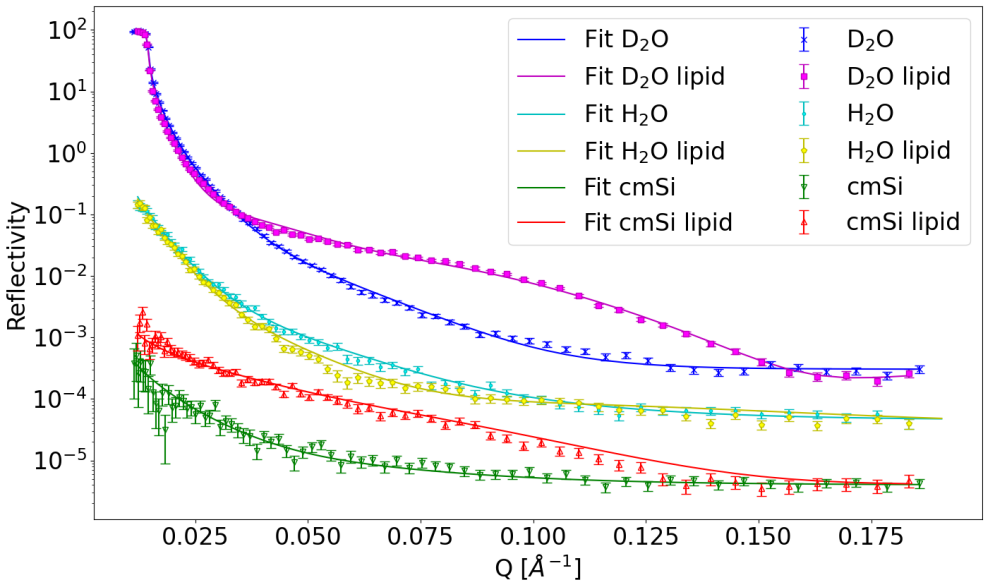

Figure 7.3: Data and model fit for the lipid layer in D_2O, H_2O, and cmSi using the lipid leaflet model. The H_2O and D_2O data are shifted by factors of 10 and 100, respectively.

for the Si nanowires going through the layer, in a similar way to the slab model. Figure 7.3 shows the data and model fit using a lipid leaflet model. The fitting parameters can be found in table 7.2. The total thickness of the lipid bilayer was 37.3 ± 1.6 Å. The volume fraction of solvent in the lipid layer was calculated by first calculating the SLD, ρ_x, of the lipid, solvent mixed layer,

$$\rho_x = \phi_x \frac{b_x}{V_x} + (1 - \phi_x)\rho_{x,solv}, \tag{7.2}$$

where the subscript x indicates the lipid head and tail, respectively. V_x is the volume, b_x is the scattering length, $\rho_{x,solv}$ is the SLD of the solvent surrounding the lipid, and ϕ_x is the volume fraction of lipid, which is defined by,

$$\phi_x = \frac{V_x}{A_m t_x} \tag{7.3}$$

where A_m is the area per molecule and t_x is the thickness. The volume fraction of solvent, ϕ_{solv}, was calculated in the same way as in previous chapters, by using,

$$\phi_{solv} = \frac{\rho_x - \rho_{lipid}}{\rho_{solv} - \rho_{lipid}} \tag{7.4}$$

where ρ_{solv} and ρ_{lipid} are the SLD of the pure solvent and pure lipid, respectively. According to the model fit, the volume fraction of solvent was lower in the head region than in the tail region.

Table 7.2: Fitting parameters for the lipid layer on the nanowire substrate using the two different models. Layer thickness, t_{layer}, Area per molecule, A_m, Volume fraction solvent, ϕ_{solv}

Slab model	$\mathbf{t}_{layer}$ [Å]	$\mathbf{A}_m$ [Å^2]	ϕ_{solv}	**Rough** [Å]
Bare substrate	parameters in	table 7.1		3
Lipid slab	36.9 ± 0.2	91.9 ± 0.3	0.245 ± 0.002	5
Layer NW	7600	——	0.974	3
Solvent	semi inf.	——	1	
Lipid leaflet model				
Bare substrate	parameters in	table 7.1		3
Lipid head inner	3.4 ± 0.4	91.9 ± 0.4	0.01	3
Lipid tails inner	16.4 ± 0.7	91.9 ± 0.4	0.35	3
Lipid tails outer	14.2 ± 1.0	91.9 ± 0.4	0.25	7
Lipid head outer	3.3 ± 0.9	91.9 ± 0.4	0.007	5
Layer NW	7600	——	0.974	3
Solvent	semi inf.	——	1	

When comparing the model fits for the slab, fig. 7.2, and for the lipid leaflet, fig. 7.3, it was fairly difficult to tell them apart. The results from both fits also gave approximately the same total thickness of the lipid layer, with 36.9 ± 0.2 Å for the slab model and 37.3 ± 1.6 Å for the lipid leaflet model. The thickness of the lipid bilayer obtained from both model fits corresponded well with previous studies on bilayers[115]. Table 7.3 shows all the obtained χ^2 values, which were about the same for both models. With this data it was not possible to distinguish between the two models. In order to get a better fit to the lipid bilayer more contrasts could be used, to selectively mask either the tail or head regions.

Table 7.3: The goodness of fit, χ^2, for the two models.

	D_2O	cmSi	H_2O
Slab model	1092	124	218
Lipid leaflet	1082	139	145

Selectively deuterating one of the lipids or part of a lipid would also change the contrast, giving more data sets to constrain the model.

7.3 Summary

This chapter has shown reflectometry data and model fits for the nanowire substrate with and without a lipid bilayer. The model fits indicated that the Si substrate had a rough, porous top layer and this structure was most likely due to the etching used to produce the nanowires. The lipid layer on top of the Si substrate was modeled in two different ways, with a slab model and with a lipid leaflet model. The two models were shown to fit the data equally well. The lipid bilayer was approximately 37.0 ± 1.5 Å thick, with about 30% solvent in the layer.

Chapter 8

Conclusions

My PhD project has been focused on neutron scattering, where I have used grazing incidence small angle neutron scattering (GISANS) and reflectometry to study a lipid bilayer on Si nanowires. Both GISANS and reflectometry are powerful techniques that are complementary to one another. Therefore, the possibility of performing both experiments simultaneously, or in close proximity, is a major advantage. With GISANS it was possible to determine the thickness and coverage of the lipid bilayer on the nanowires. With reflectometry, on the other hand, I could determine the structure of the bilayer on the flat areas between the nanowires. However, neutron scattering experiments are always dependent on external research facilities, and require long measurement times. This means that these experiments can not be performed that frequently, and it can be difficult to repeat experiments. To analyze the GISANS data, a new method had to be developed, since current methods were not suitable for the sample with an array of nanowires.

8.1 Newly developed GISANS analysis method

The GISANS data were analyzed using a newly developed method based on ratios of form factors, described in chapter 5. The procedure consisted of comparing ratios of the scattered intensity for the lipid covered nanowires and the bare nanowires with model calculations. Using ratios of integrated scattered intensity cancels the effects of the structure factor, which is assumed to be the same before and after the addition of lipid. This simplifies the analysis, and allows

information to be obtained directly on the change when adding the lipid, which is one of the major strengths of this method.

In the analysis, the measured intensity arising from scattering perpendicular to the nanowires was used, as can be seen in fig. 5.3. The intensity was mainly due to the radial structure of the nanowires. These peaks were used since they were expected to show the largest changes with addition of the lipid. This significant effect is because the lipid layer was about one order of magnitude smaller than the radius of the nanowires, whereas the length of the nanowires was approximately two orders of magnitude larger than the lipid layer.

Another reason to use the peaks perpendicular to the nanowires was to avoid issues of refraction. The intensity arising from scattering parallel to the nanowires is mainly due to the length of the nanowires, which are about 7500 Å long. Due to this length, there can occur a difference in optical path length of the neutron beam, which can lead to phase differences of the neutron beam scattered in this direction. Such a phase difference would then modify the scattering pattern, and this modification would have to be taken into account when using the ratio calculations. This is the major reason why the scattering in the direction parallel to the length of the nanowires has not yet been used, even though the peaks were of much higher intensity in that direction.

8.2 Nanowire supported lipid bilayer

A supported lipid bilayer, consisting of a mixture of 20 wt% DOPE and 80 wt% DOPC, was studied with four techniques, quartz crystal microbalance with dissipation (QCM-D), confocal microscopy with fluorescently labeled lipids, neutron reflectometry and GISANS. All methods have their advantages and disadvantages, and can give complementary information about the lipid bilayer.

QCM-D measures the bound mass on a quartz crystal, by monitoring changes in the resonance frequency[15,73,74]. The technique gives a measure of the total bound mass on the surface, which, in the case of a lipid bilayer, can include water bound to the lipids. Using QCM-D it is possible to monitor the formation of the lipid bilayer as well as calculate the area per molecule of the formed bilayer. However, QCM-D only makes it possible to follow the formation of the bilayer on a flat surface.

Confocal microscopy on fluorescently labeled lipids allows imaging of the lipid bilayer formed on the nanowire surface. Using confocal microscopy it is possible to create 3D reconstructions of the lipid bilayer on the nanowires, and with that

image the full length of the nanowire. It is also possible to measure fluorescence recovery after photobleaching (FRAP). FRAP works by bleaching a small spot on the bilayer and then monitoring and measuring the time it takes for the fluorescent signal to recover[67–69]. FRAP revealed that the lipid bilayer was fluid, connected and mobile on the nanowires. Unfortunately, confocal microscopy cannot reveal the structure, thickness and coverage of the lipid bilayer.

With GISANS and reflectometry it was possible to determine the thickness and coverage of the lipid bilayer on and between the nanowires. However, neutron scattering experiments are always dependent on external research facilities, and require long measurement times. This means that these experiments can not be performed frequently, and that it can be difficult to repeat experiments. To analyze the GISANS data a new method had to be developed, since current methods were not suitable to use for the sample with an array of nanowires. With reflectometry, information was obtained primarily on the flat areas between the nanowires, and the results could therefore be compared with QCM-D, however, on slightly different flat surfaces. With GISANS, on the other hand, information was obtained on the nanowires, and on the curved lipid bilayer.

A parameter that can be obtained from both QCM-D and reflectometry is the area per molecule for a supported lipid bilayer. The area per molecule is calculated from the adsorbed mass on the QCM-D crystal, and was calculated to be $50\,\text{Å}^2$. From reflectometry the area per molecule can either be a fitting parameter, if a lipid leaflet model is used, or can be calculated from the thickness, lipid fraction and the volume of the lipid, if a slab model is used. Both models gave an area per molecule of $92\,\text{Å}^2$, which was slightly larger than that found for pure DOPC bilayers[78]. The results from QCM-D and reflectometry differed rather significantly. As noted, the mass in QCM-D also included water bound to the lipid bilayer. The reflectometry measurements gave a solvent fraction in the lipid bilayer of about 30 %. Using this would give an area per molecule of about $70\,\text{Å}^2$. The remaining difference in the area per molecule on the QCM-D crystal and on the Si surface used during reflectometry, could be due to a difference in surface roughness. The QCM-D crystal had a low roughness[1], whereas the flat areas between the nanowires have a higher degree of roughness, due to the etching process used to fabricate the nanowires. The high roughness of the Si substrate could lead to unfavorable packing of the lipids which would result in a larger area per molecule.

From the GISANS measurements, the thickness of the lipid layer on the surface of the nanowires was determined to be about 30 Å with a solvent fraction of

[1]Less than 10 Å root mean squared roughness, according to the manufacturer (Biolin Scientific, Gothenburg, Sweden).

about 60 %. This was about double compared with the results obtained from the reflectometry measurements on the flat areas. The high solvent fraction was likely due to the lipid bilayer forming a patchy bilayer. However, the lipid layer still seemed to be connected, shown by the mobility of the lipids from the FRAP measurements. Due to the large amount of solvent in the layer it is not really useful to calculate an area per molecule, and so a direct comparison to the QCM-D and reflectometry data was not possible. However, the measured thickness obtained by GISANS and reflectometry were comparable.

8.2.1 Protein interactions

Two different proteins were added to the supported lipid bilayer to investigate the binding of the proteins to the curved lipid surfaces. The proteins used were α-synuclein and streptavidin. Streptavidin has been shown to bind to a supported lipid bilayer on nanowires[49]. α-synuclein has been seen to have a higher binding affinity to curved bilayers than to flat bilayers[64]. The proteins were added to the formed supported lipid bilayer and measured with GISANS.

When adding the protein to the lipid layer only small changes in the scattering pattern were observed for either of the two proteins. With the α-synuclein protein, both a hydrogenated and deuterated version were used. However, there was no noticeable difference after the addition of either of the samples. The concentration of protein might have been too low for a noticeable change in the contrast between the already formed lipid bilayer and the protein, given the small difference in scattering length density. A quantitative analysis of the protein binding turned out to be rather challenging and required additional beam time, which was not available.

8.3 Outlook

Prior to the pandemic I had further planned neutron beam time, both for GISANS and for reflectometry. The intention for the GISANS experiments was to repeat the measurements on the nanowires with the lipid bilayer, in order to gain more data to verify the developed method. Longer measurement times would most likely be required to increase the intensity in the peaks perpendicular to the nanowires. Measurements on the proteins were also planned to be repeated, since the measurements made so far were inconclusive.

In order to test the method further, it would be interesting to use other types of arrays of nanostructures. Since the method is based on ratios of form factor, in theory, any shape that has a defined form factor could be used. That could for example be spheres, cones, or cubes. If structures that are much shorter than the nanowires are used, then it might be less challenging to use the peaks arising from scattering parallel to the structure. In the GISANS data presented in chapters 4 and 5, the peaks in the horizontal direction, arising from scattering parallel to the long axis of the nanowires, were much more intense than the peaks in the vertical direction. However, with shorter structures, a finer tuning of the mean penetration depth would be needed. This would be facilitated with higher resolution instrumentation that still has high incident neutron flux.

The results from the GISANS analysis suggested that the lipid layer had formed in patches. So far, the lipid mixture that was used consisted of 20 wt% DOPE and 80 wt% DOPC. Using other lipid mixtures might lead to a larger degree of coverage of the nanowires. Investigating the binding of proteins to other lipid mixtures would also be of interest.

References

[1] B. T. M. Willis and C. J. Carlile. *Experimental Neutron Scattering*. Oxford University Press, 2017.

[2] SasView, . URL `https://www.sasview.org/`. Accessed: 2021-08-05.

[3] SasView. Sphere function, . URL `https://www.sasview.org/docs/user/models/sphere.html`. Accessed: 2021-08-11.

[4] A. Guinier, G. Fournet, and K. L. Yudowitch. *Small-angle scattering of X-rays*. John Wiley & Sons, Inc. New York, 1955.

[5] A. R. J. Nelson and S. W. Prescott. refnx: neutron and x-ray reflectometry analysis in Python. *Journal of Applied Crystallography*, 52(1):193–200, 2019.

[6] P. Müller-Buschbaum. Grazing incidence small-angle neutron scattering: challenges and possibilities. *Polymer Journal*, 45(1):34–42, 2013.

[7] P. Müller-Buschbaum, E. Metwalli, J.-F. Moulin, V. Kudryashov, M. Haese-Seiller, and R. Kampmann. Time of flight grazing incidence small angle neutron scattering. *The European Physical Journal Special Topics*, 167(1):107–112, 2009.

[8] Y. Xia, P. Yang, Y. Sun, Y. Wu, B. Mayers, B. Gates, Y. Yin, F. Kim, and H. Yan. One-dimensional nanostructures: synthesis, characterization, and applications. *Advanced Materials*, 15(5):353–389, 2003.

[9] K. Hiruma, H. Murakoshi, M. Yazawa, and T. Katsuyama. Self-organized growth of GaAsInAs heterostructure nanocylinders by organometallic vapor phase epitaxy. *Journal of Crystal Growth*, 163(3):226–231, 1996.

[10] C. Thelander, P. Agarwal, S. Brongersma, J. Eymery, L.-F. Feiner, A. Forchel, M. Scheffler, W. Riess, B. J. Ohlsson, U. Gösele, and L. Samuel-

son. Nanowire-based one-dimensional electronics. *Materials Today*, 9(10): 28–35, 2006.

[11] Y. Wu and P. Yang. Direct observation of vapor- liquid- solid nanowire growth. *Journal of the American Chemical Society*, 123(13):3165–3166, 2001.

[12] H. Jansen, M. de Boer, R. Legtenberg, and M. Elwenspoek. The black silicon method: a universal method for determining the parameter setting of a fluorine-based reactive ion etcher in deep silicon trench etching with profile control. *Journal of Micromechanics and Microengineering*, 5(2): 115–120, 1995.

[13] M. M. Mirza, H. Zhou, P. Velha, X. Li, K. E. Docherty, A. Samarelli, G. Ternent, and D. J. Paul. Nanofabrication of high aspect ratio (50: 1) sub-10 nm silicon nanowires using inductively coupled plasma etching. *Journal of Vacuum Science & Technology B, Nanotechnology and Microelectronics: Materials, Processing, Measurement, and Phenomena*, 30(6): 06FF02, 2012.

[14] E. Lind. High frequency III–V nanowire MOSFETs. *Semiconductor Science and Technology*, 31(9):093005, 2016.

[15] R. Röder and C. Ronning. Review on the dynamics of semiconductor nanowire lasers. *Semiconductor Science and Technology*, 33(3):033001, 2018.

[16] P. Espinet-Gonzalez, E. Barrigón, Y. Chen, G. Otnes, G. Vescovi, C. Mann, J. V. Lloyd, D. Walker, M. D. Kelzenberg, I. Åberg, M. Borgström, L. Samuelson, and H. A. Atwater. Nanowire solar cells: a new radiation hard PV technology for space applications. *IEEE Journal of Photovoltaics*, 10(2):502–507, 2020.

[17] I. Åberg, G. Vescovi, D. Asoli, U. Naseem, J. P. Gilboy, C. Sundvall, A. Dahlgren, K. E. Svensson, N. Anttu, M. T. Björk, and L. Samuelson. A GaAs nanowire array solar cell with 15.3% efficiency at 1 sun. *IEEE Journal of Photovoltaics*, 6(1):185–190, 2015.

[18] C. N. Prinz. Interactions between semiconductor nanowires and living cells. *Journal of Physics: Condensed Matter*, 27(23):233103, 2015.

[19] C. Prinz, W. Hällström, T. Mårtensson, L. Samuelson, L. Montelius, and M. Kanje. Axonal guidance on patterned free-standing nanowire surfaces. *Nanotechnology*, 19(34):345101, 2008.

[20] W. Hällström, C. N. Prinz, D. Suyatin, L. Samuelson, L. Montelius, and M. Kanje. Rectifying and sorting of regenerating axons by free-standing nanowire patterns: a highway for nerve fibers. *Langmuir*, 25(8):4343–4346, 2009.

[21] F. Johansson, M. Jonsson, K. Alm, and M. Kanje. Cell guidance by magnetic nanowires. *Experimental Cell Research*, 316(5):688–694, 2010.

[22] M. Lard, H. Linke, and C. N. Prinz. Biosensing using arrays of vertical semiconductor nanowires: mechanosensing and biomarker detection. *Nanotechnology*, 30(21):214003, 2019.

[23] Y. Wang, T. Wang, P. Da, M. Xu, H. Wu, and G. Zheng. Silicon nanowires for biosensing, energy storage, and conversion. *Advanced Materials*, 25(37): 5177–5195, 2013.

[24] D. Verardo, F. W. Lindberg, N. Anttu, C. S. Niman, M. Lard, A. P. Dabkowska, T. Nylander, A. Månsson, C. N. Prinz, and H. Linke. Nanowires for biosensing: lightguiding of fluorescence as a function of diameter and wavelength. *Nano Letters*, 18(8):4796–4802, 2018.

[25] W. Hällström, M. Lexholm, D. B. Suyatin, G. Hammarin, D. Hessman, L. Samuelson, L. Montelius, M. Kanje, and C. N. Prinz. Fifteen-piconewton force detection from neural growth cones using nanowire arrays. *Nano Letters*, 10(3):782–787, 2010.

[26] Z. Li, H. Persson, K. Adolfsson, L. Abariute, M. T. Borgström, D. Hessman, K. Åström, S. Oredsson, and C. N. Prinz. Cellular traction forces: a useful parameter in cancer research. *Nanoscale*, 9(48):19039–19044, 2017.

[27] H. Persson, C. Købler, K. Mølhave, L. Samuelson, J. O. Tegenfeldt, S. Oredsson, and C. N. Prinz. Fibroblasts cultured on nanowires exhibit low motility, impaired cell division, and DNA damage. *Small*, 9(23):4006–4016, 2013.

[28] G. Piret, M.-T. Perez, and C. N. Prinz. Support of neuronal growth over glial growth and guidance of optic nerve axons by vertical nanowire arrays. *ACS Applied Materials & Interfaces*, 7(34):18944–18948, 2015.

[29] R. Wierzbicki, C. Købler, M. R. B. Jensen, J. Łopacińska, M. S. Schmidt, M. Skolimowski, F. Abeille, K. Qvortrup, and K. Mølhave. Mapping the complex morphology of cell interactions with nanowire substrates using FIB-SEM. *PloS One*, 8(1):e53307, 2013.

[30] H.-Y. Lou, W. Zhao, Y. Zeng, and B. Cui. The role of membrane curvature in nanoscale topography-induced intracellular signaling. *Accounts of Chemical Research*, 51(5):1046–1053, 2018.

[31] J. M. Berg, J. L. Tymoczko, L. Stryer, and G. J. Gatto, Jr. *Biochemistry*. W. H. Freeman and Company, 7th edition, 2012.

[32] Avanti Polar Lipids. 3D structure, DOPC. URL `https://avantilipids.com/product/850375`. Accessed: 2021-08-10.

[33] H. T. McMahon and J. L. Gallop. Membrane curvature and mechanisms of dynamic cell membrane remodelling. *Nature*, 438(7068):590–596, 2005.

[34] T. Splettstoesser. Synapse schematic. Wikimedia Commons. Available at: `https://en.wikipedia.org/wiki/Synapse#/media/File:SynapseSchematic_lines.svg`, accessed August 4, 2021.

[35] W. Helfrich. Elastic properties of lipid bilayers: theory and possible experiments. *Zeitschrift für Naturforschung C*, 28(11-12):693–703, 1973.

[36] D. Marsh. Intrinsic curvature in normal and inverted lipid structures and in membranes. *Biophysical Journal*, 70(5):2248–2255, 1996.

[37] J. N. Israelachvili. *Intermolecular and Surface Forces*. Academic Press, 2nd edition, 1992.

[38] O. G. Mouritsen. Lipids, curvature, and nano-medicine. *European Journal of Lipid Science and Technology*, 113(10):1174–1187, 2011.

[39] S. M. Gruner. Intrinsic curvature hypothesis for biomembrane lipid composition: a role for nonbilayer lipids. *Proceedings of the National Academy of Sciences*, 82(11):3665–3669, 1985.

[40] E. Sackmann. Supported membranes: scientific and practical applications. *Science*, 271(5245):43–48, 1996.

[41] M. L. Wagner and L. K. Tamm. Tethered polymer-supported planar lipid bilayers for reconstitution of integral membrane proteins: silane-polyethyleneglycol-lipid as a cushion and covalent linker. *Biophysical Journal*, 79(3):1400–1414, 2000.

[42] E. T. Castellana and P. S. Cremer. Solid supported lipid bilayers: From biophysical studies to sensor design. *Surface Science Reports*, 61(10):429–444, 2006.

[43] J. Liu and J. C. Conboy. Structure of a gel phase lipid bilayer prepared by the Langmuir-Blodgett/Langmuir-Schaefer method characterized by sum-frequency vibrational spectroscopy. *Langmuir*, 21(20):9091–9097, 2005.

[44] J. Kurniawan, J. F. Ventrici de Souza, A. T. Dang, G.-y. Liu, and T. L. Kuhl. Preparation and characterization of solid-supported lipid bilayers formed by Langmuir–Blodgett deposition: a tutorial. *Langmuir*, 34(51): 15622–15639, 2018.

[45] E. Reimhult, F. Höök, and B. Kasemo. Intact vesicle adsorption and supported biomembrane formation from vesicles in solution: influence of surface chemistry, vesicle size, temperature, and osmotic pressure. *Langmuir*, 19(5):1681–1691, 2003.

[46] S. Ahmed, Z. Nikolov, and S. L. Wunder. Effect of curvature on nanoparticle supported lipid bilayers investigated by raman spectroscopy. *The Journal of Physical Chemistry B*, 115(45):13181–13190, 2011.

[47] N. J. Wittenberg, T. W. Johnson, and S.-H. Oh. High-density arrays of submicron spherical supported lipid bilayers. *Analytical Chemistry*, 84(19): 8207–8213, 2012.

[48] L. R. Cambrea and J. S. Hovis. Formation of three-dimensional structures in supported lipid bilayers. *Biophysical Journal*, 92(10):3587–3594, 2007.

[49] A. P. Dabkowska, C. S. Niman, G. Piret, H. Persson, H. P. Wacklin, H. Linke, C. N. Prinz, and T. Nylander. Fluid and highly curved model membranes on vertical nanowire arrays. *Nano Letters*, 14(8):4286–4292, 2014.

[50] S. Y. Chou, P. R. Krauss, and P. J. Renstrom. Imprint lithography with 25-nanometer resolution. *Science*, 272(5258):85–87, 1996.

[51] Z. Cui. *Nanofabrication: Principles, Capabilities and Limits*. Springer, 2008.

[52] T. Eriksson, S. Yamada, P. V. Krishnan, S. Ramasamy, and B. Heidari. High volume nanoimprint lithography on III/V substrates: Imprint fidelity and stamp lifetime. *Microelectronic engineering*, 88(3):293–299, 2011.

[53] M. Beck and B. Heidari. Nanoimprint lithography for high volume HDI manufacturing. *OnBoard Technology*, pages 52–55, 2006.

[54] V. R. Manfrinato, L. Zhang, D. Su, H. Duan, R. G. Hobbs, E. A. Stach, and K. K. Berggren. Resolution limits of electron-beam lithography toward the atomic scale. *Nano Letters*, 13(4):1555–1558, 2013.

[55] M. Steglich, T. Käsebier, M. Zilk, T. Pertsch, E.-B. Kley, and A. Tünnermann. The structural and optical properties of black silicon by inductively coupled plasma reactive ion etching. *Journal of Applied Physics*, 116(17): 173503, 2014.

[56] H. Jansen, H. Gardeniers, M. de Boer, M. Elwenspoek, and J. Fluitman. A survey on the reactive ion etching of silicon in microtechnology. *Journal of Micromechanics and Microengineering*, 6(1):14–28, 1996.

[57] R. Legtenberg, H. Jansen, M. de Boer, and M. Elwenspoek. Anisotropic reactive ion etching of silicon using SF 6/o 2/CHF 3 gas mixtures. *Journal of the Electrochemical Society*, 142(6):2020–2028, 1995.

[58] D. Marsh. *Handbook of lipid bilayers*. CRC press, 2019.

[59] C. Hamai, T. Yang, S. Kataoka, P. S. Cremer, and S. M. Musser. Effect of average phospholipid curvature on supported bilayer formation on glass by vesicle fusion. *Biophysical Journal*, 90(4):1241–1248, 2006.

[60] R. P. Rand and N. L. Fuller. Structural dimensions and their changes in a reentrant hexagonal-lamellar transition of phospholipids. *Biophysical Journal*, 66(6):2127–2138, 1994.

[61] P. C. Weber, D. H. Ohlendorf, J. J. Wendoloski, and F. R. Salemme. Structural origins of high-affinity biotin binding to streptavidin. *Science*, 243(4887):85–88, 1989.

[62] M. Goedert. Alpha-synuclein and neurodegenerative diseases. *Nature Reviews Neuroscience*, 2(7):492–501, 2001.

[63] A. B. Singleton, M. Farrer, J. Johnson, A. Singleton, S. Hague, J. Kachergus, M. Hulihan, T. Peuralinna, A. N. Dutra, S. Lincoln, et al. [alpha]-synuclein locus triplication causes parkinson's disease. *Science*, 302(5646): 841–842, 2003.

[64] E. R. Middleton and E. Rhoades. Effects of curvature and composition on α-synuclein binding to lipid vesicles. *Biophysical Journal*, 99(7):2279–2288, 2010.

[65] D. Semwogerere and E. R. Weeks. Confocal microscopy. *Encyclopedia of Biomaterials and Biomedical Engineering*, 23:1–10, 2005.

[66] A. Nwaneshiudu, C. Kuschal, F. H. Sakamoto, R. R. Anderson, K. Schwarzenberger, and R. C. Young. Introduction to confocal microscopy. *Journal of Investigative Dermatology*, 132(12):1–5, 2012.

[67] E. Wu, K. Jacobson, and D. Papahadjopoulos. Lateral diffusion in phospholipid multibilayers measured by fluorescence recovery after photobleaching. *Biochemistry*, 16(17):3936–3941, 1977.

[68] T. K. L. Meyvis, S. C. De Smedt, P. Van Oostveldt, and J. Demeester. Fluorescence recovery after photobleaching: a versatile tool for mobility and interaction measurements in pharmaceutical research. *Pharmaceutical Research*, 16(8):1153–1162, 1999.

[69] J. Yguerabide, J. A. Schmidt, and E. E. Yguerabide. Lateral mobility in membranes as detected by fluorescence recovery after photobleaching. *Biophysical Journal*, 40(1):69–75, 1982.

[70] P. Jönsson, M. P. Jonsson, and F. Höök. Sealing of submicrometer wells by a shear-driven lipid bilayer. *Nano Letters*, 10(5):1900–1906, 2010.

[71] SciPy.org. SciPy, optimize curve-fit. URL `https://docs.scipy.org/doc/scipy/reference/generated/scipy.optimize.curve_fit.html`. Accessed: 2021-06-18.

[72] D. M. Soumpasis. Theoretical analysis of fluorescence photobleaching recovery experiments. *Biophysical Journal*, 41(1):95–97, 1983.

[73] M. C. Dixon. Quartz crystal microbalance with dissipation monitoring: enabling real-time characterization of biological materials and their interactions. *Journal of Biomolecular Techniques: JBT*, 19(3):151, 2008.

[74] G. Sauerbrey. Verwendung von Schwingquarzen zur Wägung dünner Schichten und zur Mikrowägung. *Zeitschrift für physik*, 155(2):206–222, 1959.

[75] M. Rodahl and B. Kasemo. On the measurement of thin liquid overlayers with the quartz-crystal microbalance. *Sensors and Actuators A: Physical*, 54(1-3):448–456, 1996.

[76] N.-J. Cho, C. W. Frank, B. Kasemo, and F. Höök. Quartz crystal microbalance with dissipation monitoring of supported lipid bilayers on various substrates. *Nature Protocols*, 5(6):1096–1106, 2010.

[77] C. A. Keller and B. Kasemo. Surface specific kinetics of lipid vesicle adsorption measured with a quartz crystal microbalance. *Biophysical Journal*, 75 (3):1397–1402, 1998.

[78] J. F. Nagle and S. Tristram-Nagle. Structure of lipid bilayers. *Biochimica et Biophysica Acta (BBA)-Reviews on Biomembranes*, 1469(3):159–195, 2000.

[79] P. Müller-Buschbaum. GISAXS and GISANS as metrology technique for understanding the 3d morphology of block copolymer thin films. *European Polymer Journal*, 81:470–493, 2016.

[80] S. Nouhi, M. S. Hellsing, V. Kapaklis, and A. R. Rennie. Grazing-incidence small-angle neutron scattering from structures below an interface. *Journal of Applied Crystallography*, 50(4):1066–1074, 2017.

[81] A. V. Feoktystov, H. Frielinghaus, Z. Di, S. Jaksch, V. Pipich, M.-S. Appavou, E. Babcock, R. Hanslik, R. Engels, G. Kemmerling, et al. KWS-1 high-resolution small-angle neutron scattering instrument at JCNS: current state. *Journal of Applied Crystallography*, 48(1):61–70, 2015.

[82] NCNR. Very small-angle neutron scattering. URL `https://www.nist.gov/ncnr/chrns-vsans-very-small-angle-neutron-scattering`. Accessed: 2021-06-22.

[83] R. K. Heenan, S. E. Rogers, D. Turner, A. E. Terry, J. Treadgold, and S. M. King. Small angle neutron scattering using Sans2d. *Neutron News*, 22(2):19–21, 2011.

[84] A. R. Rennie, M. S. Hellsing, E. Lindholm, and A. Olsson. Note: Sample cells to investigate solid/liquid interfaces with neutrons. *Review of Scientific Instruments*, 86(1):016115, 2015.

[85] V. F. Sears. Neutron scattering lengths and cross sections. *Neutron News*, 3(3):26–37, 1992.

[86] J. R. Rumble, editor. *CRC Handbook of Chemistry and Physics*. CRC Press, 102nd edition, 2021.

[87] S. Tristram-Nagle, H. I. Petrache, and J. F. Nagle. Structure and interactions of fully hydrated dioleoylphosphatidylcholine bilayers. *Biophysical Journal*, 75(2):917–925, 1998.

[88] N. Kučerka, S. Tristram-Nagle, and J. F. Nagle. Structure of fully hydrated fluid phase lipid bilayers with monounsaturated chains. *Journal of Membrane Biology*, 208(3):193–202, 2006.

[89] A. I. Greenwood, S. Tristram-Nagle, and J. F. Nagle. Partial molecular volumes of lipids and cholesterol. *Chemistry and Physics of Lipids*, 143 (1-2):1–10, 2006.

[90] D. Duxbury, R. Heenan, D. McPhail, D. Raspino, N. Rhodes, S. Rogers, E. Schooneveld, E. Spill, and A. Terry. Performance characteristics of

the new detector array for the SANS2d instrument on the ISIS spallation neutron source. *Journal of Instrumentation*, 9(12):C12051, 2014.

[91] P. Müller-Buschbaum, E. Maurer, E. Bauer, and R. Cubitt. Surface versus confinement induced morphology transition in triblock copolymer films: A grazing incidence small angle neutron scattering investigation. *Langmuir*, 22(22):9295–9303, 2006.

[92] M. Rauscher, T. Salditt, and H. Spohn. Small-angle x-ray scattering under grazing incidence: The cross section in the distorted-wave Born approximation. *Physical Review B*, 52(23):16855–16863, 1995.

[93] P. Busch, M. Rauscher, D.-M. Smilgies, D. Posselt, and C. M. Papadakis. Grazing-incidence small-angle x-ray scattering from thin polymer films with lamellar structures–the scattering cross section in the distorted-wave Born approximation. *Journal of Applied Crystallography*, 39(3):433–442, 2006.

[94] I. Livsey. Neutron scattering from concentric cylinders. intraparticle interference function and radius of gyration. *Journal of the Chemical Society, Faraday Transactions 2: Molecular and Chemical Physics*, 83(8): 1445–1452, 1987.

[95] M. I. Mishchenko, J. W. Hovenier, and L. D. Travis. *Light scattering by nonspherical particles: theory, measurements, and applications*. Academic Press, 2000.

[96] N. Kučerka, J. Gallová, D. Uhríková, P. Balgavỳ, M. Bulacu, S.-J. Marrink, and J. Katsaras. Areas of monounsaturated diacylphosphatidylcholines. *Biophysical Journal*, 97(7):1926–1932, 2009.

[97] V. Nele, M. N. Holme, U. Kauscher, M. R. Thomas, J. J. Doutch, and M. M. Stevens. Effect of formulation method, lipid composition, and PEGylation on vesicle lamellarity: a small-angle neutron scattering study. *Langmuir*, 35(18):6064–6074, 2019.

[98] J. U. De Mel, S. Gupta, R. M. Perera, L. Ngo, P. Zolnierczuk, M. Bleuel, S. V. Pingali, and G. J. Schneider. Influence of external nacl salt on membrane rigidity of neutral DOPC vesicles. *Langmuir*, 36(32):9356–9367, 2020.

[99] V. Chappa, Y. Smirnova, K. Komorowski, M. Müller, and T. Salditt. The effect of polydispersity, shape fluctuations and curvature on small unilamellar vesicle small-angle X-ray scattering curves. *Journal of Applied Crystallography*, 54(2):557–568, Apr 2021.

[100] D. J. Mitchell and B. W. Ninham. Micelles, vesicles and microemulsions. *Journal of the Chemical Society, Faraday Transactions 2: Molecular and Chemical Physics*, 77(4):601–629, 1981.

[101] A. Nunns, J. Gwyther, and I. Manners. Inorganic block copolymer lithography. *Polymer*, 54(4):1269–1284, 2013. ISSN 0032-3861.

[102] A. Löfstrand, R. Jafari Jam, K. Mothander, T. Nylander, M. Mumtaz, A. Vorobiev, W.-C. Chen, R. Borsali, and I. Maximov. Poly (styrene)-block-maltoheptaose films for sub-10 nm pattern transfer: Implications for transistor fabrication. *ACS Applied Nano Materials*, 2021.

[103] I. Otsuka, S. Tallegas, Y. Sakai, C. Rochas, S. Halila, S. Fort, A. Bsiesy, T. Baron, and R. Borsali. Control of 10 nm scale cylinder orientation in self-organized sugar-based block copolymer thin films. *Nanoscale*, 5(7): 2637–2641, 2013.

[104] I. Otsuka, T. Isono, C. Rochas, S. Halila, S. Fort, T. Satoh, T. Kakuchi, and R. Borsali. 10 nm scale cylinder–cubic phase transition induced by caramelization in sugar-based block copolymers. *ACS Macro Letters*, 1 (12):1379–1382, 2012.

[105] A. Devishvili, K. Zhernenkov, A. J. C. Dennison, B. P. Toperverg, M. Wolff, B. Hjörvarsson, and H. Zabel. SuperADAM: Upgraded polarized neutron reflectometer at the Institut Laue-Langevin. *Review of Scientific Instruments*, 84(2):025112, 2013.

[106] A. Vorobiev, A. Devishvilli, G. Palsson, H. Rundlöf, N. Johansson, A. Olsson, A. Dennison, M. Wollf, B. Giroud, O. Aguettaz, et al. Recent upgrade of the polarized neutron reflectometer Super ADAM. *Neutron News*, 26 (3):25–26, 2015.

[107] M. Björck and G. Andersson. GenX: an extensible X-ray reflectivity refinement program utilizing differential evolution. *Journal of Applied Crystallography*, 40(6):1174–1178, 2007.

[108] C. A. Browne. Moisture absorptive power of different sugars and carbohydrates under varying conditions of atmospheric humidity. *Industrial & Engineering Chemistry*, 14(8):712–713, 1922.

[109] E. Cianci, D. Nazzari, G. Seguini, and M. Perego. Trimethylaluminum diffusion in PMMA thin films during sequential infiltration synthesis: In situ dynamic spectroscopic ellipsometric investigation. *Advanced Materials Interfaces*, 5(20):1801016, 2018.

[110] J. Plomp, V. O. De Haan, R. M. Dalgliesh, S. Langridge, and A. A. van Well. Neutron spin-echo labelling at OffSpec, an ISIS second target station project. *Thin Solid Films*, 515(14):5732–5735, 2007.

[111] J. R. P. Webster, S. Langridge, R. M. Dalgliesh, and T. R. Charlton. Reflectometry techniques on the Second Target Station at ISIS: Methods and science. *The European Physical Journal Plus*, 126(11):1–5, 2011.

[112] J. Major, A. Vorobiev, A. Rühm, R. Maier, M. Major, M. Mezger, M. Nülle, H. Dosch, G. P. Felcher, P. Falus, et al. A spin-echo resolved grazing incidence scattering setup for the neutron interrogation of buried nanostructures. *Review of Scientific Instruments*, 80(12):123903, 2009.

[113] R. Ashkar, R. Pynn, R. Dalgliesh, N. V. Lavrik, and I. I. Kravchenko. A new approach for probing matter in periodic nanoconfinements using neutron scattering. *Journal of Applied Crystallography*, 47(4):1367–1373, 2014.

[114] O. S. Heavens. *Optical properties of thin solid films*. Butterworth, London, England, 1955.

[115] H. P. Vacklin, F. Tiberg, and R. K. Thomas. Formation of supported phospholipid bilayers via co-adsorption with β-d-dodecyl maltoside. *Biochimica et Biophysica Acta (BBA)-Biomembranes*, 1668(1):17–24, 2005.